Observations on non-linear rock mass strength from the Nantlle Valley, Gwynedd, Wales

by

Alastair David Dewar

A thesis submitted to The University of Birmingham for the degree of MASTER OF SCIENCE BY RESEARCH

School of Geography, Earth & Environmental Sciences

The University of Birmingham

August 2021

Abstract

Accurate prediction of non-linear rock mass strength is required to model the ground as a mechanical continuum to aid design and analysis of slopes and underground excavations. Two failure criteria are discussed: The Generalised Hoek-Brown criterion defined in terms of maximum and minimum principal stress, and Barton's criterion in terms of normal and shear stress. The Generalised Hoek-Brown criterion defines non-linearity and the frictional properties of the rock by way of a petrographic constant m_i. Barton's joint roughness coefficient controls the curvature of the failure envelope and gives more pronounced non-linearity.

Numerical simulations back analysing failure of a large man-made near vertical rock slope identified combinations of Hoek-Brown parameters resulting in failure. Neither criterion was found to provide a satisfactory explanation for the observed failure, several decades after the cessation of quarrying. The collapse was attributed to failure of rock bridges after delayed fracture propagation, potentially from the weathering of minerals promoted by water penetration into the rock mass from joints formed or opened in response to significant horizontal stress relief from original quarry excavation.

To support the back analysis process and the potential development of the quarries for a hydropower scheme several strength envelopes based on Barton's criterion were determined for the principal geological subdivisions of the area. Failure envelopes were determined for various late Neoproterozoic, Cambrian and Ordovician, tuffs, metapelites and metapsammites as well acid and basic intrusions, beyond the extent of the proposed hydroelectric scheme. From the failure envelopes derived instantaneous Mohr-Coulomb shear strength parameters are provided for various stress increments.

Acknowledgements

My supervisors, Dr Carl Stevenson, and Dr James Wheeley, and the support provided by Professor Malcolm Bolton of The University of Cambridge have been fundamental to completion of this document. I've relied on land access and survey data provided by Mark Billingham and Nigel Spires. My employer, Sir Robert McAlpine, has gifted me several days to pursue part-time postgraduate study to engage with some of the technical challenges associated with non-linear rock mass behaviour. Colleagues and friends that have supported my endeavours include, Catherine Everett, Michael Gerard-Canny, Mark Whatman and Alan Chatham. Keith Johnson of EDF Nuclear Generation Ltd. provided me with sample material for testing, these samples proved especially useful as it allowed work to continue while fieldwork was delayed due to coronavirus. Thanks to Dave Holmes of Quarry Battery Company for allowing the use of QBC's data for academic purposes. Finally, I would like to thank my wife, Natalie, for her patience and support and our son, Ben, for scribing many Schmidt hammer results during recent months.

Contents

List of Figures

List of Tables

Abbreviations and symbols used

GSI	geological strength index
JCS	joint compressive strength
JRC	joint roughness coefficient
RMR	rock mass rating
RQD	rock quality designation
UCS	(or σ_c) uniaxial compressive strength
A	constant for determining R_c
a	rock mass constant
c	cohesion
c_i	instantaneous cohesion
D	reduction factor for stress relief or disturbance / damage of the rock mass
D^*	constant for determining R_c
E_i	intact modulus
E_{rm}	rock mass modulus
G	shear modulus
g	acceleration due to gravity, 9.81 m/s^2
H	depth
H_{crit}	critical height of a vertical rock slope
$I_{s(50)}$	point load index
$I_{s(50)90}$	point load index at 90° to a fabric
$I_{s(50)min}$	point load index parallel to a fabric
JC_{89}	joint condition
K	bulk modulus
k_h	coefficient of horizontal stress
k_β	coefficient to represent the effect of strength anisotropy
m_b	petrographic parameter of a rock mass
m_i	petrographic parameter for intact rock
s	rock mass constant
R	mean Schmidt rebound hardness on dry unweathered surfaces
r	mean Schmidt rebound hardness on wet weathered surfaces
R_c	anisotropy ratio
u	pore water pressure
α	angle of sliding onset in degrees
β	angle between σ_1 and a conjugate fabric (half the dihedral angle) or angle between σ_1 and an isotropic fabric
γ	mean unit weight of overburden
ε	strain
ε_{xx}	strain in the x direction
θ	angle between σ_3 and a conjugate fabric
ν	Poisson's ratio
σ_1	maximum principal stress
σ'_1	maximum effective principal stress
σ_2	intermediate principal stress

σ_3 minimum principal stress

σ'_3 minimum effective principal stress

σ'_{3max} maximum confining stress where the calculation of Mohr-Coulomb parameters from the Hoek-Brown criterion is valid

σ_c uniaxial compressive strength

$\sigma_{c(90)}$ uniaxial compressive strength at 90° to a fabric

$\sigma_{c(min)}$ uniaxial compressive strength parallel to a fabric

$\sigma_{c(\beta)}$ uniaxial compressive strength at angle β to a fabric

σ_{ci} unconfined compressive strength

$\sigma_{c(i)}$ crack initiation stress from UCS test

σ'_{cm} rock mass strength

σ_n normal stress

σ_t tensile strength

σ_{tB} Brazilian tensile strength

σ_{ti} direct intact tensile strength

$\sigma_{t(i)}$ crack initiation stress during tension testing

σ_{xx} stress in the *x* direction

σ_{yy} stress in the *y* direction

σ_{zz} stress in the *z* direction

τ shear stress

φ angle of internal friction

φ_b basic friction angle

φ_i instantaneous angle of internal friction

φ_s secant angle of internal friction

φ_t tangent angle of internal friction

1 Introduction

1.1 Background

This thesis has been prepared to support the design and construction of a potential hydroelectric facility, Dorothea Lakes, located in the Nantlle Valley, Gwynedd, North Wales. The proposed development is not typical of civil engineering activities in the UK because of the stresses involved and the absence of underground rock engineering from mainstream construction practice.

The research described in this document has been undertaken prior to application of a Development Consent Order (DCO) for the scheme, which is required for nationally significant infrastructure projects. It is suggested that after starting the DCO process the time available to undertake the work documented in this study would be severely limited by commercial pressure to plan, design, construct, and commission the scheme in the shortest possible period to start making a return on a significant investment. The work described considers the non-linear strength of rock masses of direct relevance to Dorothea Lakes as well as other rock masses of the Nantlle Valley.

1.2 Objectives

The objectives of this study are:

- To determine the extent to which rock masses of the Nantlle Valley can be treated as a mechanical continuum for engineering purposes.
- To identify an appropriate failure criterion and determine non-linear strength envelopes and shear strength parameters for various rock types and masses of the Nantlle Valley. This is to aid selection of an appropriate failure criterion by others

at a later date and improve understanding of rock mass behaviour in the area and to aid management of existing rock slopes.

- To reduce uncertainty associated with the technical complexities of rock mass behaviour and assessing the stability of near vertical, part-submerged rock slopes, some of which are more than 100 m high.

1.3 Document structure

The remainder of the introductory text provides an overview of pumped hydropower, the proposed Dorothea Lakes development as well as an example of the technical and commercial risks associated with underground construction. Section 2 summarises published information on the geology and geological setting of the Nantlle Valley. This is followed in section 3 by a summary of common methods of rock mass classification, the relevance of intact strength and stress, as well as information available on the engineering behaviour of one of the principal geological units of the area, the Llanberis Slates Formation.

Section 4 explains the application and limitations of the Hoek-Brown failure criterion and its use of the Geological Strength Index (section 5). The author's use of this criterion to back analyse a rock slope failure is presented in section 6. The back analysis process identifies combinations of parameters resulting in a calculated mode of failure that best replicates the observed mode and geometry of the failure, and thus potential strengths mobilised at the time of failure.

Section 7 discusses an alternative failure criterion (Barton's criterion) and in section 8 failure envelopes derived by the author are presented prior to concluding observations reflecting on the objectives of the study (section 9). This document is supported by

appendices explaining the methodology for determining Barton's failure criterion (Appendix C), as well as details of slope stability analyses undertaken (Appendix D) and the author's validation of these analyses (Appendix E).

1.4 Pumped storage

Pumped hydroelectric schemes, or pumped storage, allow a headpond to be filled and then discharged for power production. The main benefits are twofold: to produce electricity, and revenue, at short notice to meet demand and secondly to consume electricity, for a fee, at times of oversupply by pumping water uphill to fill the headpond. This is especially useful when other forms of energy generation cannot practically be slowed to meet reduced demand. The need to charge a headpond makes pump storage schemes nett consumers of electricity, however they are potentially useful as long-term tool to balance electricity generation and oversupply.

According to the International Hydropower Association the UK has a 2.4 GW hydropower potential and currently has 4.7 GW of installed capacity, of which 60% is pumped storage. In all forms, hydropower in the UK has accounted for approximately 2% of electricity generation consistently over the last 30 years (IHA, 2021).

1.5 Dorothea Lakes

Dorothea Lakes (Figure 1-1) is 300-acre estate in the Nantlle Valley and is located between the villages of Talysarn to the west and Nantlle to the east (Figure 1-4). The estate includes five former slate quarries, the largest of which is the Dorothea Quarry (SH 4990 5320), all are now flooded. A bathymetric survey of Dorothea Lake, the lake that filled Dorothea Quarry after the cessation of slate extraction, established a volume of

3,118 Mm^3, and a maximum water depth of 96.6 m below a water level of 97.34 mOD (APEM, 2019).

Figure 1-1 Location of Dorothea Lakes, from Bing Maps (by Mark Whatman).

Potential construction of a pump storage scheme would require a tunnel to connect a tailpond, Dorothea Lake, (Figure 1-2) to an enlarged headpond formed by deepening and damming an existing natural lake Cwm Silyn (SH 5130 5070 Figure 1-3), on the higher ground approximately 3 km to the southeast. South of the B4418 (Figure 1-4) the study area is located within Snowdonia National Park. On 28th July 2021 the slate landscapes

of North Wales were designated a World Heritage Site (UNESCO, 2021), the application for which includes provision for the proposed development.

Figure 1-4 and Figure 1-5 show maps of Dorothea Lake and adjacent flooded quarries, Cwm Silyn and the approximate alignment of a potential tunnel to connect the two. As well as significant underground works a dam would be required to increase the working volume of water in the headpond. Detailed analysis of the stability of the existing side slopes of Dorothea Lake when subjected to cyclic and rapid drawdown during a protracted working life would also be required.

Figure 1-2 View of Dorothea Lake from the west.

Figure 1-3 View looking southeast to Craig Cum Silyn and the head pond location.

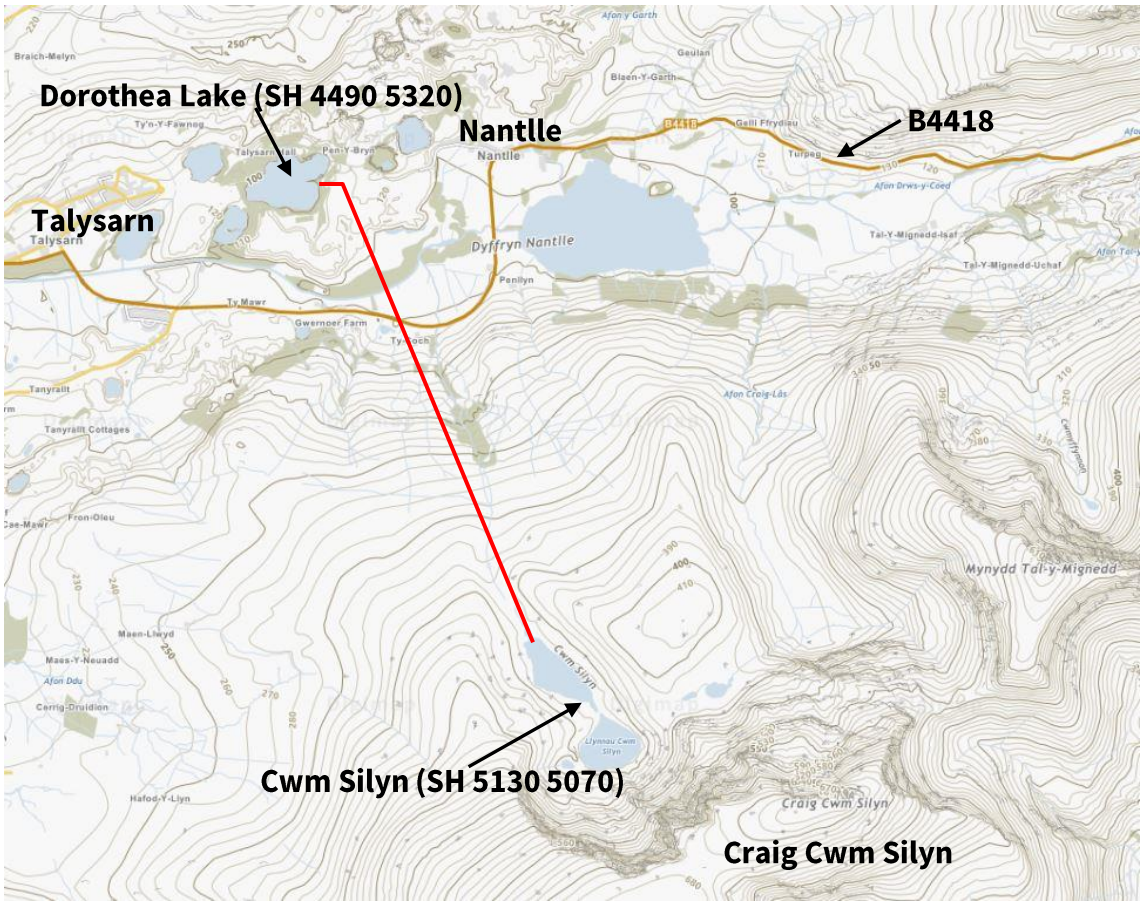

Figure 1-4 Location of the proposed Dorothea hydropower project (Digimap).

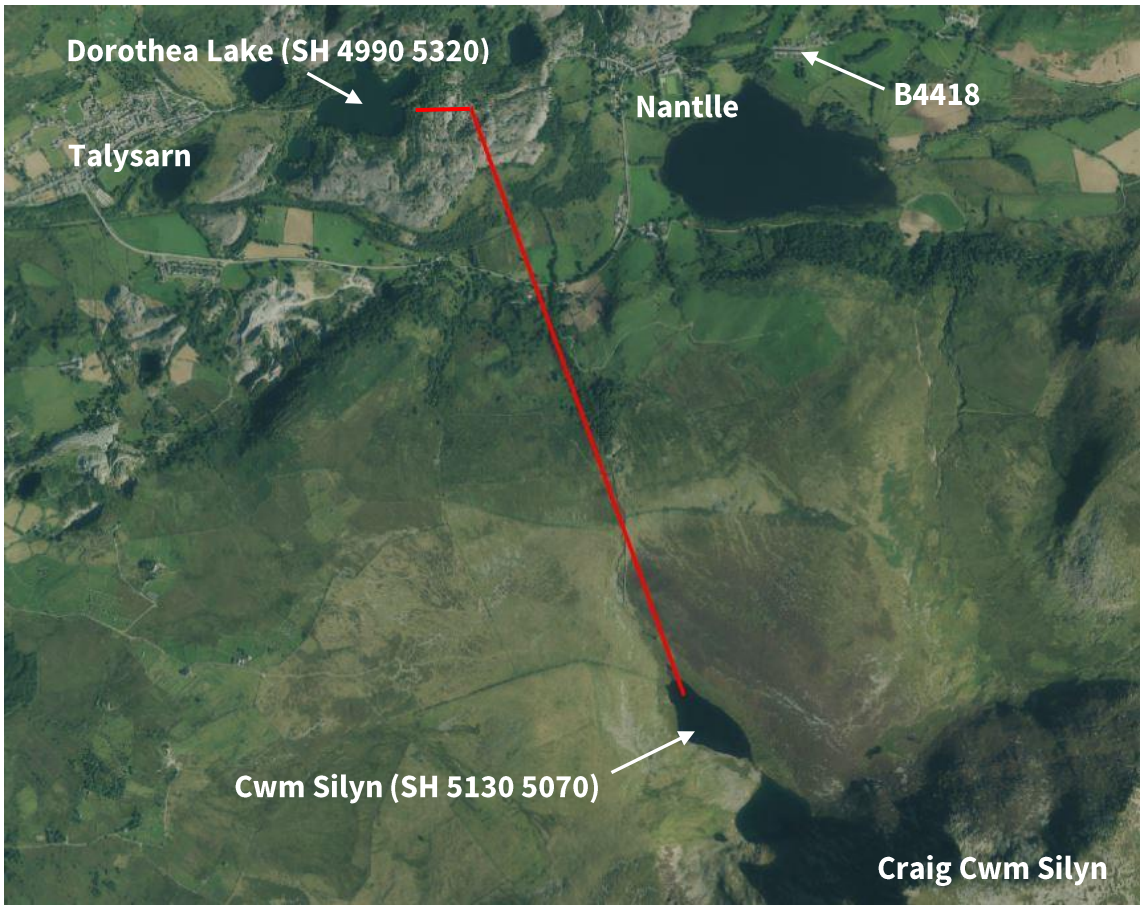

Figure 1-5 Aerial image of the proposed Dorothea hydropower project (Digimap).

1.6 Geotechnical and commercial risks in tunnelling

Tunnelling and underground excavation is potentially a high-risk activity, commercially, technically also for the safety of personnel working underground. According to Eurocode 7 (BSI, 2004) tunnelling in fractured rock and tunnels with special water tightness requirements fall into the highest geotechnical risk category, Category 3.

The commercial risks are no less significant. Hencher (2019) describes contractual responsibilities in common law in England and Wales as well as the interconnection of technical and commercial failings with respect to the collapse of a 71 m length of

hydropower tunnel through a well-known fault zone in August 2009 (Glendoe, Scotland). The collapse occurred less than a year after the £145 M, 100 MW scheme started generating. The tunnel was originally to have been lined throughout, however through the correct contractual mechanisms and with the agreement of experts from both the purchaser and contractor, permanent lining was omitted from over 99% of the tunnel's length (Hencher, 2019). Such contractual tools allow a saving to both parties and opportunity to accelerate construction in the event of ground conditions being better than anticipated.

Upon appeal in 2018 The Court of Session reversed a previous decision in favour of the purchaser to allow recovery of repair costs (£108 M) from the defendants (Ground Engineering, 2018). Reputational damage cannot be so easily quantified. The Glendoe failure and subsequent litigation highlights the need for a profound understanding of ground behaviour to inform commercial, programme and safety decisions.

2 The geology of the Nantlle Valley and the Welsh Basin

2.1 Overview of the Welsh Basin

The Welsh Basin was a Lower Palaeozoic marine basin constrained between the Menai Straight fault system and faults of the Welsh Borderland (Figure 2-1) (Rushton et al., 2000; Woodcock and Strachan, 2002). The basin is underlain by a basement of felsic intrusive and extrusive rocks of late Neoproterozoic and earliest Cambrian age (Schofield et al., 2021), formed within a volcanic arc environment (Compston et al., 2002). This basement forms the Cymru Terrane, a microterrane of Avalonia (Schofield et al., 2016), which along with other pre-Atlantic terranes (Figure 2-3) were located south of the equator (Figure 2-2) during the Lower Palaeozoic.

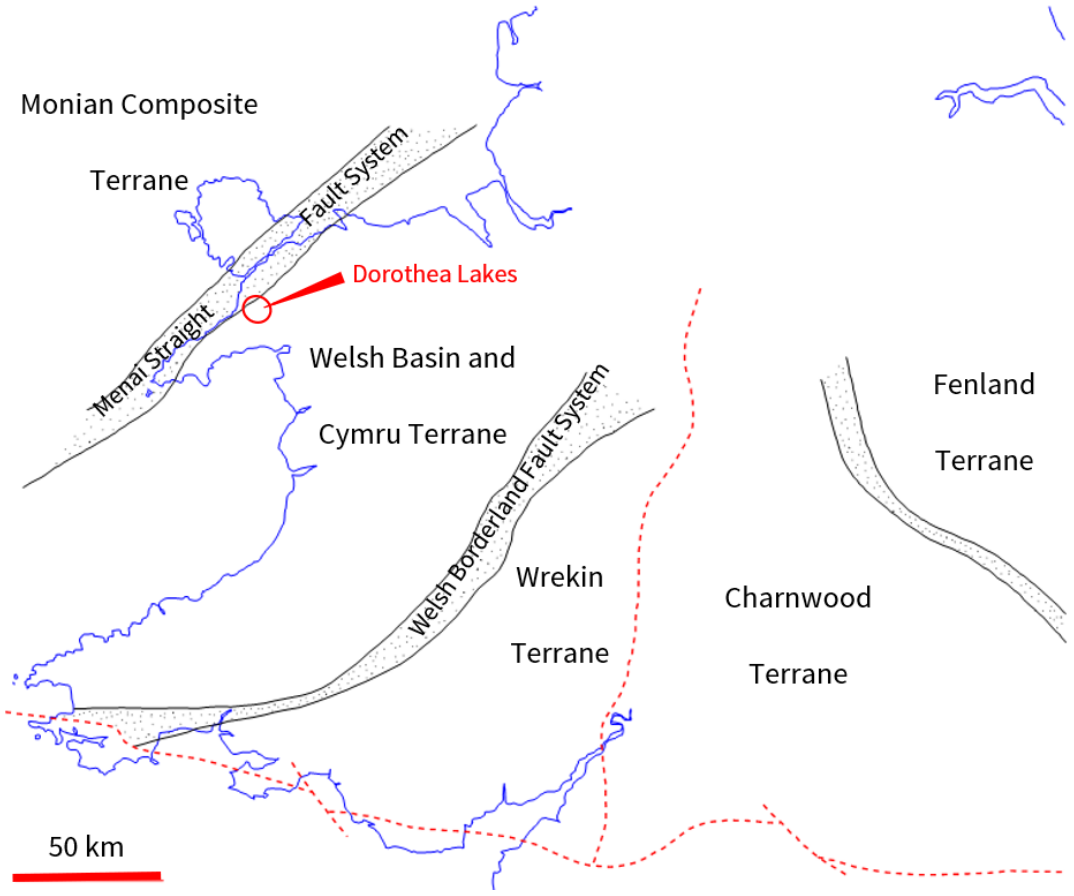

Figure 2-1 Microterranes of southern Britain, redrawn from Schofield et al. (2016).

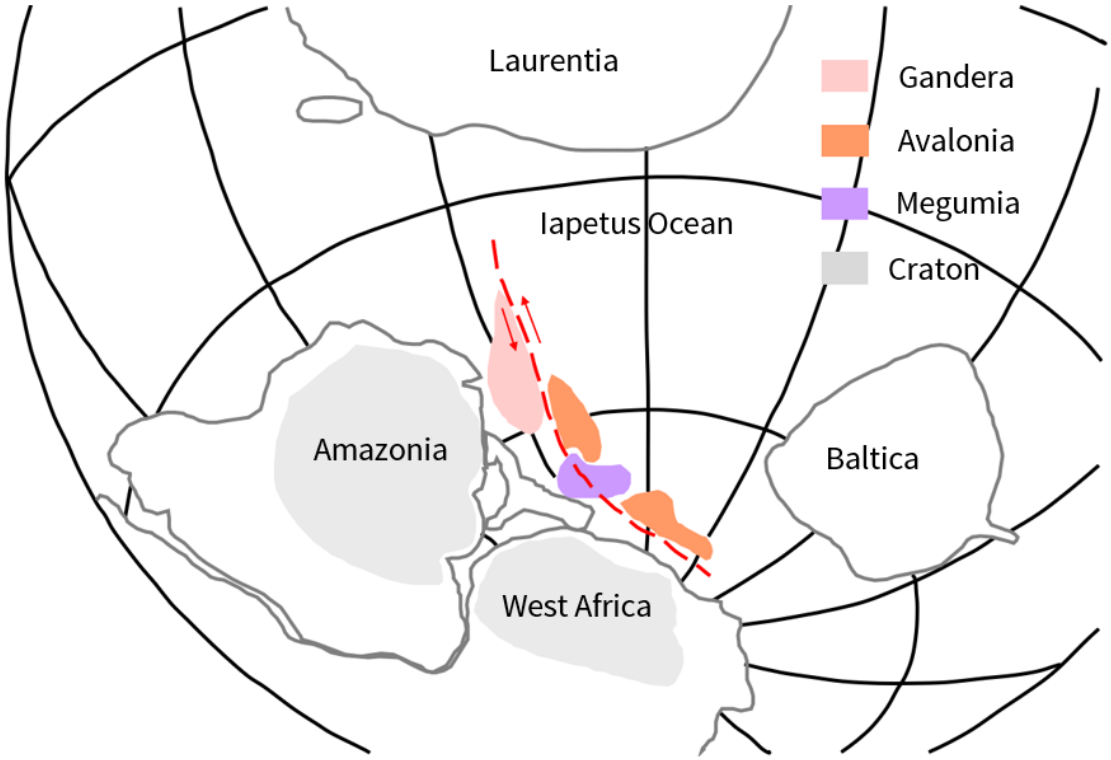

Figure 2-2 Paleogeography 500 Ma, redrawn from Pothier et al. (2015).

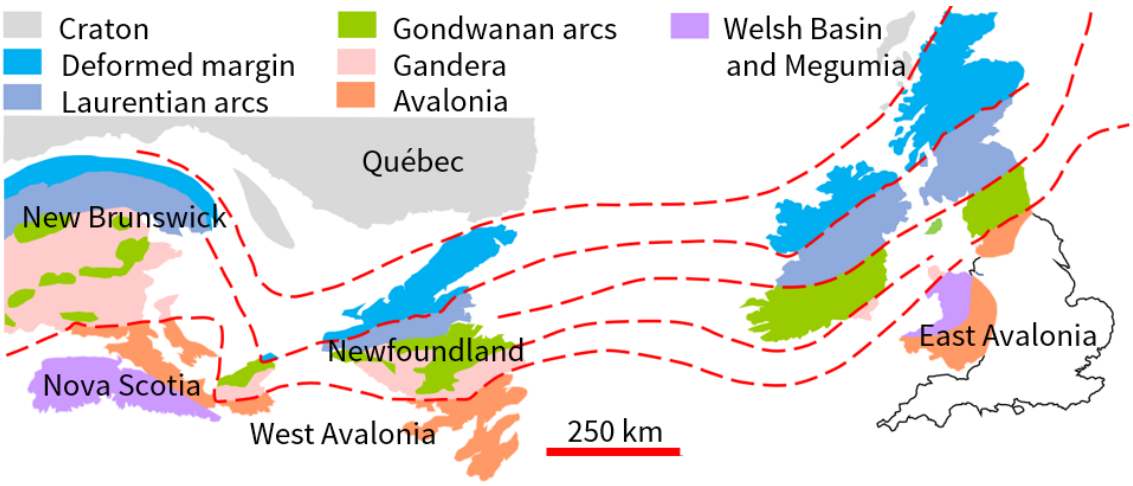

Figure 2-3 Pre-Atlantic Caledonides terrane map, redrawn from Pothier et al. (2015).

Welsh Basin sedimentation during the Lower Palaeozoic was dominated by an Irish Sea Landmass to the north, and later by the occasionally emergent Midland Platform to the east. Staged rises in sea level at the start of Cambrian times have been linked to the

breakup of the supercontinent Pannotia and ice sheet changes (Woodcock and Strachan 2002; Nield 2007). Subsidence rates were sufficiently great to allow shallow marine conditions to be replaced by deeper marine and turbiditic conditions before a return to shallower conditions in later Cambrian times (Woodcock and Strachan, 2002).

Ordovician sea level fluctuations were accompanied by volcanism associated with the development of large volcanic centres in a back-arc setting. Preserved volcanism has been interpreted as the start of subduction of Iapetus prior to rifting of Avalonia and Gondwana during Floian (Arenig), or later, times (Rushton, et al. 2000; 2011). Ordovician stratigraphy of North Wales is divided into six volcanic and two sedimentary groups, with interlayering of volcanic groups into contemporary sedimentary groups (Rushton and Howells, 1998). Schofield et al. (2008) quote the work of others, suggesting that volcanic activity occurred in three phases: Tremadoc, Floian to Darriwilian (mid-Arenig to Llanvirn) and from Darriwilian to Sandbian (Llanvirn to Caradoc) time. Comparison of current international and historical British regional terminology is provided in Table 2.1.

2.2 Geology of the Nantlle Valley

Geological maps of the Nantlle Valley include 1:10,000 and 1:50,000 scale solid and superficial maps (BGS 1985; 2015) and the online Geology of Britain Viewer (BGS, 2019). These indicate a Precambrian basement overlain by Ediacaran to Ordovician metasediments with minor Ordovician intrusions. Intrusions comprise dolerite and microgranite, which form the mountain of Mynydd Mawr (SH 53978 54680). Figure 2-4 shows a geological map of the study area and Figure 2-5 a map of the wider area. A summary of geological units is provided as Table 2.1 and a geological cross section as

Figure 2-6, which shows a number of near vertical faults within the Llanberis Slates Formation.

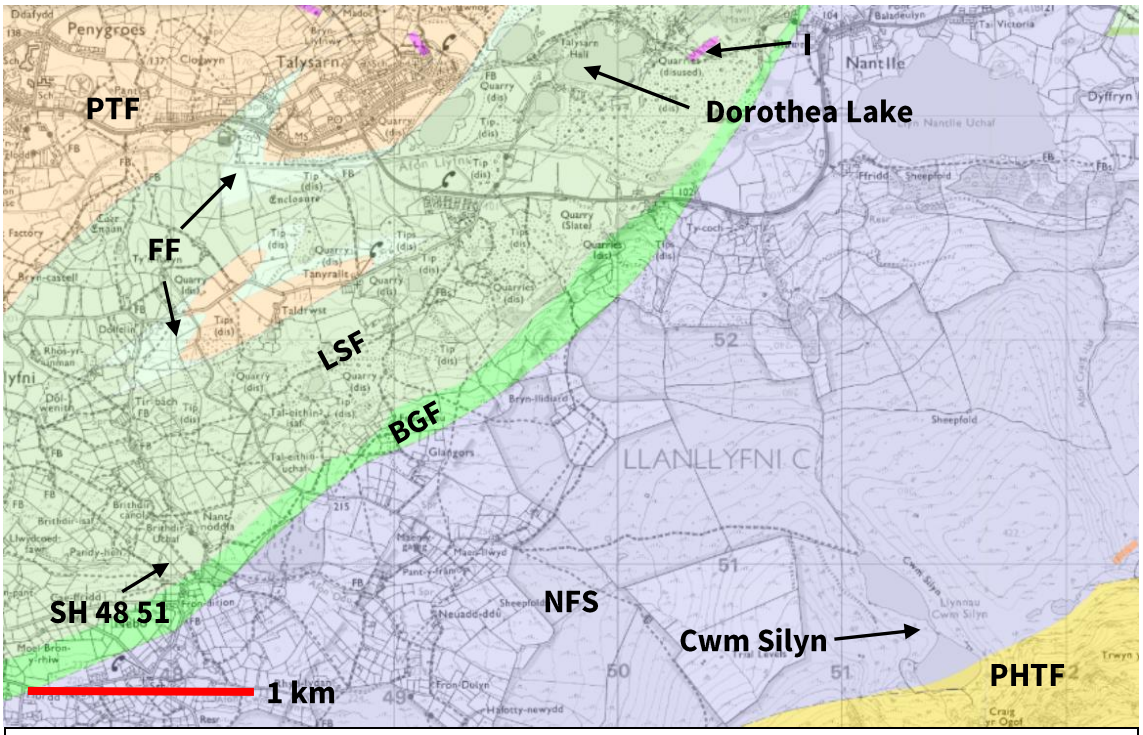

PTF - Padarn Tuff Formation, FF - Fachwen Formation, LSF - Llanberis Slates Formation, BGF - Bronllwyd Grit Formation, NFS - Nant Ffrancon Subgroup, PHTF - Pitts Head Tuff Formation, I - Microgabbro intrusion

Figure 2-4 Geological map of the study area (Digimap).

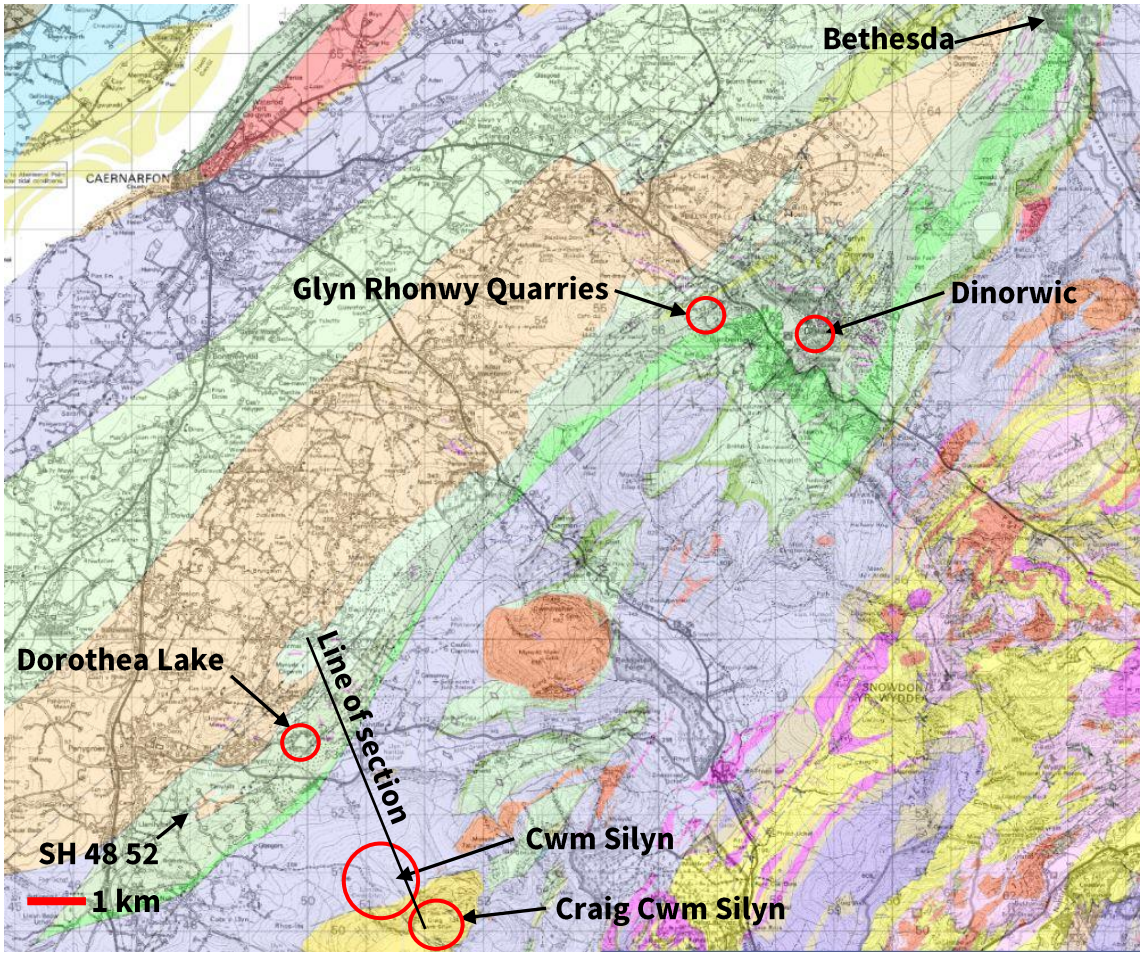

Figure 2-5 Geological map of the Gwynedd Slate Belt (Digimap).

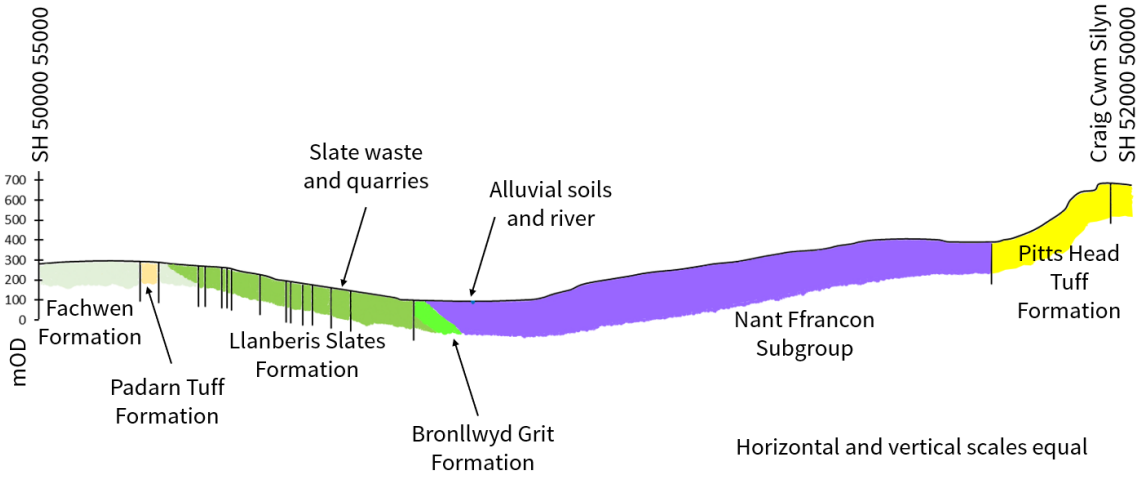

Figure 2-6 Cross section through the Nantlle Valley (drawn from BGS, 1985).

Neoproterozoic and earliest Cambrian rocks underlie alluvium and extensive slate waste on the valley floor and outcrop on the northern side of the Valley. These are grouped as the Arfon Group, which is subdivided, into the Padarn Tuff and Fachwen Formations. These are overlain by the Harlech Grits Group, comprising the Llanberis Slates, Bronllwyd Grit and Marchlyn Formations. The Llanberis Slates Formation forms the Cambrian (or Gwynedd) Slate Belt and crops out to the northeast to Llanberis, Dinorwic and Bethesda (Figure 2-5).

The southern side of the Nantlle Valley is underlain by Ordovician rocks of the Nant Ffrancon Subgroup and Pitts Head Tuff Formation, subdivisions of the Ogwen and Snowdon Volcanic Groups respectively. Faulting, downthrowing to the southeast places Cambrian against Ordovician strata. To the southeast of Cwm Silyn faulting places the Pitts Head Tuff Formation next to the Nant Ffrancon Subgroup. Craig Cwm Silyn, the mountain to the south on the study area, is formed of the Pitts Head Tuff Formation. The extent of the principal geological subdivisions is shown in Figure 2-7

Morris and Fearnside (1926) point to work undertaken in the area that contributed to Lapworth's Ordovician System (Lapworth 1879; Oldroyd 1990).

2.3 Timing of Neoproterozoic and Lower Palaeozoic events

Table 2.1 shows chronostratigraphic subdivisions and relevant events in the Welsh Basin based on Howells and Smith (1997), Fortey et al. (2000), Woodcock and Strachan (2002), Rushton et al. (2011) and Cohen et al. (2020).

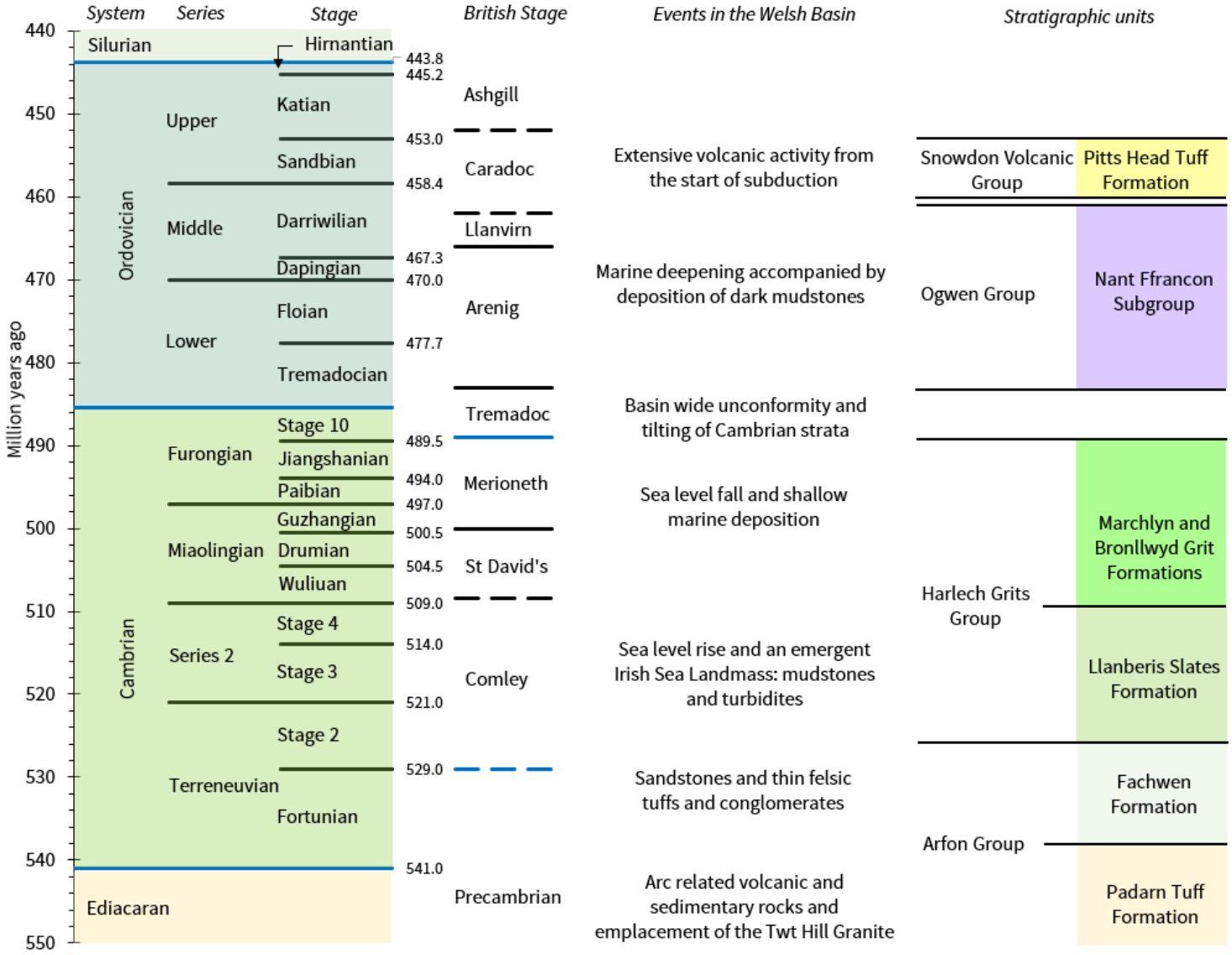

Table 2.1 Key geological subdivisions and events of the study area.

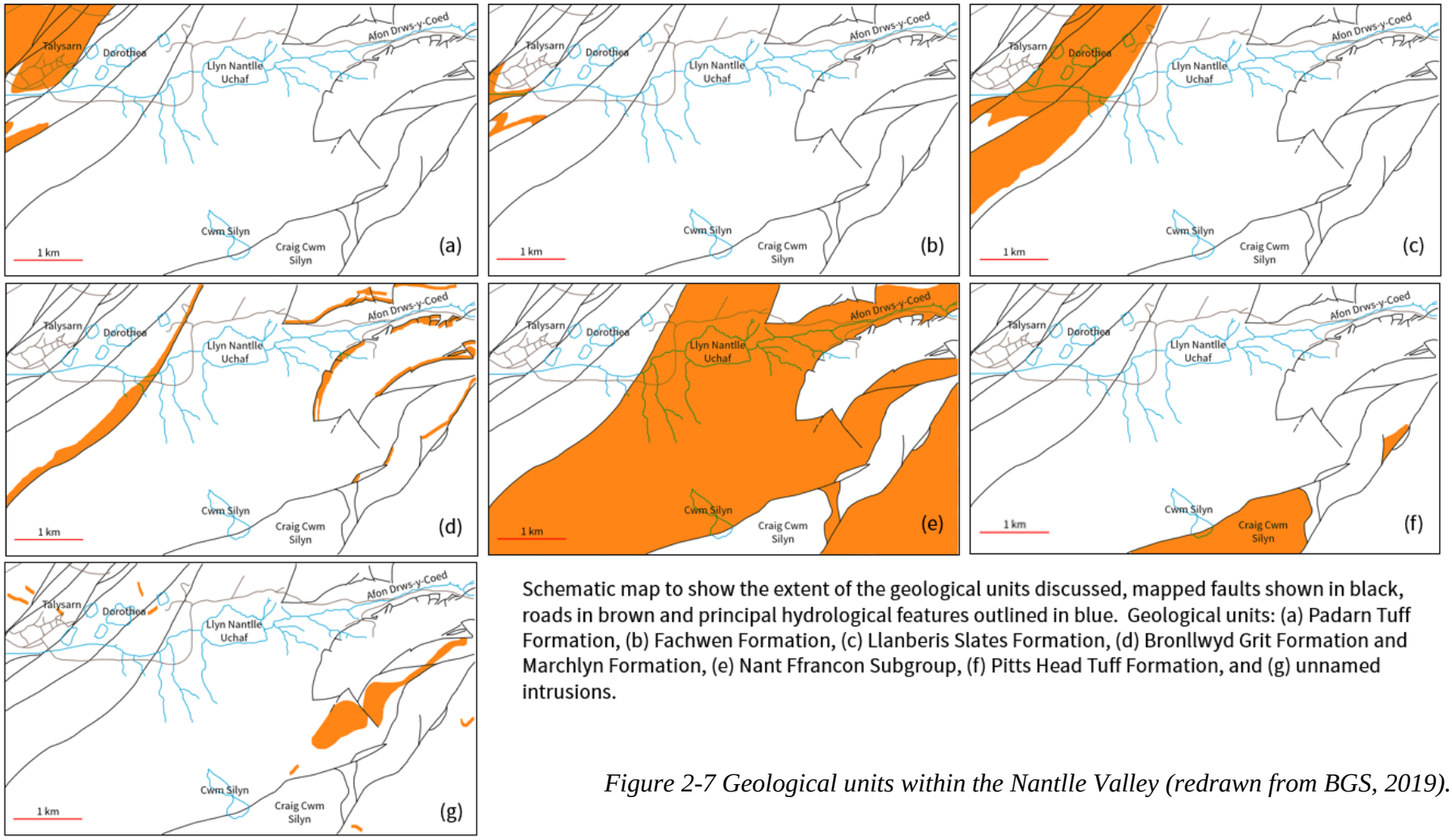

Schematic map to show the extent of the geological units discussed, mapped faults shown in black, roads in brown and principal hydrological features outlined in blue. Geological units: (a) Padarn Tuff Formation, (b) Fachwen Formation, (c) Llanberis Slates Formation, (d) Bronllwyd Grit Formation and Marchlyn Formation, (e) Nant Ffrancon Subgroup, (f) Pitts Head Tuff Formation, and (g) unnamed intrusions.

Figure 2-7 Geological units within the Nantlle Valley (redrawn from BGS, 2019).

2.4 The Arfon Group

2.4.1 The Padarn Tuff Formation

The Neoproterozoic Padarn Tuff Formation is comprised of welded rhyolitic ash-flow tuffs with phenocrysts of quartz and plagioclase and minor air-fall tuffs or rhyolitic lavas (BGS, 2019). The reference section is a road cutting on the south side of Llyn Padarn (BGS, 2019). Although not directly relevant to the Dorothea Lakes development the Formation is included for its context as the basement of the Welsh Basin. The Padarn Tuff Formation is overlain unconformably or paraconformably by the Fachwen Formation (Rushton et al., 2011).

2.4.2 The Fachwen Formation

The Fachwen Formation is an Ediacaran to Comley sequence of sandstones and siltstones, with tuffs and conglomerates (BGS, 2019). Rushton et al. (2011) refers to three subdivisions mapped by Morris and Fearnside (1926) in the Nantlle area: Tryfan Grit, Glog Grit and Cligwyn Conglomerate.

The Fachwen Formation was considered exclusively Cambrian until radiometric dates indicated a Neoproterozoic age (Compston et al. 2002; Schofield et al. 2016). The absence of an unconformity at the start of Cambrian time is highlighted by Rees et al. (2014) as one aspect of stratigraphy yet to be resolved in northwest Wales.

2.5 The Harlech Grits Group

2.5.1 The Llanberis Slates Formation

The Formation comprises silty slates with turbiditic sandstones, some of which have been mapped in the Nantlle area by Morris and Fearnside (1926). Woodcock and Strachan (2002) indicate the turbidite sediment source to be the Irish Sea Landmass to the north,

this is supported by Forshaw (2019). Subdivisions of the Harlech Grits Group in the area were described by Morris and Fearnside (1926) (Table 2.2), which includes the Cymffyrch Grit Group, now the Bronllwyd Grit Formation (Rushton et al., 2011). Morris and Fearnside's (1926) map (Figure 2-9), was prepared when the area's extensive quarries weren't flooded, access easier and exposure considerably better than at present.

Name	Description
Cymffyrch Grit Group	Coarse grits with mudstone beds
Green Slates Group	Green, greenish blue and light brown slates
Mottled Blue Slates Group	Smooth silky red slates over purple slates splashed with irregular green patches.
Pen-y-Bryn Grit Group	Coarse massive grits
Striped Blue Slate Group	Fine grained stripes most abundant in the uppermost and lowermost parts, otherwise a purplish tinge
Dorothea Grit Group	Coarse thickly bedded grits with intercalated thinly bedded white and green banded silts
Purple Slate Group	Including an upper red subdivision with abundant green spots, green stripes of coarse grit

Table 2.2 Morris and Fearnside's (1926) subdivisions of the Nantlle Valley.

Rushton et al. (2011), Rees et al. (2014) and the BGS (1961) refer to a single fossil *Pseudatops viola* near the top of the Formation suggesting an age of <520 Ma and Pothier et al. (2015) refer to a trace fossil, *Teichichnus*. Work by Pothier et al. (2015) included a date determination for detrital grains from the Dorothea Grit from Alexandria Quarry (SH 51834 56078), the youngest of which has a $^{206}Pb/^{238}U$ age of 515 Ma. Other features of

the grit horizons include the presence of bleached rip up clasts (Figure 2-8), erosive bases and features attributable to Boumer sequence subdivisions (Forshaw, 2019).

Figure 2-8 Pale rip up clasts within a grit horizon (SH 50073 53390).

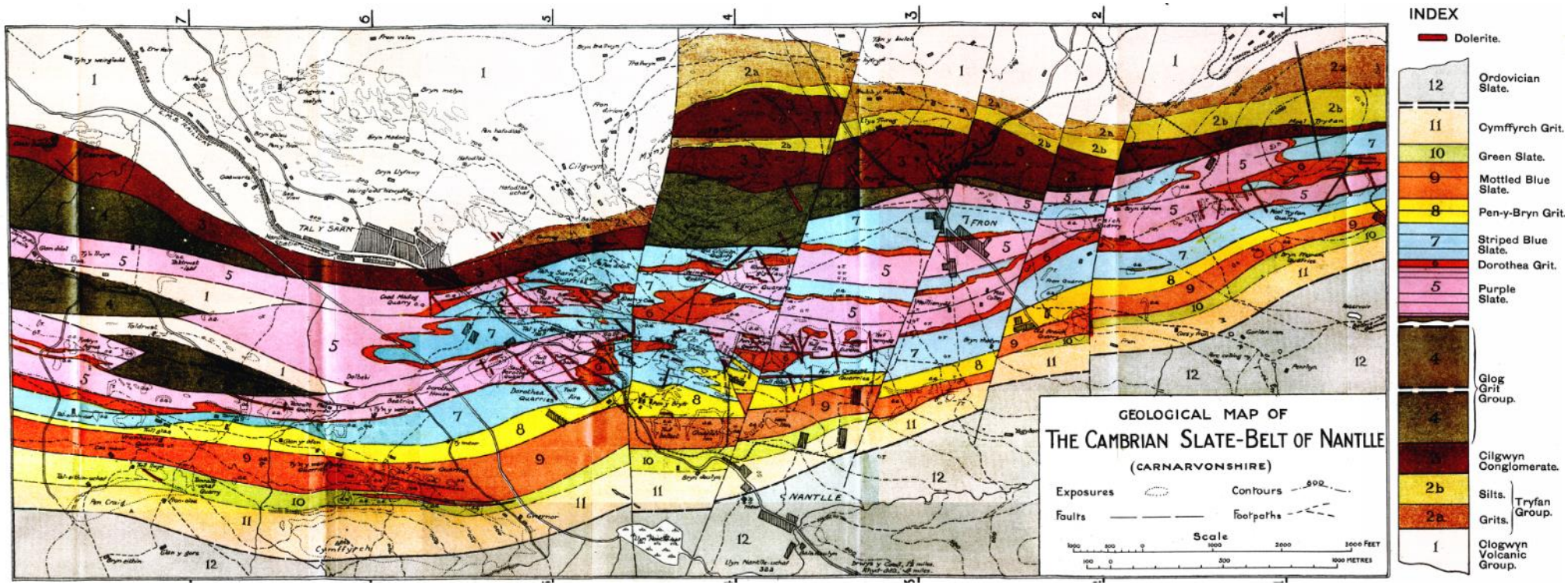

Figure 2-9 Morris and Fearnside's (1926) geological map of the Nantlle Valley.

2.5.2 The Bronllwyd Grit Formation

The transition from the Llanberis Slates Formation to the turbidites of the Bronllwyd Grit Formation is not known. Rushton et al. (2011) highlight differing views on the presence of a hiatus and the absence of fossils to constrain relative ages. The BGS (2019) describe the Formation as coarse-grained sandstones with mudstones and conglomeritic horizons, which is assigned a Series 2 to Furongian (Comley to Merioneth) age. Inclusion of all Miaolingian (St David's) time, which Rushton et al. (2011) highlight as a considerable length of time.

2.5.3 The Marchlyn Formation and Carnedd Y Filiast Grit Member

The Marchlyn Formation conformably overlies the Bronllwyd Grit Formation and is generally coarse grained. Fossils within the Carnedd Y Filiast Grit Member allow correlation with the equivalent units of the Harlech Dome (Rushton et al. 2011).

2.6 The Ogwen Group and the Nant Ffrancon Subgroup

The Ordovician strata comprise the Nant Ffrancon Subgroup, Pitts Head Tuff Formation and various intrusions. In the area of Nantlle the Subgroup underlies the land between the edge of the Valley floor to the foot of Craig Cwm Silyn, before giving way to the Pitts Head Tuff Formation, which forms the escarpment of Craig Cwm Silyn itself. Similarly, the boundary with the Pitts Head Tuff Formation to the south is also faulted (BGS, 1985; 2015; 2019).

The Nant Ffrancon Subgroup is shown by the BGS (1985; 2015; 2019) to be faulted against the Bronllwyd Grit Formation. The Nant Ffrancon Subgroup underlies most of the study area above the valley floor, dips to the southeast and is the least well exposed of the geological units of the study area. The Subgroup is assigned to the Ogwen Group

by Rushton and Howells (1998) and Rushton, et al. (2000) who also included several previously named units within the Subgroup (Table 2.3).

Formation	Subdivision
Allt Lŵyd Formation	Aran Boulder Bed Member
	Garth Grit Member
Bryncroes Formation	-
Llanengan Formation	Hen-dy-capel Ironstone Member
Moelwyn Volcanic Formation	Upper Member
	Lower Member
Penamnen Tuffs Formation	Moelfre Tuff Member
Port Meudwy Formation	
St Tudwal's Formation	Machroes Member
	Pared Mawr Member
	Penrhyn Du Member
	Trwyn yr Wylfa Member
Trygarn Formation	
Wig Bâch Formation	Trwyn Cam Member
	Wîg Member

Table 2.3 Subdivisions of the Nant Ffrancon Subgroup (Rushton and Howells, 1998).

Rushton, et al. (2000) and Woodcock and Strachan (2002) summarise the Floian (Arenig) Stage of the Welsh Basin as a transgressive sandstone facies resting unconformably on gently folded and tilted Cambrian strata. By comparison the Darriwilian (Llanvirn) Stage includes graptolitic mudstones. The Subgroup includes nearshore marine facies near its base giving way to offshore conditions for most of its thickness (Woodcock and Strachan,

2002), comprising predominantly mudstones and siltstones with sandstone, oolitic ironstone and tuff horizons (Rushton and Howells, 1998). The Subgroup includes the Moelwyn Volcanic Formation, which could not be ascribed to one of the main Volcanic Groups (Rushton and Howells, 1998).

2.7 The Snowdon Volcanic Group and Pitts Head Tuff Formation

The Caradoc (Darriwilian to Sandbian) Pitts Head Tuff Formation is a subdivision of the Snowdon Volcanic Group described by the BGS (2019) as a variably welded rhyolitic ash flow tuff. The Formation is divided into intra-caldera and outflow tuffs (Howells and Smith, 1997). The Group is the second of six major phases of Ordovician volcanic activity preserved in Snowdonia (Howells and Smith 1997; Rushton and Howells 1998).

2.8 Intrusions

The study area includes several unnamed dolerite intrusions of Ordovician age (BGS 1985; 2015), which BGS (2019) refer to as microgabbro. Morris and Fearnside (1926) document over seventy dolerite intrusions, all of which were near vertical. The location of intrusions shown on the available maps is limited to the areas surrounding the former quarries. It is therefore not clear if intrusions are genuinely limited to the slate belt or just not exposed elsewhere. A review of available boreholes from the BGS does not clarify this. The mountain of Mynydd Mawr (SH 53978 54680) is shown as an Ordovician microgranite by the BGS (2019) and as a riebeckite microgranite by the BGS (1985).

2.9 Geological structures

The geological structure of Snowdonia is complex and is dominated by events associated with the Basin's development and deformation during the Caledonian Orogeny. Compressional forces that the basin has been subjected to resulted in generally upright

fold structures parallel with the slate belt and a well-defined near vertical cleavage within the slates (Wood, 1974), as seen in Figure 2-11. Reduction spots in the Llanberis Slates Formation (Figure 2-10) can help to identify bedding. Assuming conditions of pure shear and originally spherical reduction zones the resultant strain ellipsoid is always elongated precisely parallel cleavage. Wood (1974) and Owens (1984) used this to calculate strain levels consistent with a halving of length perpendicular to cleavage balanced by a doubling in thickness along the cleavage plane. In the area of the Dorothea Quarries, Wood (1974) calculated a 70% flattening perpendicular to cleavage and highlights that within the samples examined there was considerable evidence of non-uniform strain. Minor faults are reported to be associated with mylonitised surfaces (Figure 2-12).

Figure 2-10 Reduction spots in slate spoil.

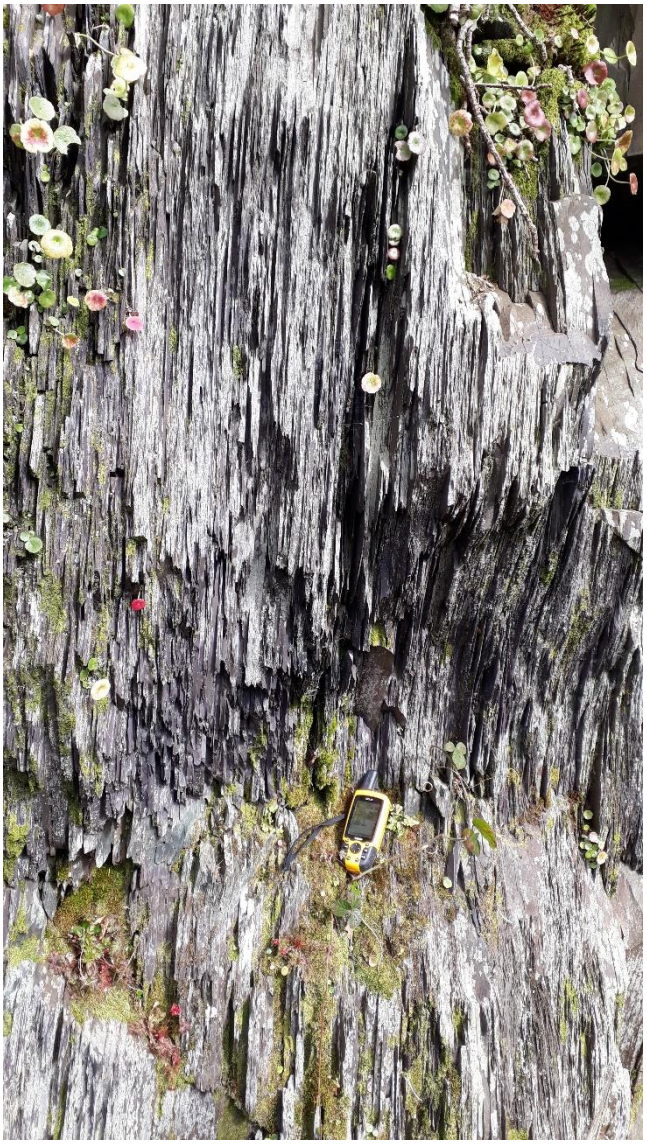

Figure 2-11 Cleavage in the Llanberis Slates Formation (SH 50203 53319).

Figure 2-12 Mylonitised surface exposed on the surface of slate waste.

3 Rock strength, rock mass classification and in-situ stress

3.1 Rock strength and mass classification

This section explains the challenges determining compressive and tensile strength for inherently variable materials and ways to characterise strength anisotropy. Two common rock mass classification systems are discussed to classify mass *behaviour* to aid planning excavation activities and estimating stand up time or support requirements. In section 4 onwards methods to estimate *failure* of rock masses are discussed. Behavioural classification systems are discussed as they predate and shaped the development of rock mass failure criteria. This section concludes with a summary of estimating in-situ stresses.

3.2 Intact compressive strength and anisotropy

Tensile or compressive strength is not an intrinsic property and depends upon orientation, scale, rate of loading and stress regime. The notion of a single strength is therefore somewhat simplistic but necessary to standardise methods of classification. Determining intact strength is difficult as aspects of rock mass fabric often prevent a representative intact strength from being measured (Hoek and Marinos, 2000). In the UK ISO 14689:2017 (BSI, 2018) gives qualitative and quantitative descriptions of rock strength, which are provided in Appendix A. For variable lithologies with differing strengths, Hoek and Marinos (2000) suggest the use of a weighted average to characterise mass behaviour. This may be appropriate for aggregating properties but not when extremes of strength influence excavation safety or behaviour.

Isotropy is rare (Barton and Quandros, 2015), and it needs to be appreciated that sedimentary and metamorphic rocks typically possess pronounced strength anisotropy

(Saeidi, et al., 2014). This may be inherent, from bedding, foliation or schistosity, or an induced anisotropy, from joints and fractures (Ramamurthy et al., 1993). The ratio between maximum ($\sigma_{c(90)}$) and minimum ($\sigma_{c(min)}$) compressive strength defines the anisotropy ratio (R_c) (Equation 3.1), which Saeidi et al. (2013; 2014) explain using Jaeger's expression modified by Donarth (Equation 3.2). This allows intact strength to be estimated for angle β between an isotropic fabric and the major principal stress (σ_1) based on constants D^* and A. This requires UCS (σ_c), or point load index ($I_{s(50)}$) measurements for β angles 0°, 30° and 90°. Ramamurthy et al. (1993) quote work by Singh et al (1989) giving ranges of R_c for different rock types (Table 3.1).

$$R_c = {\sigma_{c(90)}}/{\sigma_{c(min)}} = {I_{s(50)90}}/{I_{s(50)min}}$$

Equation 3.1 Anisotropy ratio from Saeidi et al. (2013).

$$\sigma_{c(\beta)} = A - D^* \cos 2\,(\beta - \beta_{min})$$

Equation 3.2 Strength anisotropy summarised by Saeidi et al. (2014).

R_c	Description	Rock types
1.0-1.1	Isotropic	Sandstones
1.1-2.0	Low anisotropy	Sandstones and shales
2.0-4.0	Medium anisotropy	Shales, slates and phyllites
4.0-6.0	High anisotropy	
>6.0	Very high anisotropy	

Table 3.1 Classification of strength anisotropy given by Ramamurthy et al. (1993).

Intact rock exhibits the greatest compressive strength where the maximum principal stress (σ_1) is perpendicular to the plane of weakness ($\sigma_{c(90)}$ or $I_{s(50)90}$) and the lowest compressive strength where σ_1 is orientated at between 30° and 45° to the potential shear surface. This

corresponds with the maximum shear stress acting along the rock fabric, either in-situ or in a laboratory sample (Figure 3-1) and can be explained in terms of normal and shear stress (σ_n and τ respectively) and matches relationships reported by Tien et al. (2006).

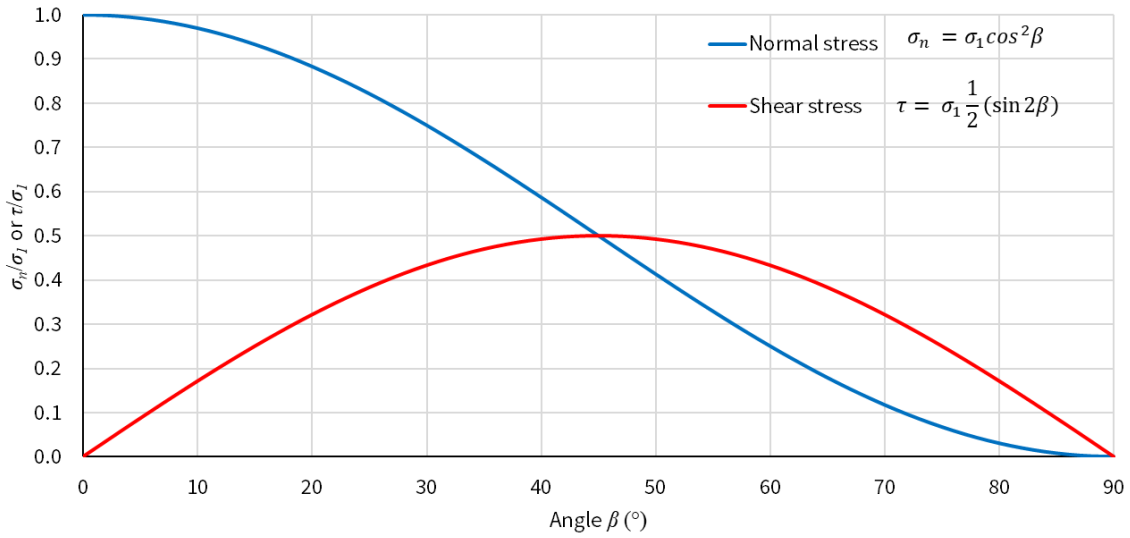

Figure 3-1 Magnitude of shear stress with orientation to maximum principal stress.

3.3 Tensile strength

Griffith (1921) provides an explanation for the anomalously low tensile strength of concrete that is equally applicable to intact rock. The strength of molecular bonds multiplied by the number of bonds to be broken provides a theoretical tensile strength. For intact rock, as with other materials, this theoretical value is greater than the measured tensile strength. Griffith attributed this to far-field stress concentration at the ends of pre-existing microscopic cracks, referred to as Griffith cracks, facilitating local stress concentration, coalescence, and propagation of cracks (van der Pluijm and Marshak 1997; Hudson and Harrison 1997; and Cai 2010).

Regardless of scale, stress concentration occurs in compression or tension around any opening without internal support, be it a pore space or tunnel. For a circular opening the

maximum stress increase in the wall of the opening is three times the far field stress (Hoek and Brown, 1980). For elliptical openings stress increase at the extremities of the ellipse is proportional to its axial ratio. A finite crack represents an extreme form of ellipse with very high length:width ratio, resulting in much higher stress concentration. Plastic yielding, at the crack tip facilitates tension crack propagation (van der Pluijm and Marshak, 1997).

With reference to very high vertical rock slopes Barton and Shen (2018) provide a method that can be used to estimate the minimum tensile strength required to sustain such slopes. Applying this to the steep and unweathered sides of Dorothea Quarry (Equation 3.3) for an assumed critical height (H_{crit}), in metres, equal to the current slope height and adopting a Poisson's ratio (ν) = 0.2 and γ = 2.79 tons/m^3 for the Llanberis Slates Formation (Table 3.3) a minimum σ_t = 0.64 MPa is required for a 115m high near vertical rock wall. This is less than the minimum value of σ_{tB} of 2.61 MPa recorded from elsewhere in the slate belt (Table 3.3).

$$H_{crit} = {}^{100\,\sigma_t}/_{\gamma\,\nu} \quad or \quad \sigma_t = {}^{H_{crit}\,\nu\,\gamma}/_{100}$$

Equation 3.3 Critical slope height based on Barton and Shen (2018).

3.4 Conjugate fabrics and the critical state concept

Irrespective of stress level Coulomb failure assumes a constant dihedral angle between conjugate failure surfaces and provides a method of quantifying shear failure in terms of cohesion (c) at zero normal stress and internal friction (φ) (Muehlberger, 1961). At failure cohesion is exceeded, and the failure envelope is tangential to Mohr's circle with a slope equal to $tan\ \varphi$ from the onset of friction. Peak strength values are mobilised at larger strain levels as stress increases. After cohesion has been overcome, friction remains but

dilation continues to even greater strain levels (Barton, 2014). While Coulomb failure will be independent of any existing fabric or texture within the rock the stress regime causing Coulomb failure can preserve conjugate joints to be developed. The relationship between conjugate failure surfaces (Figure 3-3) is shown as Figure 3-2, where the value of angle θ is given by Equation 3.4.

$$2\theta = 90 + \varphi \quad \text{or} \quad \theta = 45 + \left(\frac{\varphi}{2}\right)$$

Equation 3.4 Relationship of angle θ to φ.

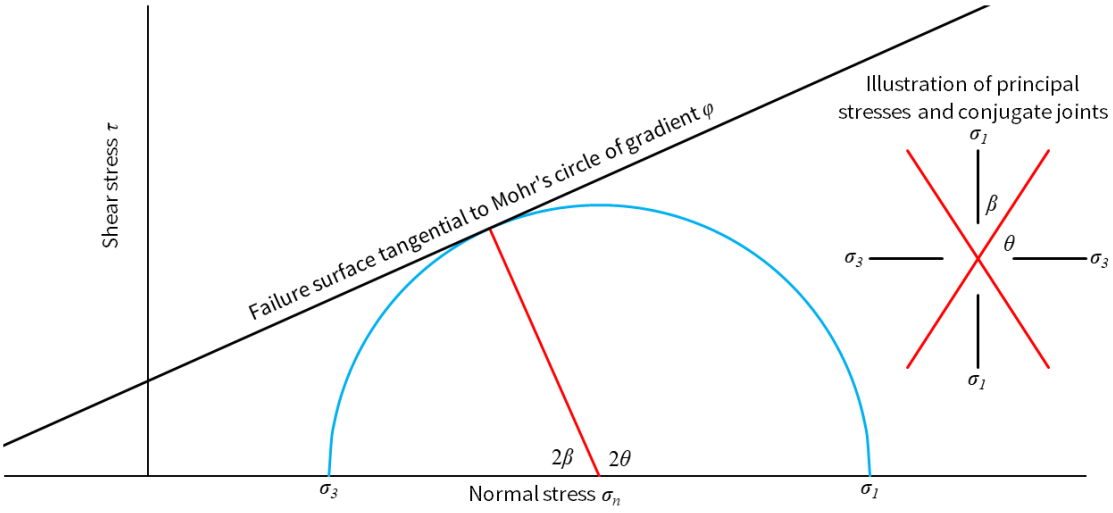

Figure 3-2 Mohr's circle, Coulomb failure envelope and dihedral angle, 2β.

Figure 3-3 Apparently conjugate joints in an adit within the Llanberis Slates.

In reality the slope of the failure envelope is not linear over all stress levels and is parabolic with symmetry along the abscissa, however simplification to a straight line is often a reasonable approximation, especially over a limited range of stresses. A non-linear failure envelope may be ascribed Mohr-Coulomb parameters for a given stress level, by adopting an instantaneous friction angle (φ_i) and instantaneous cohesion intercept (c_i) (Hoek 2006) (Figure 3-4). Prasssetyo et al. (2017) refer to a secant (φ_s) or tangent friction angle (φ_t) for the same purpose: defining the point of failure on a non-linear strength envelope. Figure 3-4 shows that at low values of σ_n angle φ_i is relatively high and c_i relatively small, but as σ_n increases there is an initial reduction in φ_i and c_i increases.

With increased normal stress beyond the UCS the failure envelope flattens out completely irrespective of the confining stress, at which point a critical state condition has been reached (Barton 2014; Pothier et al. 2015; Singh and Barton 2019; Shen et al. 2020).

Once reached the critical state does not allow deviatoric stress or frictional strength to increase and the material has passed through the brittle-ductile transition (Singh and Barton, 2019). The critical state condition is shown within Figure 3-4 as occurring where internal friction degrades to 26° and σ_1 is three times σ_3, which is typical of the behaviour of most rocks and rock masses (Barton 2014; Shen et al., 2020).

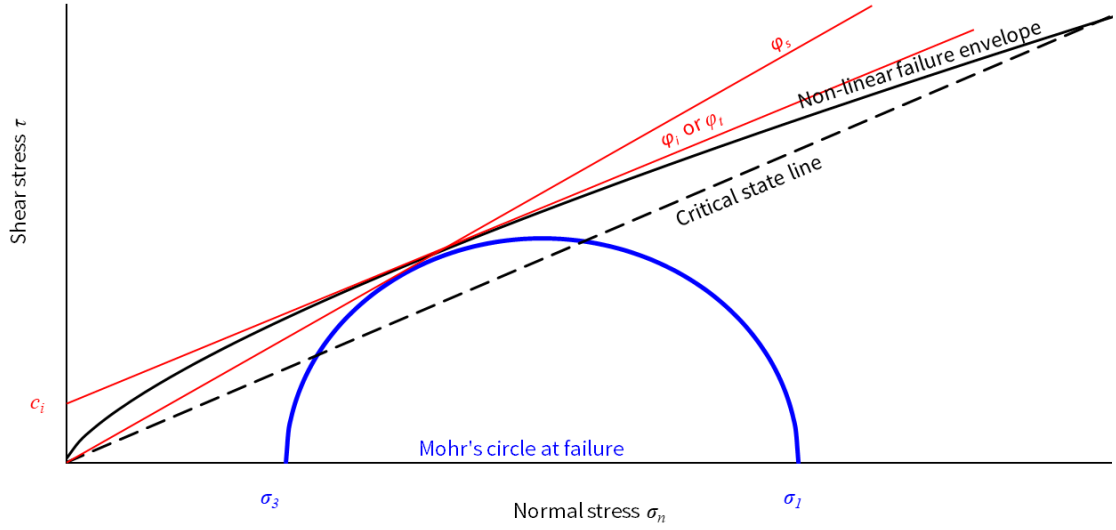

Figure 3-4 Mohr-Coulomb plot with instantaneous and secant frictional parameters.

3.5 Rock mass behaviour and classification systems

Rock mass strength and behaviour may be comparable to a completely broken mass of individual particles best considered by soil mechanics or as a monolithic and largely intact mass. The range of intact strengths and strength anisotropy is further complicated by discontinuities and in-situ stresses.

At low stress levels instability is governed by the presence and orientation of discontinuities. At higher stress levels failure may still be controlled by the joints but may be closer to the intact strength (Hoek, 2006). At yet higher stress levels still, failure may propagate through the intact material and be independent of pre-existing weaknesses.

Different classification systems have been developed for a variety of purposes, driven by the need to estimate cost and plan for the likely method of excavation as well as temporary and permanent reinforcing or support requirements. The two common English speaking classification schemes for estimating reinforcing, support requirements or stand-up time are Bienawski's Rock Mass Rating (RMR) and the Norwegian Geotechnical Institute's Q-system (Hoek, 2006). Both systems were developed from experience tunnelling in a range of rock masses, use relatively few parameters relating to geometry and mechanical condition of the rock mass and have an element of subjectivity (Hudson and Harrison 1997; Bertuzzi 2019). There are limitations in stratified rocks, differing stress levels and in accounting for block shape (Hudson and Harrison, 1997). According to Hoek (2006) the crossover of RMR from civil engineering to mining applications led to the criticism that it was overly cautious.

In the case of RMR, parameters are scored, then summed and adjustment made for the beneficial or detrimental effect for discontinuity orientation, resulting in a score between 0 and 100, allowing subdivision into five classes of rock. By comparison the more complex Q-system has a semi-logarithmic score ranging between 0.001 and 1000 and nine rock quality classes. Barton (2015) suggests that by normalising a Q-value there are potentially eight orders of magnitude available from the Q-system.

The classifier and end user must appreciate the limitations of either system. Marinos et al. (2005; 2007) point out that structural orientation as well as the role of groundwater and stress regime utilised in both systems are specifically dealt with by post-classification design of an excavation. Both stress and groundwater may also be changed by the excavation process, thereby altering the original classification.

The extensive use of RMR or Q-system for the successful construction of extensive tunnels and caverns worldwide shows the potential suitability of both methods. Marinos et al. (2005) suggest this is because they are best suited to moderate stress levels and RMR values of 30 to 70. However, where squeezing or rock bursts are likely, in high stress environments or in poor quality rock, or where progressive failure is possible the methods are unsuitable.

Both systems utilise RQD (rock quality designation), which is the percentage length of solid core free from joints with a length ≥0.1 m (Figure 3-5) (BSI, 2015). Using RQD as an input parameter is useful as it is easily measured from cores or determined from a scanline.

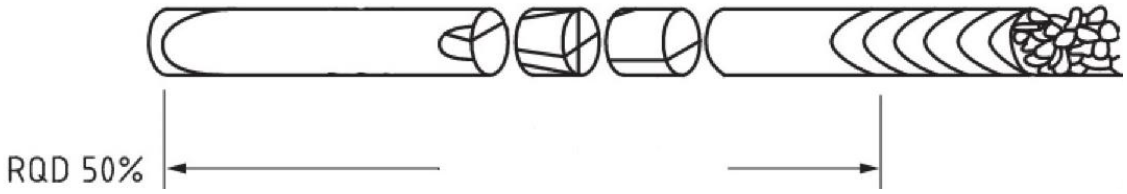

Figure 3-5 RQD from core length (modified from BSI, 2015).

Hudson and Harrison (1997) show that RQD is relatively insensitive to joint spacings >0.3 m, with mean spacing >0.3 m always giving RQD values >95%. Ignoring core lengths <0.1 m creates a situation where cores with uniformly spaced joints at 0.09 m and 0.11 m achieve an RQD of 0% and 100% respectively for no meaningful change in rock quality (Palmstrom, 2005). According to Marinos et al. (2005) an RQD of zero is meaningless and should not be included in a classification system.

As RQD is a one-dimensional measurement susceptible to anisotropic bias, which is one reason Barton (2015) recommends it as a useful tool for quantifying anisotropy. The inclusion of RQD in any classification requires consideration, especially where highly

fractured, low RQD rocks, are present (Marinos et al., 2005). Essex (2007) discourages the use of classification systems to describe baseline conditions, preferring non-subjective testing of the ground's properties with reference to specific test requirements. It is not clear how RQD should be treated in this respect as it is easily measured and but highly susceptible to orientation bias.

3.6 In-situ stress

Determining in-situ stress is the hardest of all parameters to measure or estimate (Hoek, 1999) as theoretical estimates prove unreliable (Hoek, 2006). Knowledge of in-situ stress is required for engineering design and analysis purposes and to understand the effect of stress redistribution around an excavation. Stress redistribution may cause block tightening or loosening, referred to as clamping forces by Hoek (2006), or result in the rock mass being bought to the point of failure.

In-situ vertical stress, usually the minimum principal stress (σ_3), can be estimated as the product of mean unit weight (γ) and depth of overburden (H). The assumption of a mean unit weight of 27 kN/m^3 is consistent with lithostatic stress measured from mining and civil engineering projects worldwide (Hoek and Brown, 1980; Hoek, 2006).

Horizontal stresses are considerably harder to estimate as these may be a product of regional tectonics, topography, and anthropogenic effects such as excavation. The World Stress Map is of limited use to civil engineers working in the uppermost few hundred metres of the earth's crust (Hoek, 1999). Hoek (1999; 2006) refer to an elasto-static thermal stress model developed by Sheorey (1994) that has reasonable accord with measured horizontal stress summarised by Hoek and Brown (1980) from very deep mining and tunnelling. Hoek (2006) recommends that in-situ stresses should be measured

where sensitivity studies indicate that this is likely to affect the behaviour of underground excavations, although notes that measurements within 50 km may be of some use.

With respect to stress changes: these may be due to stress redistribution from forming the excavation itself (Figure 3-6) as well as an increase in effective stress from seasonal effects or from draining of the rock mass or to facilitate excavation.

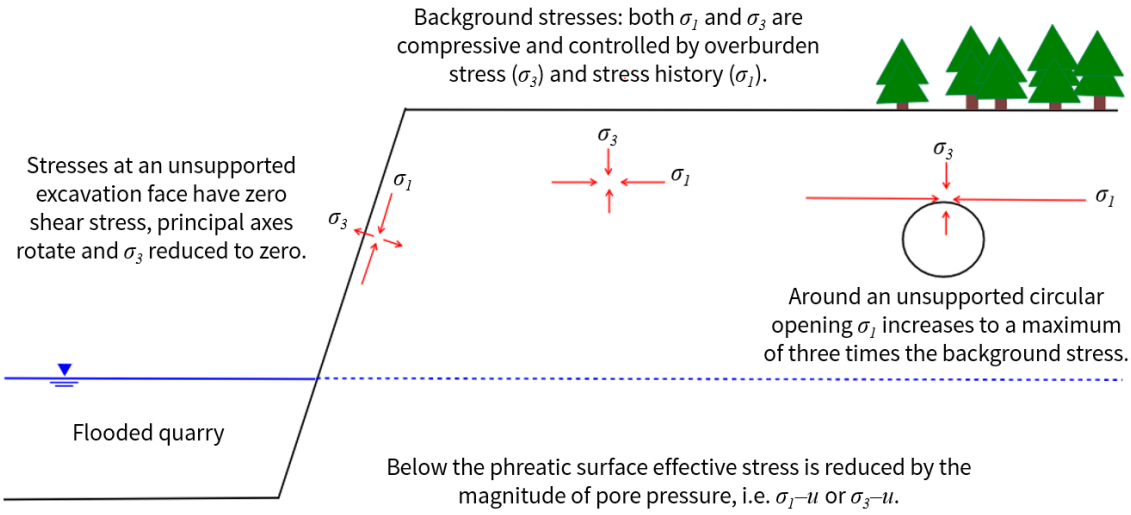

Figure 3-6 Illustration showing changes in the orientation of principal stresses.

Knowing or estimating changes in vertical (σ_{zz}) or horizontal stresses (σ_{xx} and σ_{yy}) from excavation related unloading allows Hooke's law to be used to quantify elastic strain (ε_{xx}) based on Poisson's ratio (ν) and Young's modulus (E) (Equation 3.5). For an initial state of triaxial compression an element of rock in the ground subject to horizontal stress relief from adjacent excavation results in σ_{xx} being reduced to zero immediately adjacent to the excavation. The resulting horizontal strain may be accommodated purely elastically or concentrated at new or existing discontinuities (Figure 3-7). Although not formed in a truly tensile regime such fractures achieve the greatest surface roughness and friction angle (Barton, 2014). Such fractures will likely be perpendicular to maximum stress

relief. In the case of a near vertical rockface, such fracture may be subparallel to the rockface and themselves subvertical. This provides an explanation for the development of potential dislocation surfaces roughly parallel to the face of a subvertical rock face of significant and unbenched height.

$$\varepsilon_{xx} = {}^{1}/_{E}\,\sigma_{xx} - \nu(\sigma_{yy} + \sigma_{zz})$$

Equation 3.5 Hooke's law.

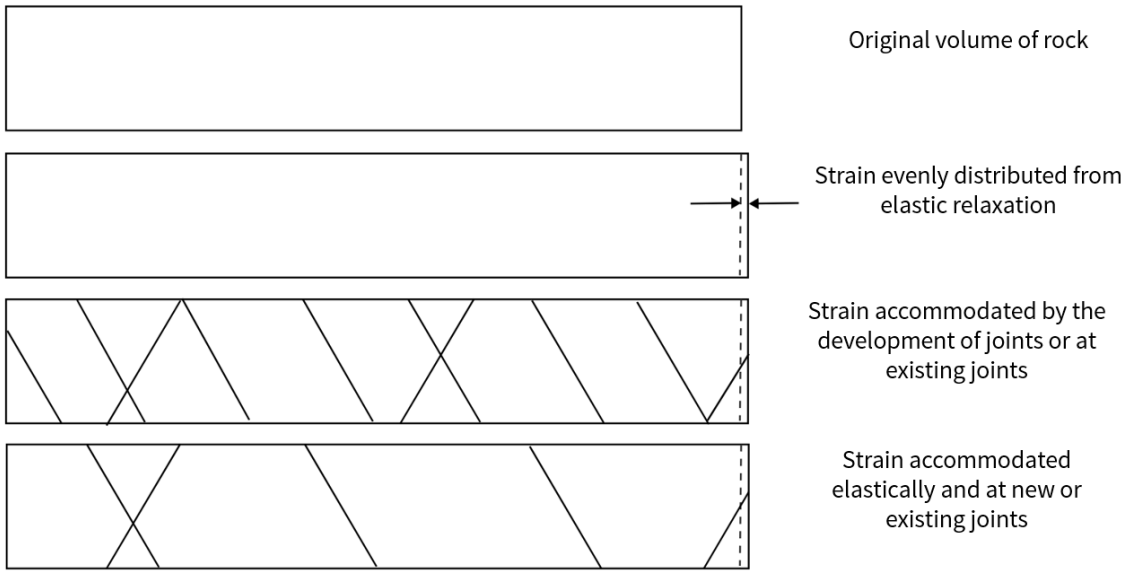

Figure 3-7 Methods of accommodating strain.

By way of an example a spreadsheet was used to determine a profile of lithostatic stress (σ_{zz}) based on γ = 27.9 kN/m^3 (Table 3.3). As the original horizontal stress components σ_{xx} and σ_{yy} are not known, different scenarios were considered for a coefficient of horizontal stress (ratio of horizontal to vertical stress) k_h = 1.0, 1.5, 2.0 and 2.5 (Figure 3-8). The reduction of σ_{xx} to zero associated with quarry excavation allows ε_{xx} to be calculated based on Equation 3.5 (Figure 3-9). Adopting values of v = 0.2 and E = 50 GPa the strain levels related to horizontal relaxation of the rock mass towards the quarry can be calculated (Figure 3-10). With reference to Figure 3-10, note the negative sign convention as calculated strains are tensile. Values of v = 0.2 and E = 50 GPa are based

on based on the stiffness parameters determined from a trial excavation at Dinorwic, discussed in section 3.7.1 and Appendix D.3.7.

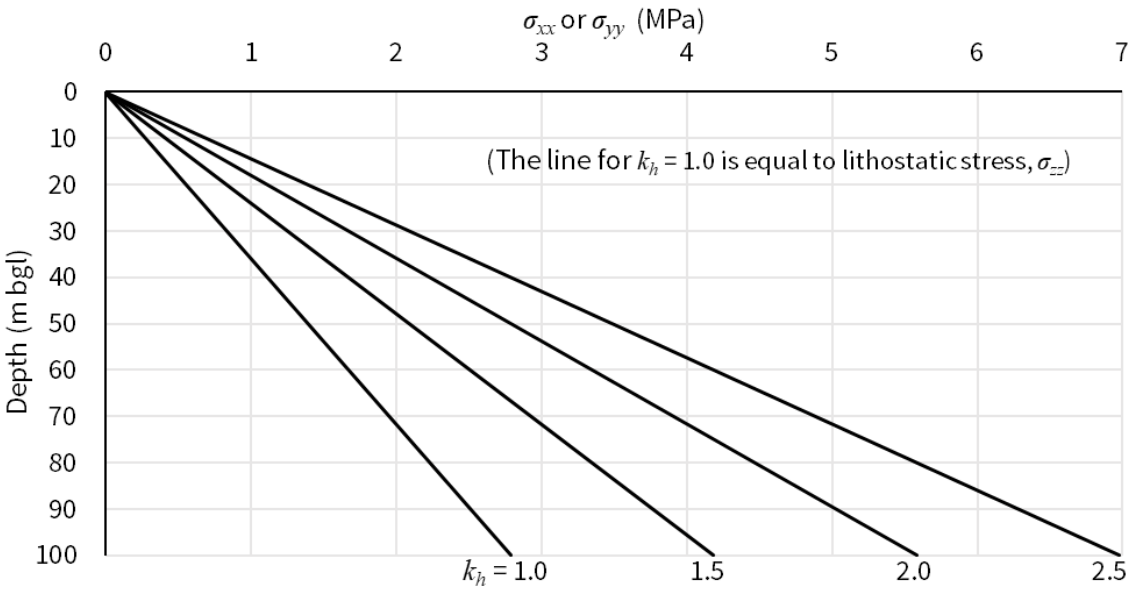

Figure 3-8 Estimation of horizontal stress based on lithostatic stress.

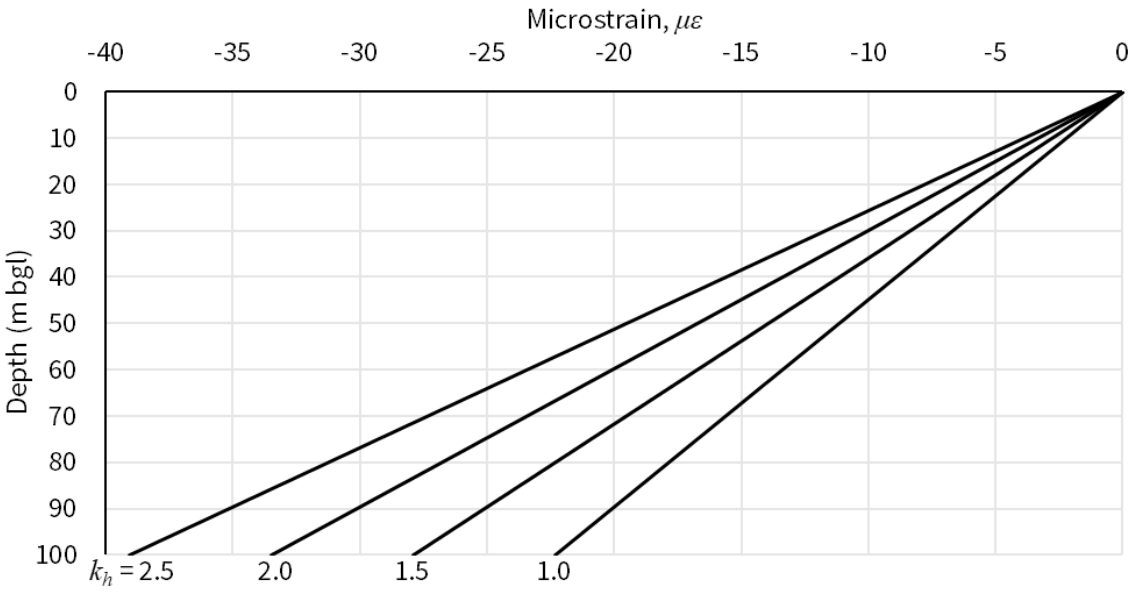

Figure 3-9 Estimation of strain level, expressed as microstrain.

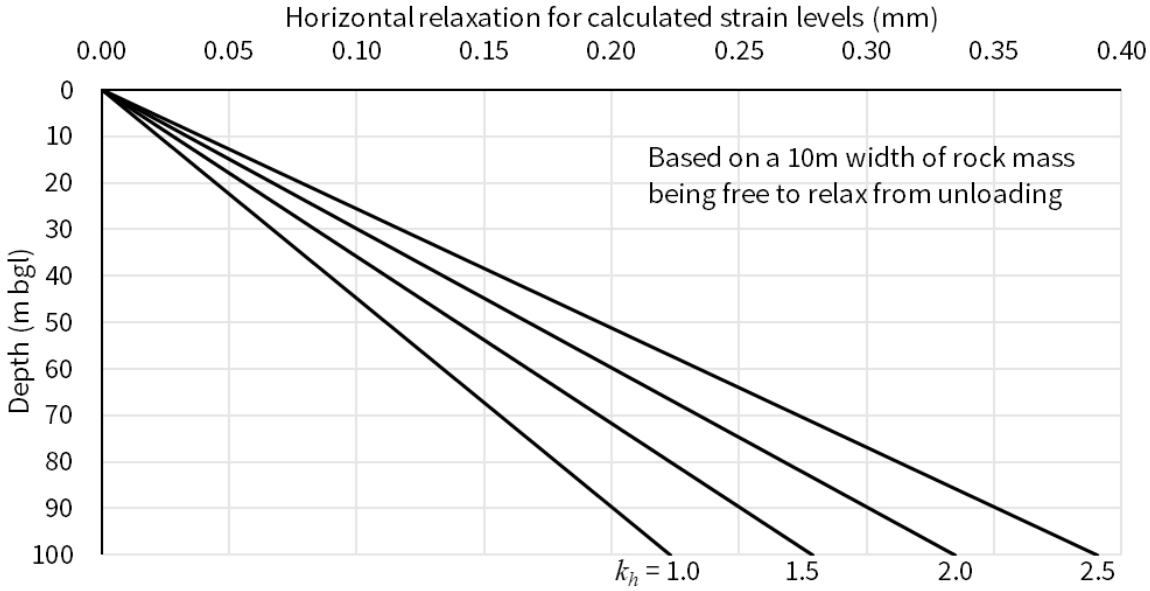

Figure 3-10 Estimated displacements in response to unloading.

3.7 Documented rock and rock mass behaviour

3.7.1 Dinorwic: strength, stiffness, and stress measurements

Dinorwic is an 1800 MW pumped storage scheme that was completed in the 1980s in the Llanberis area in ground conditions directly comparable to Dorothea Lakes (Figure 2-5). The scheme required extensive tunnelling and the construction of nine underground caverns, the largest, the Machine Hall, is 180.3 m long with an unsupported clear span of 24.5 m and height of 59.7 m.

Douglas et al. (1983) summarise a trial excavation of part of the Machine Hall roof and provides a summary of ground conditions and design parameters used (Table 3.2). Back analysis of the trial excavation during December 1976 and January 1977 confirmed a rock mass modulus in the range 50 to 60 GPa. The caverns were excavated within the Llanberis Slates Formation, which were associated with several near vertical metadolerite dykes, the margins of which are hornfels and sheared. Five main discontinuity sets were

described along with bedding and various faults. Discontinuities were noted as being planar, very smooth, continuous at the scale of the caverns excavated and associated with clay or surface alteration. The dykes were reported to be barriers to water, but the margins are associated with higher permeabilities. West and Ewan (1981) report the presence of altered Caledonian and Tertiary dolerite dykes. It is not clear what the basis for the intrusions being assigned as a Tertiary age is a s the only terrestrial Welsh Palaeogene intrusion is at Wylfa Head, Anglesey, according to King (2016).

Parameter	Value
In-situ stresses (dip/azimuth) (from a combination of over cored boreholes and flat jacking)	σ_1 = 18 MPa 26°/300° σ_2 = 8 MPa 26°/198° σ_3 = 6 MPa 52°/074°
Rock mass modulus Poisson's ratio	50 GPa 0.2
Rock density (all types)	28 kN/m^3
Dolerite UCS Slate UCS (β angle dependent)	80 to 180 MPa 20 to 110 MPa
Shear strength of discontinuities	φ = 30° and c = 0 kPa

Table 3.2 Design parameters used for the design of the Machine Hall at Dinorwic.

3.7.2 Strength and stiffness relationships from Glyn Rhonwy

The Glyn Rhonwy Quarries are a chain of former slate quarries located in the Gwynedd Slate Belt approximately 14 km to the northeast of Nantlle and 1.5 km to the northwest of Llanberis (Figure 2-5). An initial phase of ground investigation for another proposed pumped hydropower scheme has been made available to the author (Quantum

Geotechnical, 2015) courtesy of Quarry Battery Company. A geological map of the scheme (Figure 3-11) shows the proposed tunnel alignment is within the Llanberis Slates Formation and Dorothea Grit.

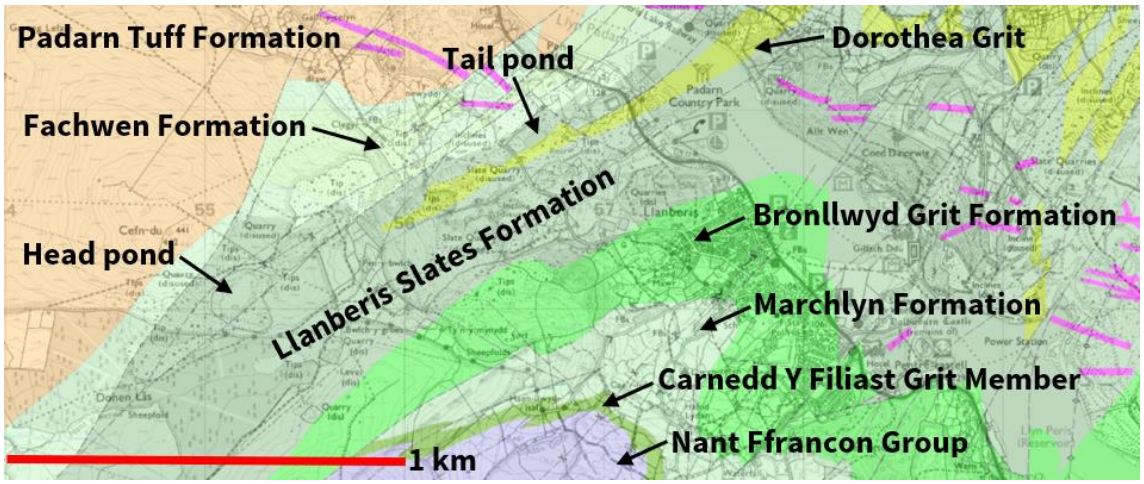

Figure 3-11 Geological map of the Glyn Rhonwy Quarries (Digimap).

Available testing includes, $I_{s(50)}$, UCS, Brazilian tensile tests and measurements of Young's modulus. A summary of the results and potential relationships are shown in the Tables below.

Name	Tests	Range	Mean	Standard deviation
Dry density (Mg/m³)	215	2.27 - 3.84	2.79	0.284
Point load index (MPa)	161	0.36 - 11.24	4.88	2.28
UCS (MPa)	85	5.1 - 163	55.4	35.6
Brazilian tensile strength (MPa)	26	2.61 - 43.6	9.24	8.03
Measurement of Young's modulus (GPa)	23	7.3 - 248.5	75.6	61.4

Table 3.3 Testing summary from review of Quantum Geotechnical's (2015) data.

Name	Range	Mean
Ratio of UCS : $I_{s(50)}$	1.9 – 35.0	11.7 from 63 tests
Ratio of UCS : Brazilian strength	1.97 – 13.2	6.4 from 24 tests
Ratio UCS : Young's modulus	221 - 6398	1833 from 24 tests

Table 3.4 Relationships for strength and deformation testing determined observed.

Where UCS and point load tests were undertaken close to one another (Quantum Geotechnical, 2015) the results have been plotted and presented as Figure 3-12. Figure 3-13 provides a comparison of UCS tests undertaken close to Brazilian tests to give a comparison between compressive and tensile strength. A comparison of UCS results and measured values of Young's modulus is provided as Figure 3-14 to compare strength and stiffness.

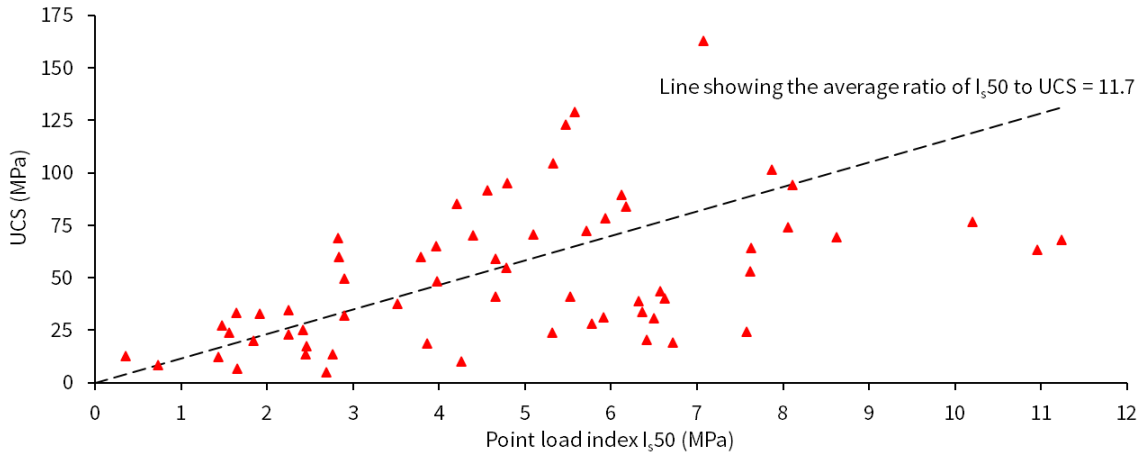

Figure 3-12 Comparison of UCS and $I_{s(50)}$ results.

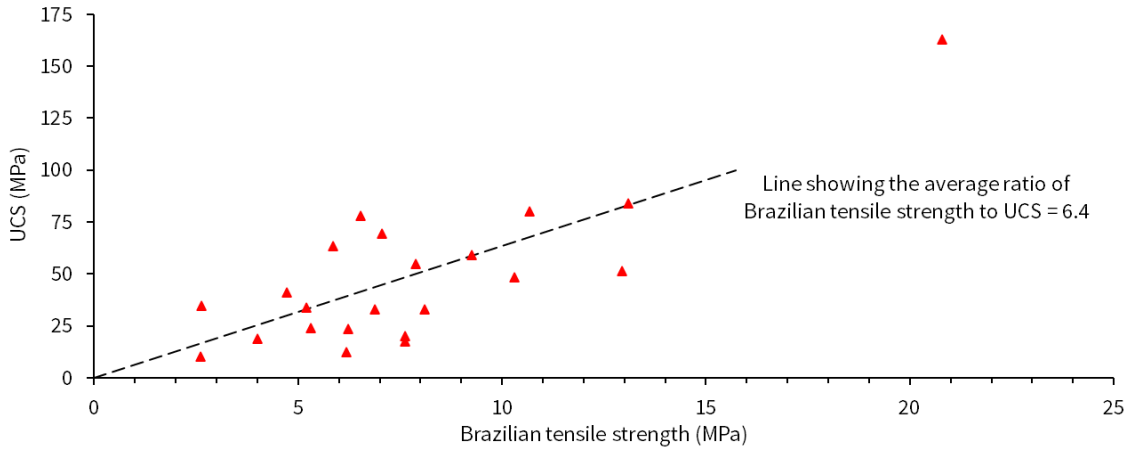

Figure 3-13 Comparison of UCS and Brazilian results.

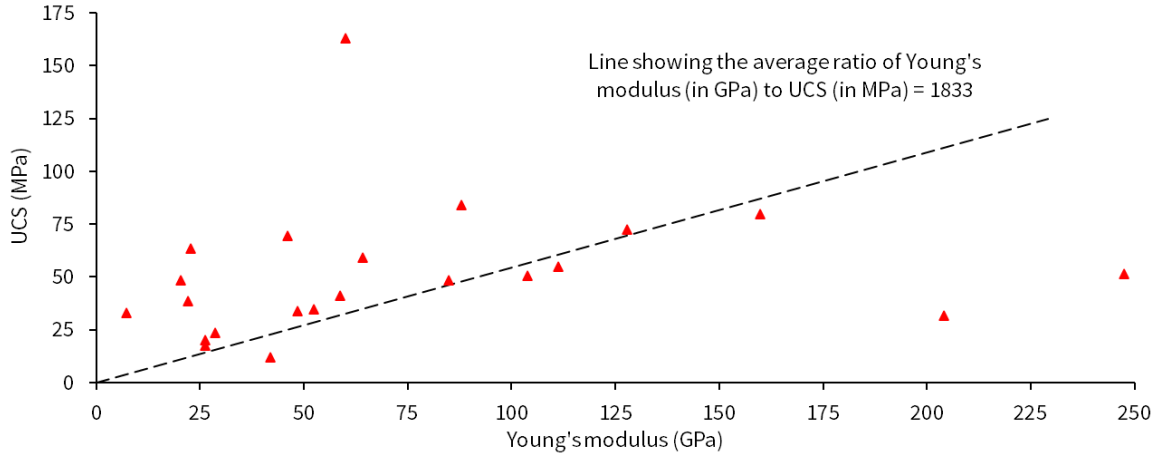

Figure 3-14 Comparison of UCS and Young's modulus results.

Information from Dinorwic and the Glyn Rhonwy Quarries has been reviewed to allow later comparison of reported properties with numerical simulation of non-linear behaviour of the Llanberis Slates Formation. The next section introduces a failure criterion for jointed rock masses: the Generalised Hoek-Brown criterion.

4 The Hoek-Brown failure criterion

4.1 Development of the Hoek-Brown failure criterion

The original Hoek-Brown criterion (Hoek and Brown, 1980) expands on Griffith crack extension theory, was based on extensive testing of a wide range of rock types and is summarised along with subsequent developments by Hoek and Brown (2018). The criterion provides a non-linear failure envelope for jointed brittle rock masses in terms of σ_1 and σ_3 for shear failure in a state of triaxial compression. Combined with the input of geological characteristics from the Geological Strength Index (GSI) (section 5), it allows intact or disintegrated rock mass behaviour to be described mathematically and treated as a mechanical continuum (Marinos et al., 2005).

Since 1980 the criterion has been expanded from hard rock tunnels and other underground excavations to include slopes and foundations (Hoek and Brown, 2018) and "*has become an indispensable tool for rock engineers*" (Colak and Unlu, 2004 p1045). The failure criterion has been used extensively for the successful prediction of rock mass behaviour in numerical simulations, closed form solutions or limit equilibrium analyses for civil engineering and mining purposes. According to Eberhardt (2012) the criterion provides a straightforward method of determining mass properties from laboratory tests. Barton (2014), however, considers the criterion to be unnecessarily complex and lacking clarity.

Unusual uses of the criterion include the use of terrestrial strength analogues by Neuffer and Schultz (2019) to back analyse 8 km high rock slope failures on Mars, allowing the identification of tectonic or impact related seismicity, rather than liquid water, as the trigger of slope instability. A use documented by Thomas et al. (2019) explains the

stability of ancient and contemporary volcanic edifice slopes, including the Pitts Head Tuff (D. N. Petford, pers. comm. 2020).

4.2 Generalised Hoek-Brown criterion

The original criterion was revised as the Generalised Hoek-Brown criterion (Hoek, et al., 2002), and is shown as Equation 4.1. The strength of intact rock is considered by the term σ_{ci} (unconfined compressive strength). Hoek and Brown (2018) make the distinction between σ_{ci}, where σ_3 can be controlled in a triaxial cell, and a UCS test with no confining stress (σ_c). This distinction is unique to the Hoek-Brown criterion and the associated advanced triaxial tests developed to determine both σ_{ci} and a petrographic constant m_i.

$$\sigma_1 = \sigma_3 + \sigma_{ci} \left(m_b \frac{\sigma_3}{\sigma_{ci}} + s \right)^a$$ *Equation 4.1 Generalised Hoek-Brown criterion.*

$$m_b = m_i \exp\left[\frac{(GSI - 100)}{(28 - 14D)}\right]$$ *Equation 4.2 Rock mass constant m_b.*

$$s = \exp\left[\frac{(GSI - 100)}{(9 - 3D)}\right]$$ *Equation 4.3 Rock mass constant s.*

$$a = \frac{1}{2} + \frac{1}{6}\left(e^{-GSI/15} - e^{-20/3}\right)$$ *Equation 4.4 Rock mass constant a.*

4.3 The constants: a, s and m_i

The shape of the failure envelope is defined by the criterion's three constants a, s and m_i, for intact rock a = 0.5 and s = 1. Bulk rock mass property (m_b) is determined using Equation 4.2 using m_i, GSI and a disturbance factor D.

Variation in m_b is shown as Figure 4-1 as a ratio of m_b/m_i for different values of GSI and D. For GSI = 100 Figure 4-1 shows $m_b = m_i$; the rock mass acts as intact material. Bertuzzi et al. (2016) suggest that intact behaviour occurs where GSI > 90 and Marinos et al. (2005) suggest that at depths >1,000 m joints become so tight that intact behaviour prevails and GSI becomes meaningless. Priest (2010) notes that depending on the value of s and where σ_3 is zero the calculated strength of the rock mass will be less than the value of σ_{ci}.

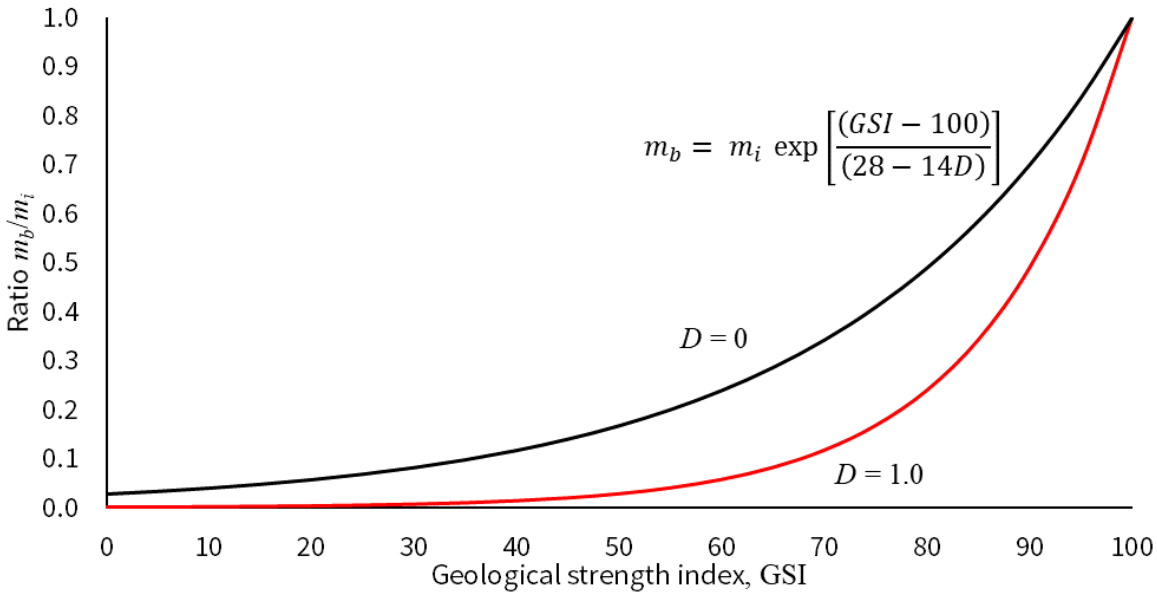

Figure 4-1 Ratio of m_b to m_i for different values of GSI and disturbance factor D.

4.4 Petrographic parameter m_i

m_i via variation in m_b is the primary control on non-linearity. m_i is determined from advanced triaxial tests (Hoek and Marinos 2000) or where such testing is not available it can be reliably estimated from qualitative descriptions (Hoek and Brown, 1997). Published values of m_i are tablulated in Appendix B, which shows the dimensionless value of m_i generally increasing with grain or crystal size varying from 4 to 44. Figure

4-2 shows the effect on strength from changes in m_i. Other controls on m_i are the degree of inter-particle interlock and friction (Colak and Unlu, 2004) as well as mineral content and foliation (Cai, 2010). Eberhardt (2012) points out that the higher the value of m_i the steeper the failure envelope and higher the instantaneous friction angle at low stresses. Saeidi et al. (2014) suggest that the value of m_i is ubiquitous and independent of orientation, even if strength is not.

With reference to published values of m_i Hoek and Marinos (2000) point out that the term "granite" is an unambiguous rock type whereas "breccia" is less prescriptive. In their view, this results in a greater range of published values of m_i for less prescriptive rock types. The distinction between weathering, a near surface process, and alteration by other geological processes was also made.

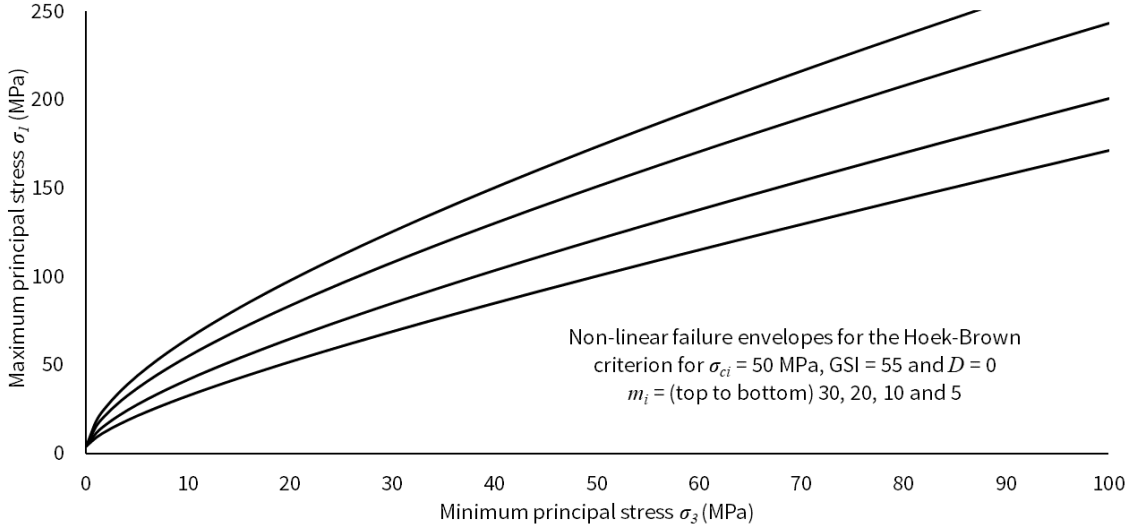

Figure 4-2 Effect of variations in m_i on predicted strength.

The value of m_i is discussed in relation to UCS by Cai (2010), who uses Griffith's theory to show that for $m_i \geq 8$ the ratio of crack initiation stress in compression testing ($\sigma_{c(i)}$) to tensile strength is approximately equal to m_i. Direct tension tests (σ_{ti}) are difficult to

prepare, and the alternative Brazilian test (σ_{tB}) is not without limitations, which Bertuzzi (2019) suggests gives values 10% to 30% higher than direct tension tests. Most published relationships between compressive and tensile strength utilise the Brazilian test for convenience. Cai (2010) suggests that the relationship given in Equation 4.5 is of use in strong brittle rocks in the absence of advanced triaxial tests but with an abundance of UCS and Brazilian tests where $\sigma_{ci} \geq 8\sigma_{ti}$ (or $8\sigma_{tB}$). As the value of $\sigma_c \neq \sigma_{c(i)}$ comparison of the ratio of UCS to tensile strength alone is not relevant apart from knowing that the ratio of $\sigma_c{:}\sigma_t > \sigma_{c(i)}{:}\sigma_{t(i)}$.

$$8\sigma_{ti} \approx 8\sigma_{tB} \approx \sigma_{c(i)} \approx m_i$$

Equation 4.5 Relationship of tensile and compressive strength to m_i based on Cai (2010).

The difference between σ_c and $\sigma_{c(i)}$ is explained by Griffith's principles whereby further stress increase is required after crack initiation ($\sigma_{c(i)}$) to cause yielding (σ_c) (Cai, 2010). This contrasts with tensile behaviour where the threshold for crack initiation is very close to the tensile strength ($\sigma_t \approx \sigma_{t(i)}$). Hudson and Harrison (1997) and Cai (2010) explain that the energy released from crack initiation in tension is sufficient to sustain crack propagation and permit failure.

Colak and Unlu (2004) provide a summary of the variation of m_i with changes in intact strength for transversely isotropic rocks based on UCS and either direct tensile tests (σ_{ti}) or based on the Brazilian test (σ_{tB}) (Equation 4.6).

$$m_i = {}^{\sigma_{ti}}/_{\sigma_{ci}} - {}^{\sigma_{ci}}/_{\sigma_{ti}}$$

Equation 4.6 m_i based on UCS and different tensile tests (Colak and Unlu, 2004).

Considering m_i to be sensitive to orientation Colak and Unlu (2004) quote Hoek and Brown's (1997) recommendation that samples be tested normal to anisotropy (β = 90°)

in determining m_i. This follows the same approach as determining R_c for UCS values at β angles between 0° and 90° (section 3.2), allowing the criterion to be rewritten as Equation 4.7, for intact isotropic rock (Colak and Unlu 2004).

$$\sigma_{1(\beta)} = \sigma_3 + \left(m_{i(\beta)}\sigma_{ci(\beta)}\sigma_3 + \sigma^2_{ci(\beta)}\right)^{0.5}$$

Equation 4.7 Modified Hoek-Brown criterion for intact transversely isotropic rocks.

As m_b depends on m_i it is reasonable to assume that $m_{b(\beta)}$ depends upon $m_{i(\beta)}$, transverse strength anisotropy can be captured by the Generalised Hoek-Brown criterion (Colak and Unlu, 2004). This approach differs from that taken by Saroglou and Tsiambaos (2008), who consider that m_i is associated with rock type and not related to anisotropy. Saroglou and Tsiambaos (2008) modify the criterion with the addition of a parameter k_β to represent the effect of strength anisotropy for intact transversely isotropic materials. Their approach is consistent with the methods of determining an anisotropy ratio R_c (Equation 3.1) and their modified criterion is shown as Equation 4.8.

$$\sigma_1 = \sigma_{c\beta}\left(k_\beta m_i \frac{\sigma_3}{\sigma_{c\beta}} + 1\right)^{0.5}$$

Equation 4.8 Criterion for transversely isotropic rock (Saroglou and Tsiambaos, 2008).

4.5 Disturbance factor *D*

A disturbance factor *D* is included in the Generalised Hoek-Brown criterion to reflect the detrimental effect of stress relief from excavation or disturbance, such as from poorly controlled blasting. A value of $D = 0$ is appropriate for no disturbance of the rock mass with a maximum value of 1 ascribed to material highly disturbed by poor blasting control, stress relief from excavation itself and for all slopes. Guidance on the adoption of an appropriate value of *D* is given in Hoek et al. (2002), Hoek and Diederichs (2006) and Hoek and Brown (2018). The failure envelope calculated is very sensitive to *D*, which

varies with every application (Bertuzzi, et al., 2016). Although σ_3 is a component of the criterion there is further accounting for stress relief, by way of the disturbance factor, potentially providing a tool of convenience for the back analysis of failures but being of limited use for predictive purposes. The effect of variation in the value of *D* on *S* for different GSI values is shown as Figure 4-3.

Hoek and Diederichs (2006) showed that variation in *D* is proportional to strain level and back analysis indicated differing *D* values as concentric zones around an excavation. However, there is too much uncertainty about likely value of *D* and extent of the disturbed volume around an excavation to allow this to be used for predictive purposes (Hoek and Diederichs, 2006). Hoek and Brown (2018) note high values of *D* can occur even with careful excavation.

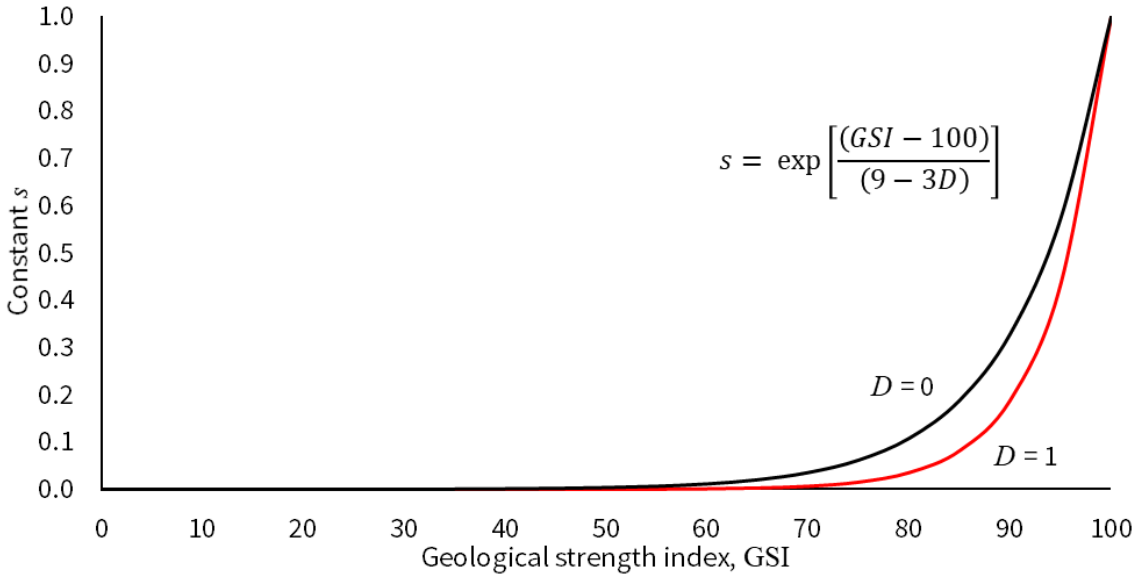

Figure 4-3 Variation in s for different values of GSI and disturbance factor.

4.6 Applicability of Hoek-Brown behaviour

Hoek and Brown (2018) suggest that their criterion is not appropriate where $\sigma_1 \geq 3.4\sigma_3$ due to the onset of ductile behaviour and suggest caution using the criterion where relatively massive rock is confined by significant in-situ stresses. To mitigate this, they suggest that care should be taken for GSI values >65. It is worth noting that this recommendation reflects high stresses in deep mining applications compared to relatively shallow civil engineering applications.

The assumption of homogeneity within the rock mass is fundamental to the criterion but is not valid where joints are spaced close to the dimensions of the excavation under consideration, such as the diameter of a tunnel or the height of an excavation bench. In such cases behaviour will be controlled by the kinematic freedom of individual joint bounded blocks or combinations of joints.

By comparison large volumes of rock may be associated with Hoek-Brown behaviour simply by virtue of number of blocks and block size relative to the size of the excavation allowing the rock mass to behave as homogeneous isotropic mass (Figure *4-4*). With respect to determining isotropy and homogeneity Palmstrom (2005) provides methods based on RQD to determine block volume and volumetric block count which can be determined in different orientations.

Connor-Langford and Diederichs (2015) provide a detailed discussion on the uncertainty associated with the parameters required for the Generalised Hoek-Brown criterion and the extent to which they are interrelated. They also state that the criterion tends to be used in a deterministic fashion whereby single values are ascribed to each parameter thereby

missing the opportunity to utilise a probabilistic approach in support of reliability-based design, described in detail by Hoek (2006).

According to Barton (2015) the complexity of the Hoek-Brown approach does not accurately represent non-linear behaviour and Singh and Barton (2019) consider that the criterion underestimates the strength of intact rock.

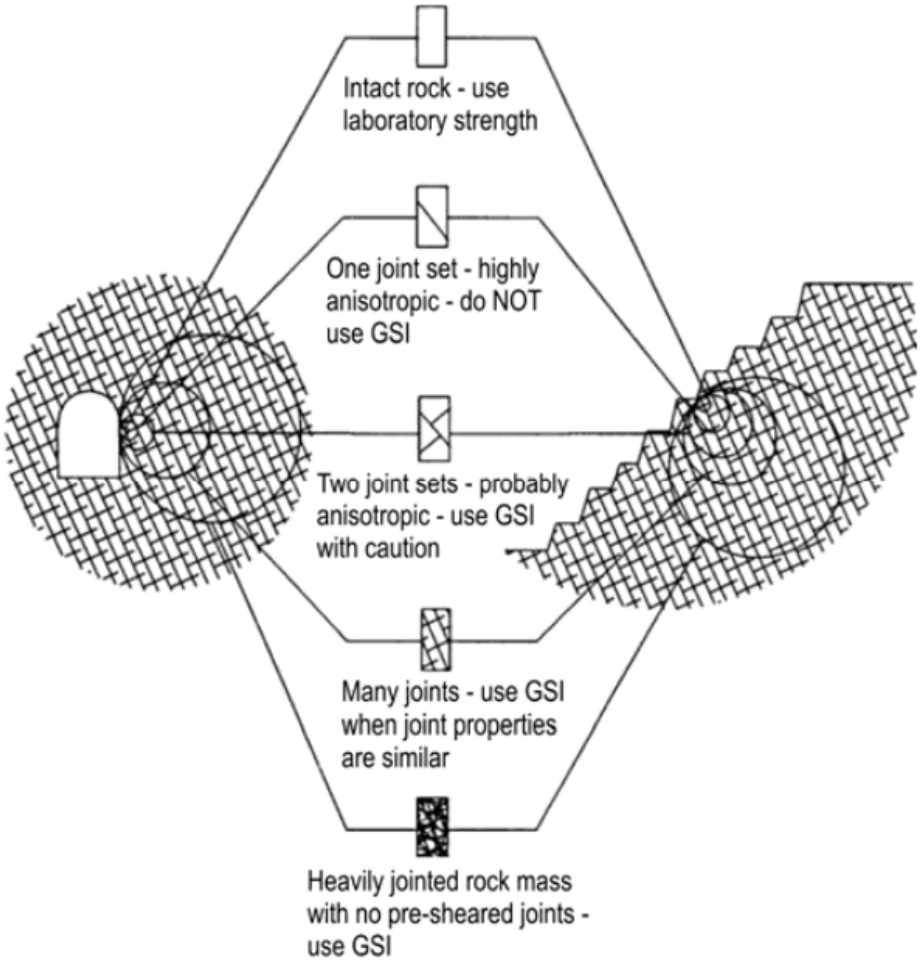

Figure 4-4 *Sample volume and behaviour from Hoek et al. (2013).*

4.7 Hoek-Brown behaviour in a triaxial stress regime

The Generalised Hoek-Brown criterion ignores the intermediate principal stress (σ_2), which Eberhardt (2012) points out is correct where $\sigma_2 = \sigma_1$ or σ_3 or the condition where

$\sigma_1 = \sigma_2 = \sigma_3$ and points to the work of others suggesting that σ_2 may also control mass strength. The notable influence of σ_2 on borehole stability Eberhardt (2012) gives as the reason why the criterion has not been widely adopted in the hydrocarbon industry. While this may be correct, the criterion was developed for larger openings where simplification to plane strain of axisymmetric conditions is often appropriate.

Modification of the criterion to take account of σ_2 for a triaxial stress regime have been developed by Priest (2005) and Zhang et al. (2013). Priest (2005) combined the Hoek-Brown criterion with the three-dimensional Drucker-Page failure criterion and used a weighting average of σ_2 and σ_3 to take account of σ_2. This approach was validated by Melkoumian et al. (2009) in examining well bore stability. In comparing various three dimensional failure criteria Priest (2010) concludes that three-dimensional versions of the Hoek-Brown criterion needs to be validated against the observed behaviour of rock masses at high stress levels accompanied by triaxial test data. Zhang et al. (2013) provide a smooth theoretical criterion for the transition between compressive and extensional behaviour but do not provide the comparison with observed behaviour sought by Priest (2010). The method proposed by Zhang et al. (2013) calculates the same strength for both two and three-dimensional stress states, as well as for both triaxial states of compression and tension, which Priest's (2005) method does not.

4.8 Tensile behaviour

Tension failure is not dealt with specifically in the Generalised Hoek-Brown criterion, but Hoek and Brown (2018) highlight the need for inclusion of a tension cut off to reflect negative values of σ_3, such as from stress redistribution around an excavation. As a provisional measure Hoek and Brown (2018) suggest a tension cut off as a ratio of tensile strength (σ_t) based on m_i and σ_{ci} (Equation 4.9).

$$\sigma_{ci}/\sigma_t = 0.81\, m_i + 7$$

Equation 4.9 Tension cut off suggested by Hoek and Brown (2018).

This recommendation is based on high quality laboratory testing and observed behaviour of a range of rock types (Figure 4-5). Any tensile strength should only be used for high GSI values to ensure there remains sufficient intact rock within the rock mass to rely on tensile strength (Rocscience, 2016). The parameter m_i is derived from compression related strength testing, which Connor-Langford and Diederichs (2015) believe also to be applicable to tensile failure, suggesting that this fundamental behaviour is captured by the test method itself. This supports the view of Cai (2010).

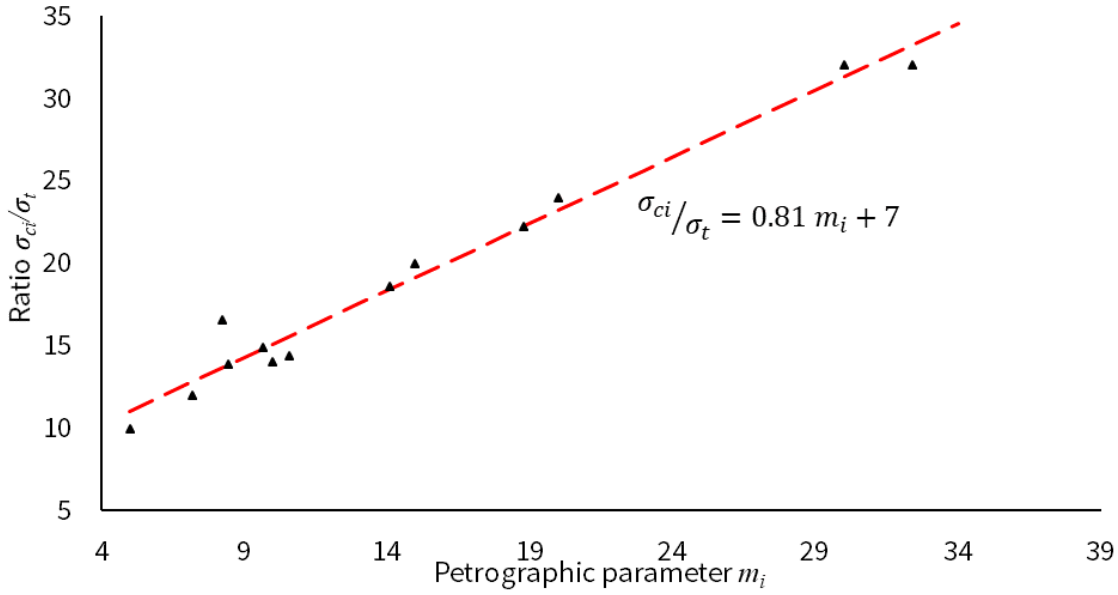

Figure 4-5 Data used to support Equation 4.9 from Hoek and Brown (2018).

4.9 Derivation of Mohr-Coulomb parameters from Hoek-Brown behaviour

As with soils in the drained conditions rock masses fail in response to changes in effective stress. Hudson (1989) points to the potentially erroneous assumption about hydraulic connectivity through a rock mass when calculating pore pressure, (u) and overburden

stress. Irrespective of the condition before excavation the very action of tunnelling in rock tends to drain the rock mass (Hoek and Marinos, 2000; Hoek, 2006) such that effective stress and the associated friction derived strength increases.

The Generalised Hoek-Brown criterion is expressed in terms of σ_1 and σ_3 and was developed at a time when the analytical software and hardware required to model complex constitutive models was not commercially available. For engineering design and analysis purposes, it is more common to define failure in terms of φ and c based on shear and normal stress. This limitation was recognised by the original authors (Hoek, et al., 2002), who are amongst the authors who have developed methods for deriving Mohr-Coulomb parameters from the criterion (Hoek, 1990; Hoek, et al., 2002; Lee and Pietruszczak, 2017). Methods available to derive Mohr-Coulomb parameters allow a secant or tangent (instantaneous) value of φ and c to be determined for a given stress level (see section 3.4).

The method provided by Hoek et al. (2002) uses a calculated value of rock mass strength, σ'_{cm} (Equation 4.10) to calculate σ'_{3max} (Equation 4.11), the maximum confining stress at which the calculation of Mohr-Coulomb parameters from the Generalised Hoek-Brown criterion is valid. With reference to Equation 4.11 the term γH accounts for overburden stress and should be replaced by the horizontal stress, if greater. This method is applicable to tunnels, but not slopes (Hoek, et al., 2002).

$$\sigma'_{cm} = \sigma_{ci} \frac{\left(m_b + 4s - a(m_b - 8s)\right)\left({m_b}/{4} + s\right)^{a-1}}{2(1+a)(2+a)}$$

Equation 4.10

Calculation of σ'_{cm}.

$$\sigma'_{3max} = \sigma'_{cm}\left(0.47\left(\frac{\sigma'_{cm}}{\gamma H}\right)^{-0.94}\right)$$

Equation 4.11

Calculation of σ'_{3max}.

$$\varphi' = sin^{-1}\left(\frac{6am_b(s + m_b\sigma'_{3n})^{a-1}}{2((1+a)(2+a) + 6am_b(s + m_b\sigma'_{3n})^{a-1}}\right)$$

Equation 4.12

Calculation of φ'.

$$c' = \frac{\sigma_{ci}\lfloor(1+2a)s + (1-a)m_b\sigma'_{3n}\rfloor(s + m_b\sigma'_{3n})^{a-1}}{(1+a)(2+a)\sqrt{1 + \frac{(6am_b(s + m_b\sigma'_{3n})^{a-1})}{((1+a)(2+a))}}}$$

Equation 4.13

Calculation of c'.

$$\sigma_{3n} = {\sigma'_{3max}}\Big/{\sigma'_{ci}}$$

Equation 4.14

Determination of σ_{3n}.

Lee and Pietruszczak (2017) undertook numerical simulations to address the need for an explicit relationship between the Generalised Hoek-Brown criterion and shear and normal stress at failure for GSI values <100, where $a \neq 0.5$. They present a solution for all possible values of *a* based-on approximations of the relationship between σ_n and *sine* φ_i.

5 The Geological Strength Index

5.1 Purpose

GSI was introduced to the Hoek-Brown criterion in the 1990s as a qualitative method to capture aspects of rock lithology, structure and the condition of joints observable from boreholes, outcrops or the face of a tunnel or excavation. The index, from 0 to 100, was introduced to replace a modified version of RMR originally used as a method for downgrading intact rock strength (Bertuzzi et al., 2016). The original use of RMR did not adequately characterise aspects of the geological conditions relevant to behaviour, particularly in weak, fractured, or disturbed rock masses (Marinos et al., 2007) and unlike other methods of classification, the index was not intended to estimate support measures, reinforcing requirements or stand-up time (Hoek and Brown, 2018). The value of GSI used in the failure criterion must be representative of the volume of rock associated with stress redistribution around the excavation and not just the excavated material (Marinos et al., 2007).

5.2 Geological Strength Index charts

GSI values can be obtained easily from charts of two readily observable rock mass parameters: joint surface quality and the extent of block interlock (Figure 5-1). Neither of these parameters are available from in-situ or laboratory tests but both are fundamental to mass behaviour.

Characteristics such as joint tightness, cleanliness, spacing of fractures and good block interlock cannot easily be measured by laboratory or in-situ testing but have considerable contribution to mass strength. GSI has no reference to rock strength as this is dealt with

in the failure criterion itself (Hoek and Brown, 2018), and originally had no reference to scale.

GSI can describe everything from disintegrated to intact rock masses (Marinos and Hoek, 2000; Hoek et al. 2002 and Hoek and Brown 2018). Updates to the original GSI chart include additional charts applicable to tectonically disturbed rock masses including: molasse, flysch, heterogeneous or lithologically variable masses, sheared weak masses and ophiolites (Marinos et al., 2007; Marinos and Carter, 2018). More recently the existing GSI charts have been supplemented by the work of Vassilis and Carter (2018) who have reinvigorated the geological emphasis of the GSI system with the introduction of charts to tackle weathered and other rock masses that are hard to describe in an engineering context.

5.3 Limitations and advantages of GSI

Marinos et al. (2007) cautions the use of the GSI in tectonically disturbed rocks if mass behaviour will not be governed by sliding or rotation of blocks of rock and suggests that the Generalised Hoek-Brown criterion may only be applicable for a GSI between 35 and 75. Bertuzzi et al. (2016) suggests that the lower limit may be a GSI = 30 and σ_c = 15 MPa. The absence of consideration of the aperture of joints in the index is subsequently addressed by using an appropriate disturbance factor (*D*) (Marinos et al., 2005; 2007).

GSI and the Generalised Hoek-Brown criterion are based on the assumption that the rock mass behaves as a mechanical continuum and geological observations captured are fundamental to rock mass behaviour, i.e. there are sufficient joints of different orientation to allow behaviour as homogeneous isotropic mass. Such an assumption is not

necessarily valid in predominantly young rocks without enough joints to allow behaviour significantly different from the intact strength (Marinos et al., 2007).

5.4 GSI and RQD

Hoek (1999) and Hoek et al. (2013) describe oposing views on recording geological conditions qualitatively or quantitively, suggesting geologists prefer the former and engineers the latter. To satisfy the desire for a quantiative method to determine GSI, Hoek et al. (2013) introduces a method by which numbers can be ascribed to the axes of the GSI chart based on RQD and joint condition. The method of assessing joint condition chosen is based on that originally defined in Bieniawski's 1989 RMR system (JC_{89}). The relationship between the numerical scales applied to RQD and JC_{89} (Equation 5.1) were found by Hoek et al. (2013) to give good agreement with qualitative determination of GSI. The use of RQD introduces scale into the GSI, where it was previously absent (Bertuzzi, 2019), as well as the limitations associated with RQD itself, discussed in section 3.5.

$$GSI = 1.5JC_{89} + {}^{RQD}/_{2}$$

Equation 5.1 GSI based on RQD and JC_{89} from Hoek et al. (2013).

Figure 5-2 shows the quantitative GSI chart, comparison with Figure 5-1 reveals that lines bounding GSI values are parallel, allowing a simpler numerical characterisation of GSI. Hoek et al. (2013) suggest that this change is sufficiently small to remove the need for existing analyses to be revised.

The simple description of joints in terms of JC_{89} contrasts with the UK's standard method of describing discontinuities in rock in the relevant part of Eurocode 7: BS EN ISO 14689 (BSI, 2018). The surface condition description on the GSI chart covers the more

complicated descriptions of discontinuity surfaces given in BS EN ISO 14689, which requires separate descriptive terms for surface form, weathering, and roughness. This prevents comparison on a simple two-axis chart, which Pine and Harrison (2003) point out as being an advantage of the GSI.

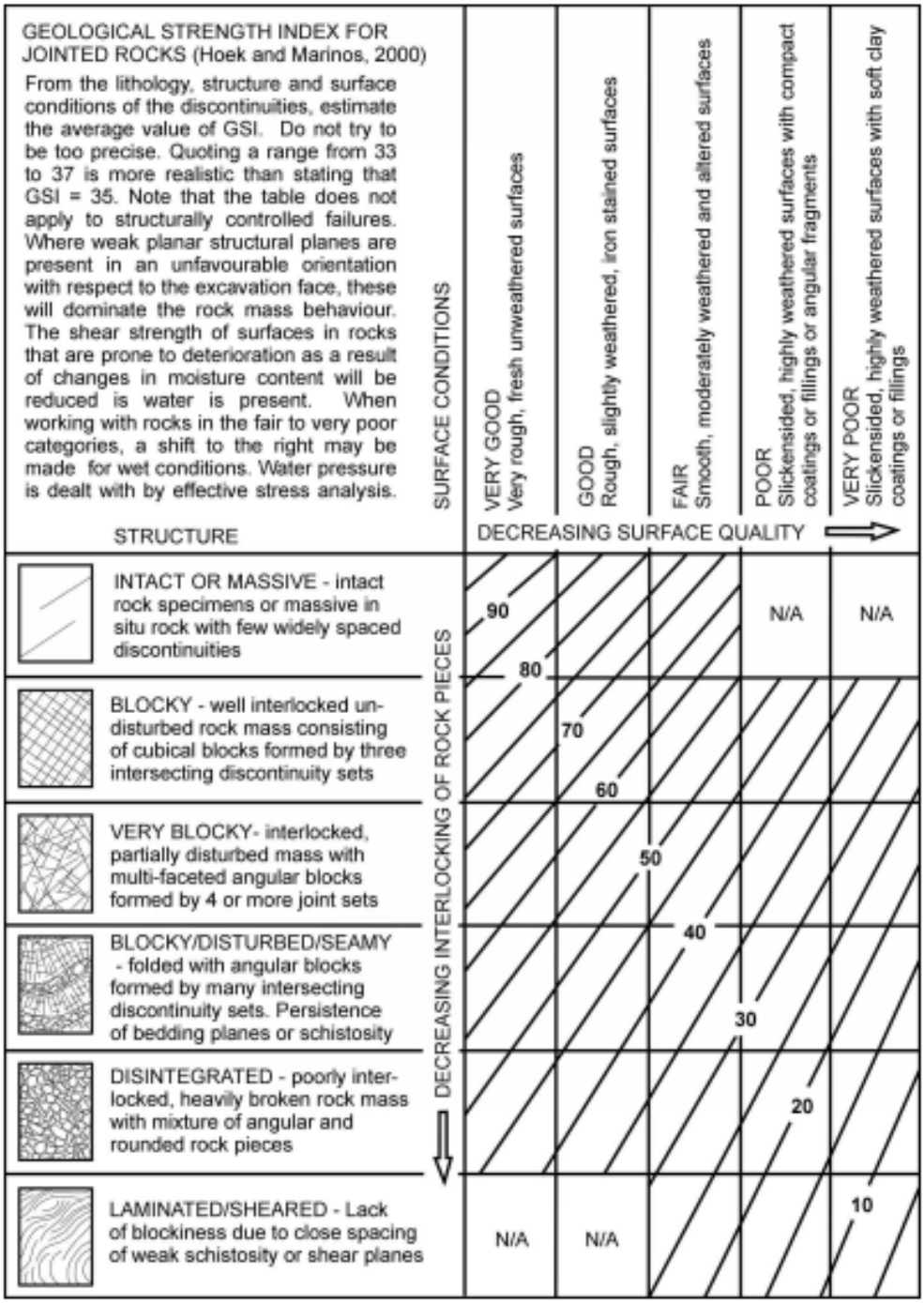

Figure 5-1 Geological Strength Index chart from Hoek and Marinos (2000).

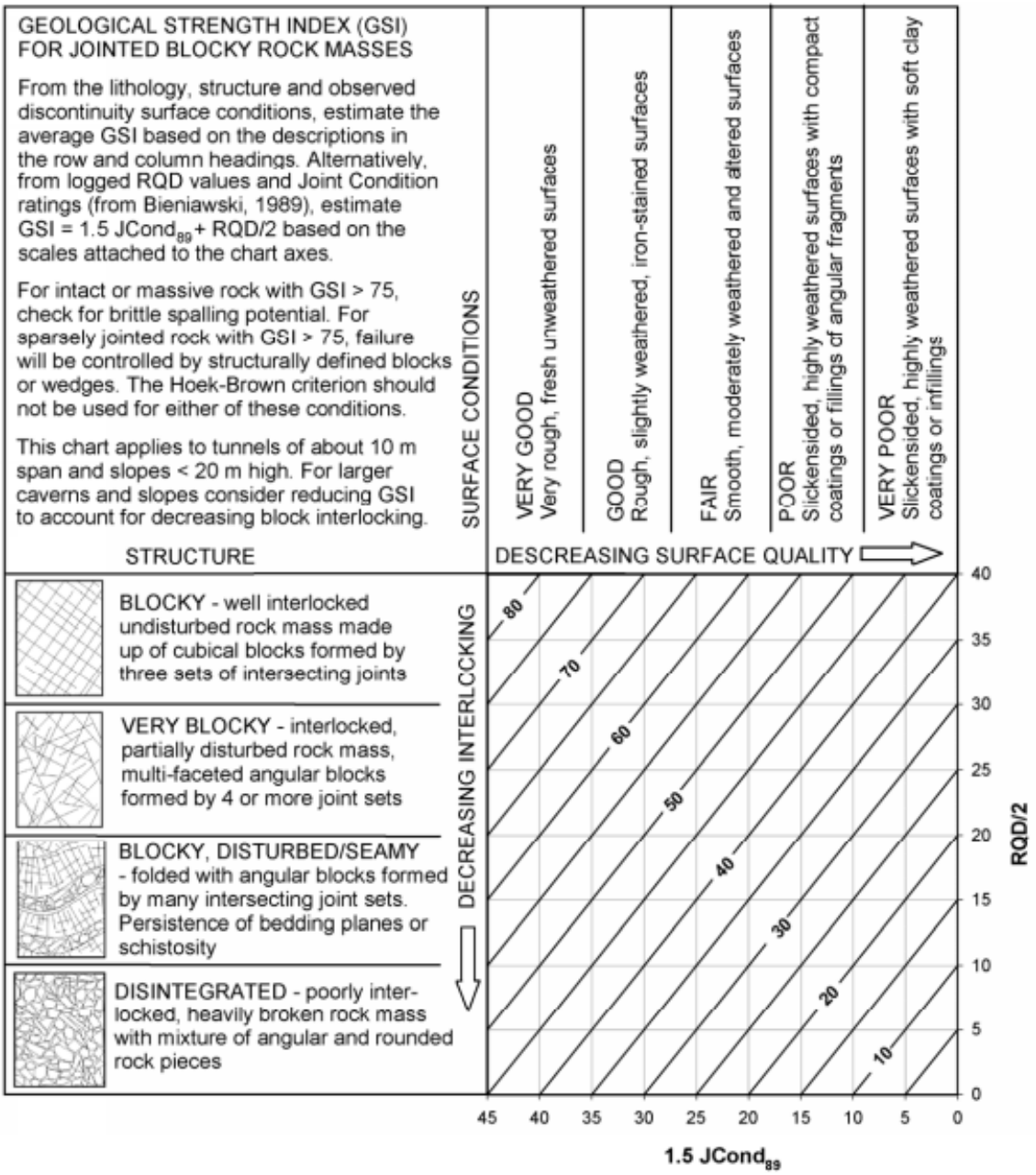

Figure 5-2 Revised GSI chart for quantitative purposes from Hoek et al. (2013).

5.5 Anisotropy and the Geological Strength Index

At the scale of most engineering applications materials may be treated as homogeneous and isotropic, but judgement is needed with respect to block size. Schistose gneisses, schists, phyllites and slates require particular consideration of the appropriateness of GSI

because of their anisotropic nature (Marinos and Carter, 2018). Marinos et al. (2005) recommend that undisturbed slate should not be assigned a GSI value where failure is governed by anisotropy. Where block size does not exceed 10% of the relevant excavation dimension then GSI may be applied and Hoek-Brown behaviour can be expected (Marinos and Carter, 2018).

For pronounced anisotropy an orientation dependant GSI value could be adopted, however this results in considerable complexity in any associated analysis. It is preferable, and mathematically simpler, to incorporate an orientation dependant strength into the Hoek-Brown criterion for analysis purposes (Marinos et al., 2007). This fits well with anisotropic strength variation given in Equation 3.1 and its incorporation into either criterion shown as Equation 4.7 or Equation 4.8. With respect to all input parameters in the criterion, Hoek (1998) recommends using a normal distribution, apart from for GSI >40. Marinos et al. (2005) recommend the use of a range of GSI values to reflect the breadth observed, thereby encouraging the use of a probabilistic approach.

6 Slope instability explored through Hoek-Brown behaviour

6.1 Talysarn Quarry failure

This section summarises a parametric study of Hoek-Brown parameters to identify combinations of parameters with the potential to cause quarry scale slope failure in the Llanberis Slates Formation. This was undertaken after observation of a large rock slope failure in 2020.

On 16th July 2020 a significant failure of part of the subvertical rock face of Talysarn Quarry occurred, a quarry immediately adjacent to Dorothea (Figure 6-1). The failure was captured on a 16" video clip (pers. comm. M. Billingham, 2020), annotated stills from which are shown as Figure 6-3 to Figure 6-9. The failure appears to have involved a significant volume of material previously forming the south facing subvertical wall of the quarry. Failure was reportedly preceded by smaller minor collapses and spalling from April 2020.

The backscarp of the failure appears curved and can only be observed from a distance on either the opposite side of the quarry or from above (Figure 6-2). The curved and stepped dislocation surface is inconsistent with failure along the planar joints generally observed to be present, suggesting failure, in-part, through intact material. The failure appears to have removed between 5 and 8 m horizontally from the previous face of the quarry wall. With reference to the following Figures, water level is at approximately 97.3 mOD and the rim of the spoil around the rim of the quarry is at a level of about 132.5 mOD. The depth of the water is unknown. A conservative estimate of the volume of material involved is 1,800 m^3.

*Figure 6-1 Location of the Talysarn failure * (Google Earth).*

Figure 6-2 View of the backscarp of the failure (courtesy of Nigel Spires).

A. Existing scarp of slate waste above subvertical rockface

B. Massive coherent block rotating forward

C. Disintegrated base of failure below coherent mass above

D. Debris falling into the still water of the quarry ahead of main body of the failed mass

E. Adit exposed in quarry wall

Figure 6-3 Image from the first second of the video clip.

A. Coherent failed mass continuing to rotate forwards

B. Continued disintegration of the toe of the failure, which appears to have started entirely above the water line

C. Area of debris fall into lake increases

Figure 6-4 Image from the next second of the video clip.

A. Fast moving main body of fall starts to penetrate the water and develop a significant splash

Figure 6-5 Image from the third second of the video clip.

A. Development of curtain of high speed water

B. Ravelling of slate waste and soil bought down with the main body of the fall

C. Brown sediment laden water flung outward

Figure 6-6 Image from the fourth second of the video clip.

A. Video shows falling rock debris flung upwards and outwards by force of water curtain before lakefall

Figure 6-7 Image from the fifth second of the video clip.

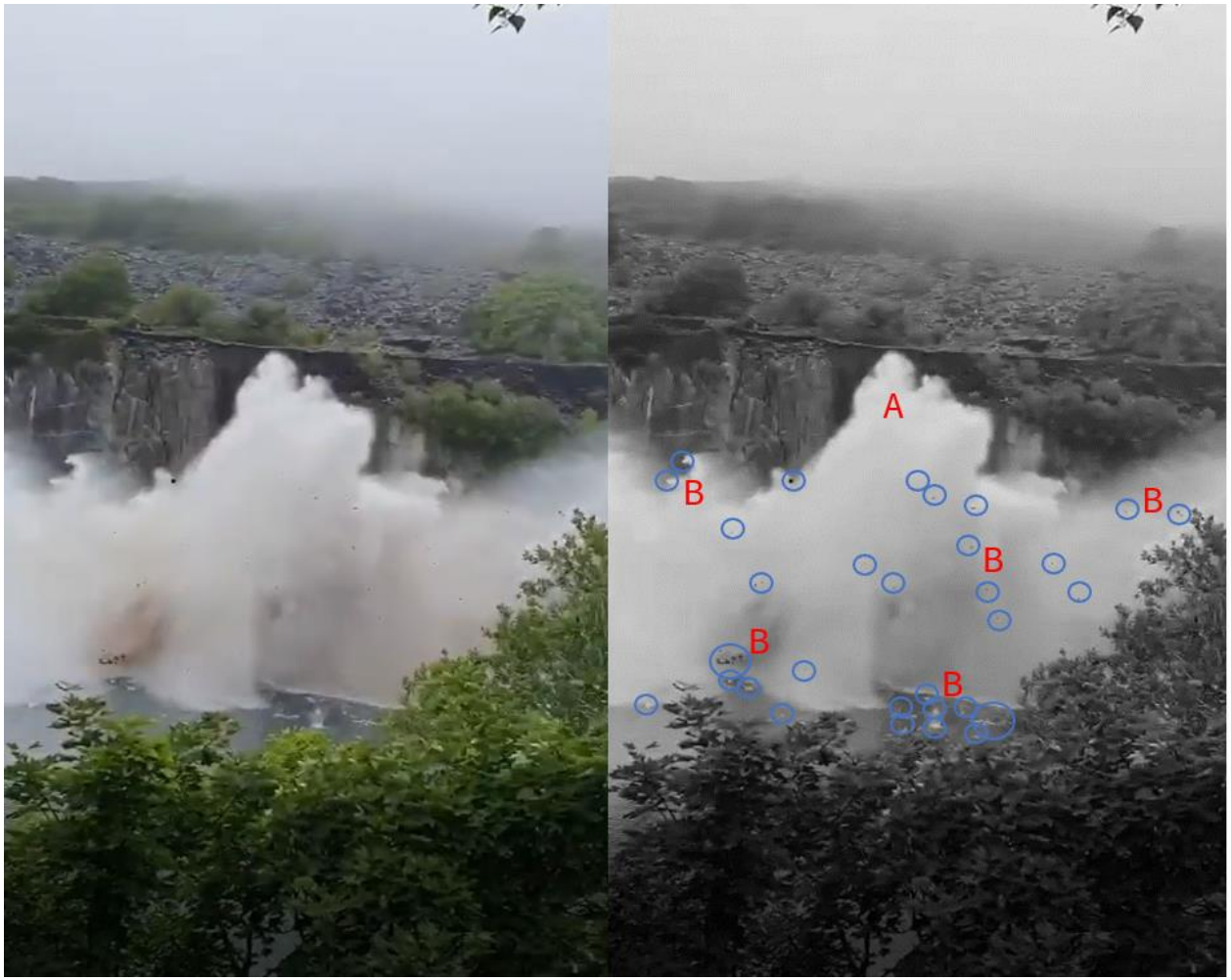

A. Height of splash reaches the original fall height

B. Ejecta

Figure 6-8 Image from the sixth second of the video clip.

A. Although appearing dry, slate waste and soil pour down the newly exposed rockface

B. No sign of water flowing or damp patches on the rockface

C. Waves propagate outwards as curtain of water disperses

Figure 6-9 Image from the tenth second of the video clip.

The scale of the failure was considered too great to be attributable to root wedging and the absence of concurrent seismic activity (BGS, 2020) allowed both of these to be discounted as a cause. Similarly, the absence of recent surcharging of the slope or changes in water level did not present an obvious trigger mechanism. Notwithstanding these points the collapse provided an opportunity to model the failure along with the ascribed Hoek-Brown strength criteria.

6.2 Overview of FLAC analyses

Appendix D provides details of numerical simulations used to identify combinations of Hoek-Brown parameters resulting in calculated failure of the rock mass. Theoretical failure was identified by a factor of safety of approximately unity. In the absence of bathymetric information from Talysarn Quarry topographic and bathymetric data for a cross section through the sidewall of Dorothea was used in the analyses. The cross section chosen has the greatest total height of all the quarries and is, in places, subvertical and is therefore considered the most sensitive to changes in strength parameters.

Results of the analyses using Itasca's finite difference FLAC programme are tabulated in Appendix D.4 along with parameters used in each simulation. Results are also shown summarised as Figure 6-10 and Figure 6-11. Table 6.1 summarises combinations of m_i, σ_{ci} and GSI used in the analyses that resulted in failure.

Analyses for GSI = 100 are associated with no reduction in parameter m_b, i.e. intact behaviour, whereby the calculated factor of safety only varies as a function of a change in intact strength. For GSI = 100 failure occurs at σ_{ci} <1 MPa. To prevent failure for GSI = 90 or 85 a minimum σ_{ci} = 1 MPa or 1.5 MPa is required respectively. Further reduction to GSI = 80 suggests failure for σ_{ci} = 2 MPa. At progressively lower values of GSI greater

values of σ_{ci} are required to prevent failure and the difference in m_i become more apparent by requiring grater intact strengths still.

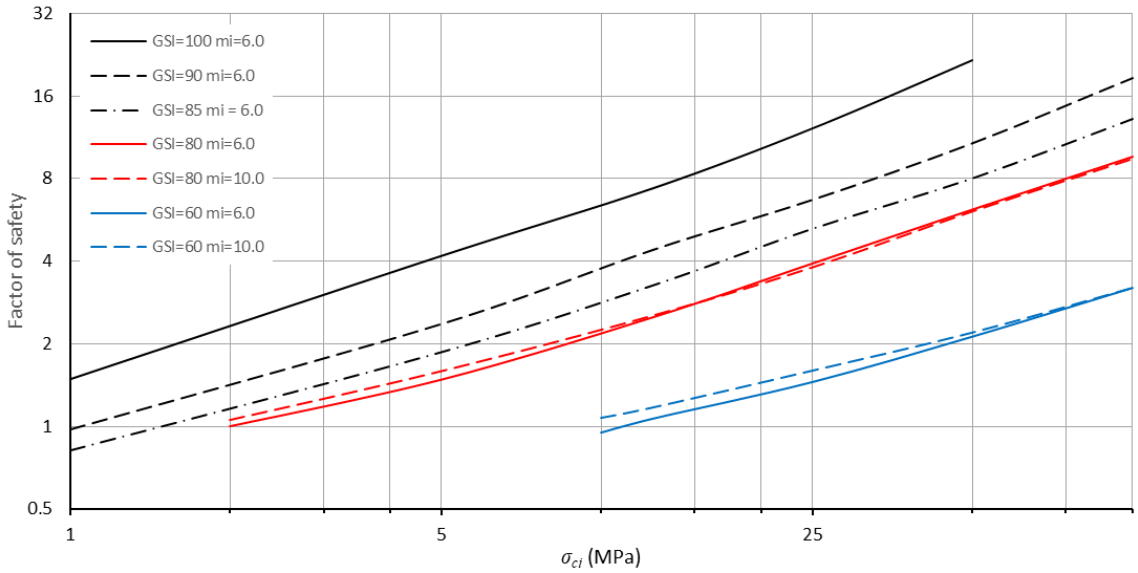

Figure 6-10 Log-log summary of FLAC results.

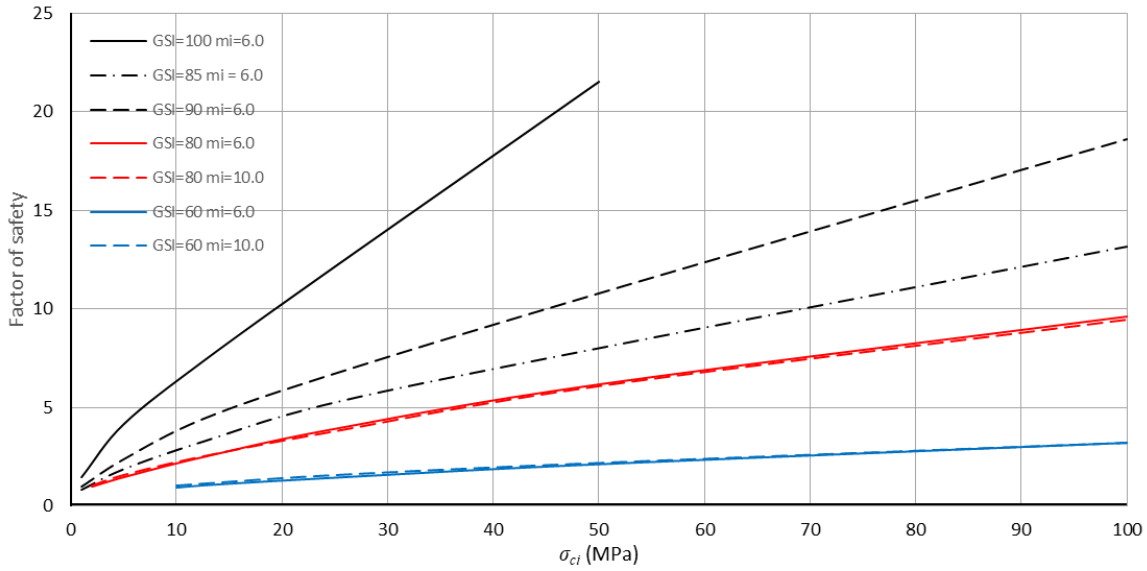

Figure 6-11 Summary of FLAC results.

σ_{ci}	<1 MPa	1 MPa	1.5 MPa	<2 MPa	2 MPa	<9 MPa	12.5 MPa
GSI	100	90	85	80	80	60	60
m_i	6.0	6.0	6.0	6.0	10.0	10.0	6.0

Table 6.1 Summary of combinations of parameters causing failure.

Figure 6-12 shows an example of the simulated failure of the slope (Table D.2 file 601.txt), which suggests that a greater distance from the quarry is involved in the calculated failure than that observed. Of note in Figure 6-12 is a pronounced zone of higher shear strains rather than a discrete failure surface through a brittle material. This may capture some of the mechanisms of the failure surface jumping through intact material between joint surfaces, where present.

To explore the possible role of tensile strength file 601.txt (factor of safety 0.95) was rerun with σ_t set to zero (611.txt) and returned the same factor of safety, to six decimal places (0.951172). The numerical simulation may be correct but this is not considered to replicate the reality of a high, steep rock face relaxing towards the quarry excavation.

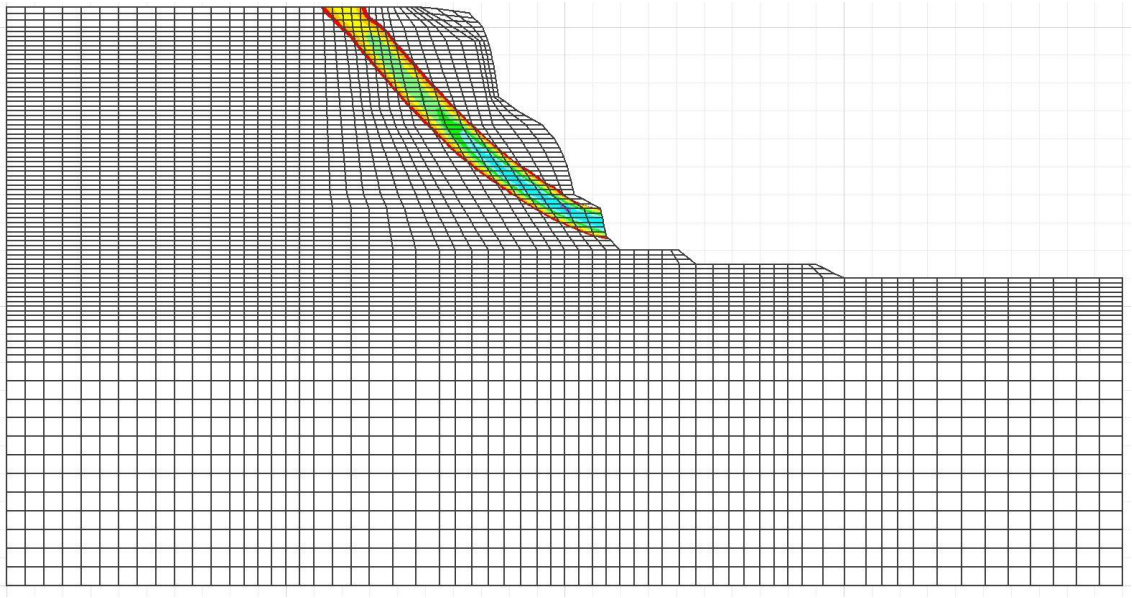

Figure 6-12 Example failure predicted from FLAC analysis.

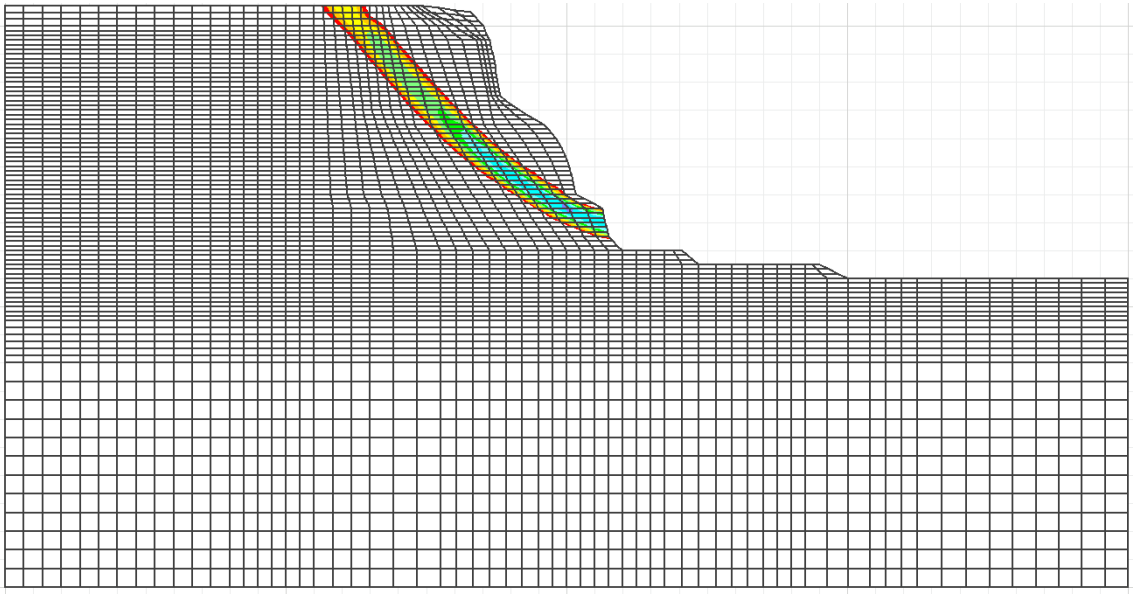

Figure 6-13 Example failure from Figure 6-12 re-run with zero tensile strength.

Despite numerous simulations for a wide range of parameters Figure 6-10 and Figure 6-11 show that the predicted failure involves a greater volume of material than observed from the Talysarn failure. This suggests that the analyses and Generalised Hoek-Brown model do not easily align with the very steep backscarp of the observed Talysarn failure.

6.3 Verification by complementary analyses

To compare FLAC results further analyses were undertaken using combinations of parameters for which FLAC calculated a factor of safety of <1.5. This verification process is described in Appendix E and used Rocscience's Slide 6 software to calculate a factor of safety for a 2D slice using Bishop's simplified method. The results of the analyses align well with the FLAC results (Table E.1), providing mutual corroboration of the general geometry of the predicted failure surface and the relative magnitude of restoring and disturbing forces, despite the Slide analyses being limited to circular failure surfaces.

The verification process reinforces the initial assertion that observed behaviour cannot be explained by Hoek-Brown behaviour alone. The circular failure surfaces identified from the FLAC analyses and supported by the Slide analyses would not typically be appropriate for a homogeneous isotropic material. It is debatable if this reflects reality but may be considered as a simplification of mobilised strengths. It is worth noting that values of GSI (Appendix D.3.2) and compressive strengths required to cause failure (Appendix D.3.1) are considerably lower than those reported by Davies (2020) or given in Table 3.3. Figure 6-14 shows a slide output providing a similar factor of safety to the corresponding FLAC analysis using the same parameters and slope geometry.

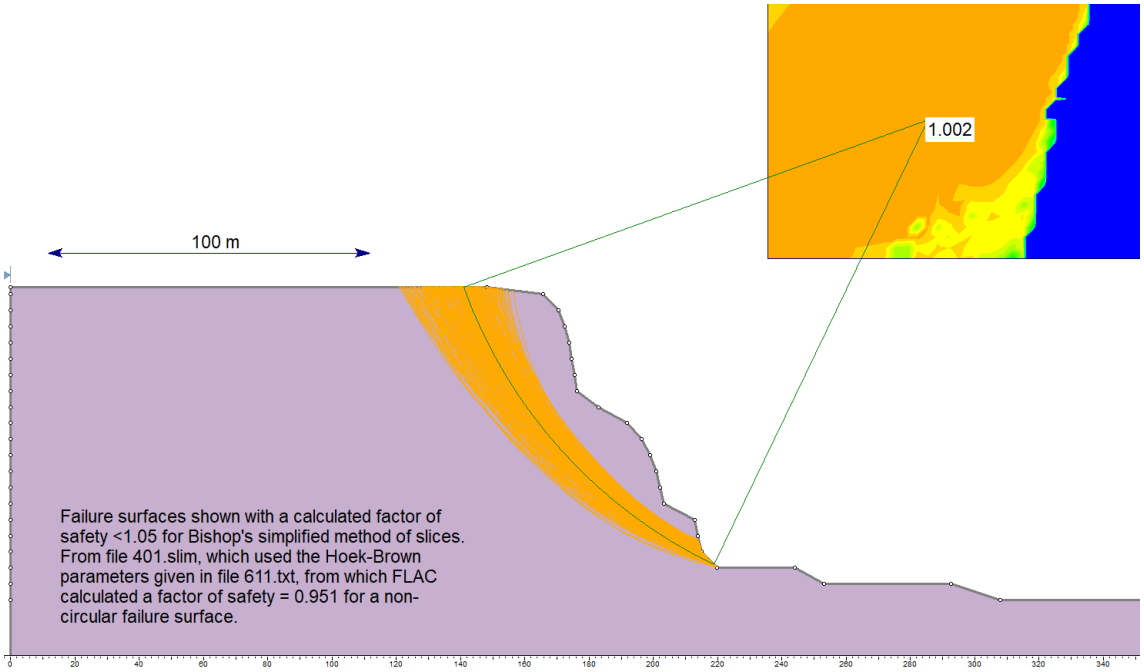

Figure 6-14 Slide output suggesting failure in a similar fashion to Figure 6-12.

6.4 Summary

The FLAC analyses undertaken are complex and attempts to replicate changes in in-situ stress with quarry excavation did not yield results that are sensitive to σ_t or replicate the very steep Talysarn style failure. Progressively downgrading Hoek-Brown parameters until failure was predicted allowed failure-critical combinations to be determined (Table 6.1). The combination of Hoek-Brown parameters required to cause theoretical failure do not fit with field observations of strength or GSI based on RQD (Figure D-26).

The numerical simulations undertaken should therefore be treated with caution as they represent the calculated factor of safety for a very specific form of failure, and apparently not the mode of failure associated with the lowest overall factor of safety and greatest propensity for failure.

7 The Barton failure criterion

7.1 Background and input parameters

This section describes an alternative failure criterion for jointed rock masses; the Barton criterion. The Barton failure criterion is an evolution of the Q-system (section 3.5) that has been linked to different tunnelling methods. Barton (2014) summarises the non-linear strength of jointed rock masses (Equation 7.1) using a joint roughness coefficient (JRC), (Figure 7-2), joint compressive strength (JCS) and an estimate of the residual friction angle (φ_r). JCS is the mean of the highest 50% of Schmidt hammer results. φ_r is a degraded value of the bulk friction angle (φ_b), downgraded by the relationship of mean Schmidt rebound hardness on dry unweathered surfaces to wet weathered surfaces (Equation 7.2). φ_b is determined from tilt tests, or where JRC >9, forced sliding tests (Barton, 2014).

Input parameters for the criterion are uncomplicated and easy to obtain from field measurements and routine tests. The envelope is expressed in terms of shear and normal stress, always with zero cohesion at zero σ_n. Example failure envelopes are shown as Figure 7-1, showing the influence of JRC on non-linearity, with JRC = 0 giving a linear failure envelope and JRC >0 giving progressively greater non-linearity. Irrespective of the value of JRC the different envelopes shown diverge at $\sigma_n = 0$ and converge at a point where σ_n = JCS, at which point failure can propagate through intact material regardless of joint properties. For unweathered planar smooth joints, terms involving JRC and JCS are negated and Equation 7.1 reverts to $\tau = \sigma_n \cdot tan\ \varphi_r$, i.e. a linear failure envelope passing through the origin of a graph of normal and shear stress and directly comparable to Coulomb's failure surface (section 3.4). This uses a residual friction angle, which is

always less than the basic frictional properties of the rock. Subsequent development of the criterion to the Barton-Bandis behavioural model took account of scale effects observed between different sized samples subjected to direct shear or tilt tests (Prasssetyo et al., 2017).

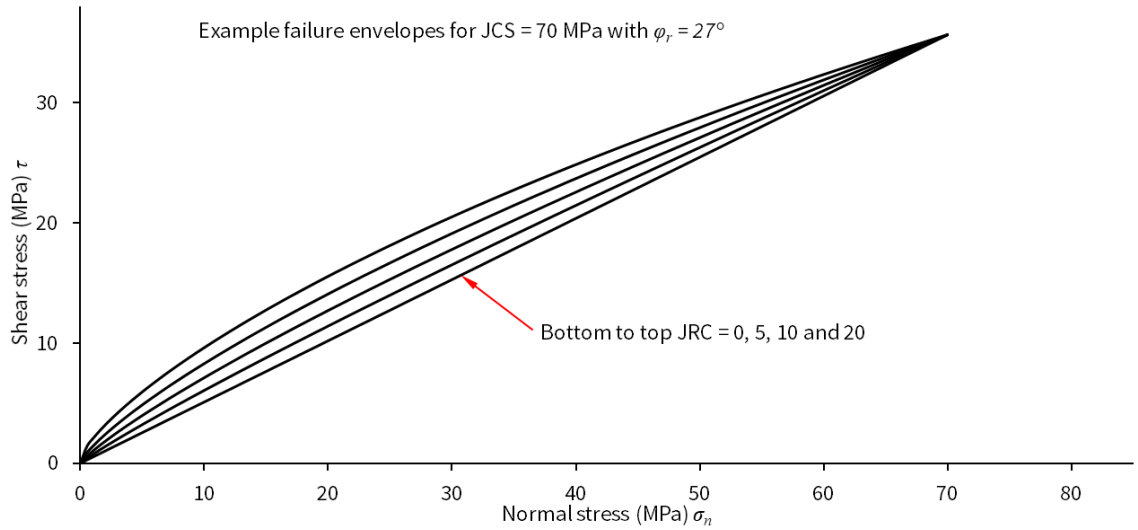

Figure 7-1 Illustrative failure envelopes for the Barton criterion.

$$\tau = \sigma_n \tan\left(JRC \log\left(\frac{JCS}{\sigma_n}\right) + \varphi_r\right)$$

Equation 7.1 Barton's criterion.

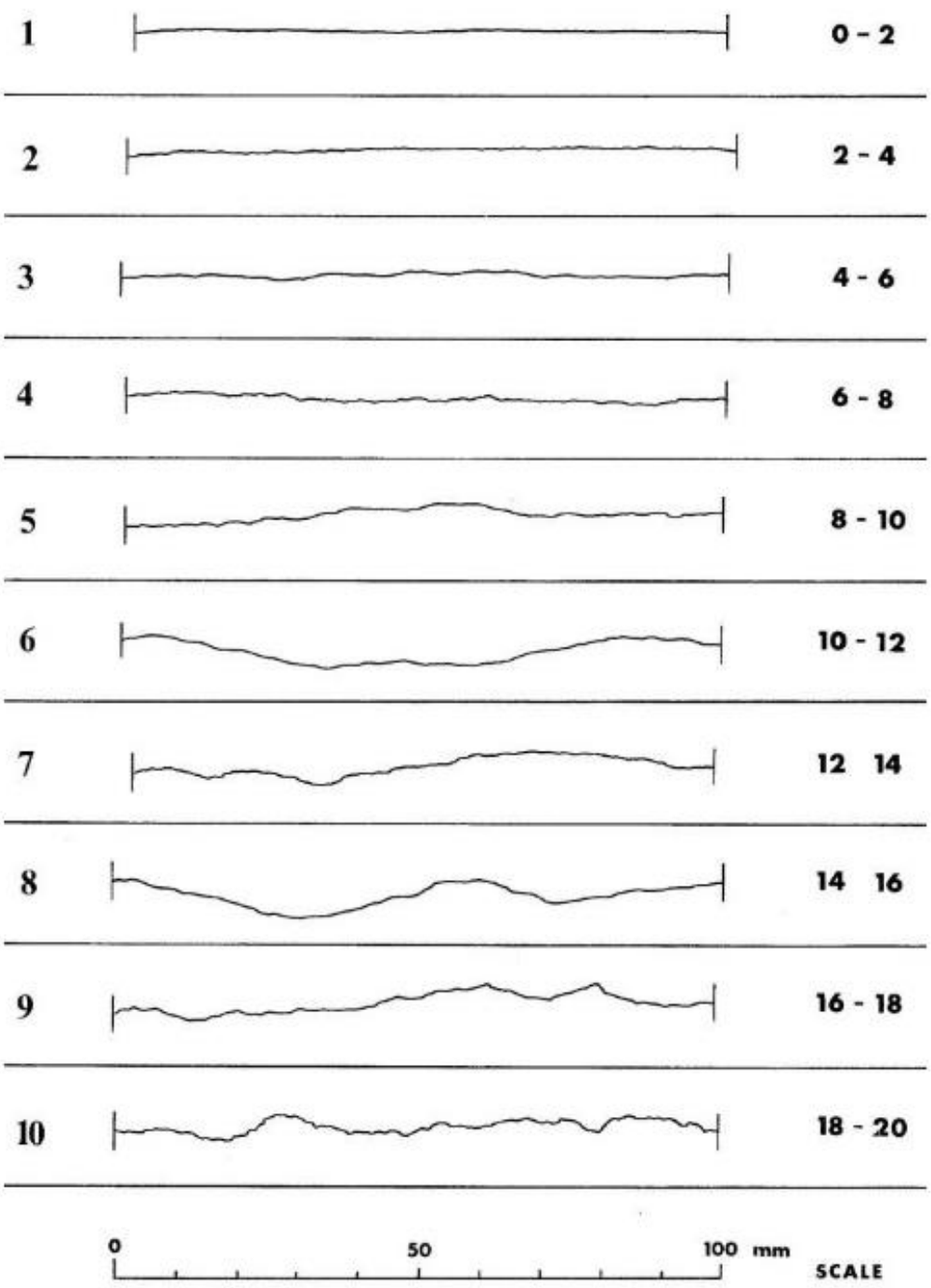

Figure 7-2 True scale chart of Joint Roughness Coefficient (Barton, 2014).

7.2 Frictional parameters φ_b and φ_r

7.2.1 Basic friction angle, φ_b

The use of φ_b in rock engineering to estimate the shear strength of discontinuities and may be determined from a simple tilt test (Jorda-Bordehore and Herrera, 2018). Alejano et al. (2012) suggest typical values of 25° to 30° for sedimentary rocks and 30° to 35° for igneous and metamorphic rocks.

There is no standard procedure for undertaking a tilt test (Alejano et al. 2012; Jorda-Bordehore and Herrera 2018; Pérez-Rey et al; 2019) and Barton originally proposed undertaking the test on a sand blasted or rough sawn surface (Pérez-Rey et al., 2019). Various types of tilt test for determining the basic frictional properties include:

- Sliding of one core axially along two basal cores (Figure C-7), originally described by Stimpson (1981).
- Sliding of an axially bisected length of core.
- Sliding discs of core over one another, i.e. shorth lengths of core cut perpendicular to the axis of a core.
- Sliding of block or slab samples.

Various recommendations are provided by Pérez-Rey et al. (2019) for each of the test types listed above, including a minimum sliding area of 50 cm^2 as well as various sample aspect ratios to ensure a uniform normal stress distribution across the sliding surface to minimising overturning moments at high tilt angles. For cores cut axially a minimum diameter of 55 mm (NX core) should be used (Pérez-Rey et al., 2019). Stimpson's (1981) three-core method has the advantage that it can be undertaken in the field from core samples without the need for further sample preparation. Alejano et al. (2012) correctly

point out that Stimpson's three-core method, where sliding occurs along two generatrices rather than across a surface, to overestimate φ_b from an error in the original maths, which they correct (Equations 7.3 and 7.4).

Influence factors on all tilt tests are described by Pérez-Rey et al. (2019) including tilting rate, rock surface preparation, vibration, and the effect of polishing from repeated testing. Tiling rate and accelerations of <0.005 g did not contribute to the onset of sliding and polishing may be minimised by limiting sliding to 5-10% of the maximum possible sliding length. Recommendations were also provided for finishing saw cut surfaces prior to testing.

7.2.2 Residual friction angle, φ_r

The relationship of φ_r to φ_b (Equation 7.2) utilises R and r, the mean Schmidt hammer rebound hardness for fresh, dry, unweathered samples and rebound hardness for weathered wet discontinuities respectively (Barton, 2014). Only the mean value of the upper 50% of Schmidt values is used to determine both r and R.

$$\varphi_r = (\varphi_b - 20°) + 20 \cdot \left(\frac{r}{R}\right)$$

Equation 7.2 Relationship of φ_r to φ_b used in the Barton criterion.

7.3 Deriving Barton's criterion for the Kelly Burn Sandstone

Appendix C documents the derivation of Barton's criterion from core samples available to the author from a Devonian sandstone from Scotland. The work documented in Appendix C was undertaken to develop fieldwork methods prior to undertaking fieldwork and provides:

- Calibration of Schmidt rebound hardness against UCS measurements.
- An assessment of the influence of hammer orientation on rebound hardness.

- Details the scatter observed in Schmidt data to determine the minimum number of tests needed to determine a coefficient of variability of <5% to ensure an acceptable minimum number of tests were undertaken.
- An explanation of the use of the profile gauge to determine JRC.
- An explanation of the Stimpson's three-core sliding test as modified by Alejano et al. (2012) on 117 mm diameter core samples to determine φ_b.
- A calculated strength envelope for the Kelly Burn Sandstone (Figure C-8), and the associated instantaneous shear strength parameters.

7.4 Comparison of methods to determine ϕ_b

7.4.1 Sliding tests on small diameter cores

This section provides a comparison of methods used to determine φ_b, the maximum frictional resistance of a smooth unweathered clean joint, for the Kelly Burn Sandstone and the explains the methods subsequently used to derive φ_b for samples of material from the Nantlle Valley.

As mentioned above large (117 mm) diameter sliding tests are described in Appendix C. Two of the core samples used were subsequently subsampled to produce 25 mm diameter cores (Figure 7-3), which were then subjected to small scale tilt tests (Figure 7-4). Unlike the tests described in Appendix C, inclination was measured using an application on a mobile phone rather than a compass clinometer. However, and just as with the tests documented in Appendix C, the sliding tests were undertaken by placing the sliding core onto the pair of basal cores when set to a predetermined angle. This was considered appropriate to ensure accuracy in knowing test inclination angle, the need for repeated tests at the same angle and to avoid the lack of control associated with hand-held tilting

and the associated vibrations. Preliminary measurements using a phone-based accelerometer indicated that hand-tilting grossly exceeded the threshold acceleration value of 0.005 *g* suggested by Pérez-Rey et al. (2019), therefore handheld tilting was not explored further. Strictly speaking such an approach determines the angle at which sliding is not arrested, rather than the angle at which sliding was initiated for static cores subject to tilting. Any difference is considered small.

To minimise smoothing of the sliding surface and the effect of local variations in core surface texture sliding distances were minimised and both basal and sliding cores were rotated axially and swapped amongst each other in an ordered fashion to obtain an average α value. All cores exceeded a 2:1 slenderness ratio and any cores showing perceptible necking from the coring process were not tested. Results are discussed in section 7.4.4.

Figure 7-3 Coring to recover 25 mm diameter samples.

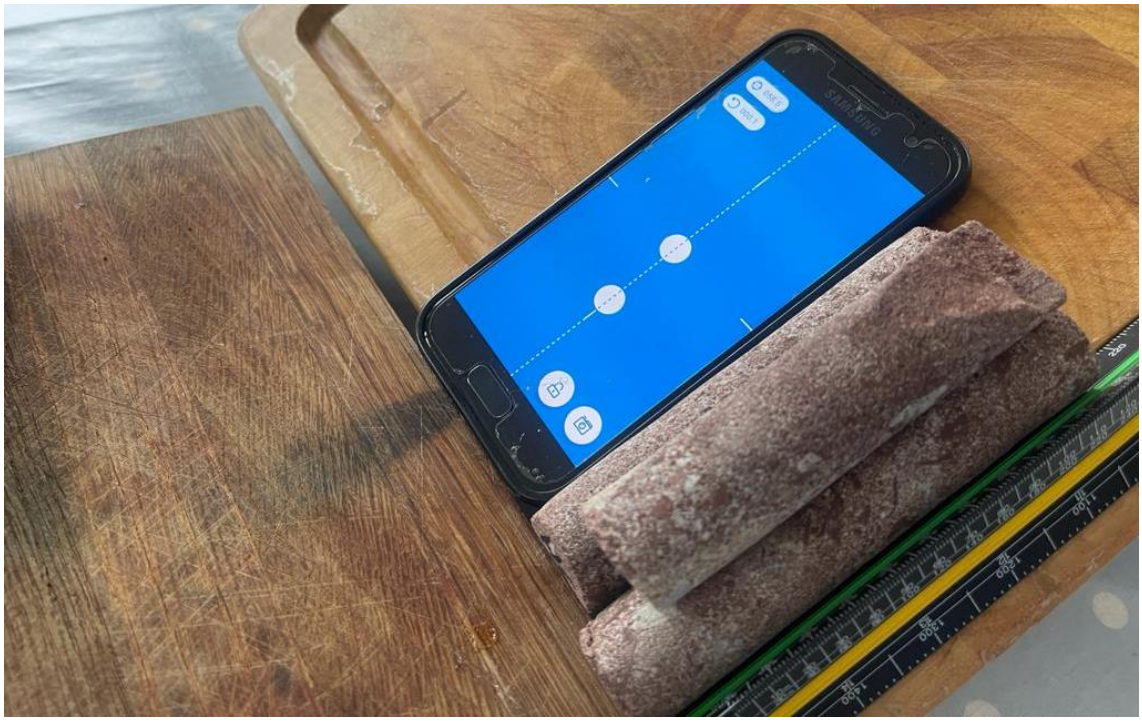

Figure 7-4 Small scale tilt tests on Kelly Burn Sandstone with inclinometer.

7.4.2 Disc sliding tests

117 mm diameter core samples of the Kelly Burn Sandstone were cut diametrically using an angle grinder. The cut surface was not planar and showed the marks of the cutting process (Figure 7-5 left). To create smooth surfaces for subsequent sliding tests the discs were ground flat, initially by grinding opposing cut faces against one another by hand (Figure 7-5) before finishing with a 10" ceramic file, washing and air drying. The flattening process was undertaken mindful to minimise the potential for preferential smoothing by using a circular motion of the opposing disc or the file. A single face on each of four discs was prepared from 117 mm diameter core in this fashion to allow nine disc sliding combinations. Discs met the geometry and area criteria described by Pérez-Rey et al. (2019). An average value of ϕ_b = 32.7° was determined, with all samples failing at 32° or 33°.

Figure 7-5 Preparation of discs for sliding tests.

Figure 7-6 Tilt test on discs of Kelly Burn Sandstone.

7.4.3 Sliding tests on axially cut cores

The same process described above was used to prepare two halves of a short length to axially cut core (Figure 7-7). This gave a sliding area >50 cm^2, as recommended by

Pérez-Rey et al. (2019). An initial value of ϕ_b = 35° was followed by the sliding angle degrading to 34°, highlighting the sensitivity of the material to polishing / smoothing.

Figure 7-7 Preparation of axially cut cores for tilt testing.

7.4.4 Comparison of results

Mean values of ϕ_b determined from four different types of tilt tests are listed in Table 7.1. The highest value was associated with the small diameter (25 mm) three-core tilt tests and it may be no coincidence that the small diameter samples are also associated with the lowest stress level for which higher apparent frictional resistance may be expected. There was a small difference between the disc and axially cut cores, suggesting that the method of surface preparation common to both was not the only control on sliding resistance.

The two highest values were determined from the 117 mm and 25 mm diameter three-core axial sliding method. For α values of 35.5° and 37.2° for 117 mm and 25 mm diameter samples the calculated value of ϕ_b was 31.7° and 33.3° respectively. These values align reasonably well with values obtained from the other types of test. For the

reason provided in section 8.1.1 this reduced multiplier is considered more representative of material behaviour. The calculated failure envelope and shear strength parameters for the Kelly Burn Sandstone are provided as in Appendix C.3 and C.4.

$$\varphi_b = tan^{-1}(1.155 \tan \alpha)$$

Equation 7.3 Relationship of φ_b from α, from Stimpson (1981).

$$\varphi_b = tan^{-1}(0.866 \tan \alpha)$$

Equation 7.4 Revised relationship of φ_b and α, from Alejano et al. (2012).

Test type	ϕ_b
Tilt tests on 117 mm diameter core (Appendix C)	31.7°
Tilt tests on 25 mm diameter core (section 7.4.1)	33.3°
Tilt tests on disc samples (section 7.4.2)	32.7°
Tilt tests on axially cut cores (section 7.4.3)	35°

Table 7.1 Comparison of values of ϕ_b from different types of tilt test.

8 Barton's failure envelope for rocks of the Nantlle Valley

8.1 Input parameters

8.1.1 Basic friction angle

Table 8.1 gives values of ϕ_b determined for the geological units tested using the 25 mm diameter three-core tilt test described in section 7.4.1. Also shown in italics are value of ϕ_b determined from tests on two other geological units not in the Nantlle Valley for which subsequent comparisons of rock mass strength were made.

Geological unit	Sample location	α	ϕ_b
Padarn Tuff Formation	SH 56167 61264	34.0°	30.3°
Fachwen Formation	SH 56399 61017	33.0°	29.4°
Llanberis Slates Formation	SH 49556 52219	33.6°	29.9°
Grit horizon within Llanberis Slates Formation	SH 49730 52394	34.6°	30.9°
Bronllwyd Grid Formation	SH 59558 58995	34.0°	30.3°
Carnedd Y Filiast Grit Member	SH 55329 53761	34.5°	30.8°
Pitts Head Tuff Formation	SH 51353 50664	35.0°	31.2°
Microgranite	SH 53978 54680	35.0°	31.2°
Nantlle Dolerite	SH 54741 54332	35.0°	31.2°
Titterstone Clee Hill Dolerite	*SO 59581 77923*	*36.0°*	*32.1°*
Land's End Granite	*SW 35332 26337*	*35.0°*	*31.2°*

Table 8.1 Values of ϕ_b determined based on Equation 7.4.

The value determined for the Llanberis Slate Formation samples (29.9°) is close to the value of 30° quoted by Douglas et al. (1983).

Samples from the Nant Ffrancon Subgroup and Marchlyn Formation repeatedly disintegrated when cored. After obtaining additional sample material and cutting and finishing as described in sections 7.4.2 and 7.4.3 values of ϕ_b were determined from block sliding tests. The irregular shape of the sample of the Marchlyn Formation proved difficult to mount stably for multiple sliding tests at different angles. The solution adopted was to mount the sample proud of a water filled tray which, when frozen, allowed the tray to be set to the desired test angle (Figure 8-1). Immediately prior to testing condensation rapidly forming on the cold surface of the sample was removed with a hairdryer.

Geological unit	Sample location	ϕ_b
Nant Ffrancon Subgroup	SH 56331 54080	28.0°
Marchlyn Formation	SH 55224 53435	29.0°

Table 8.2 Values of ϕ_b from block sliding tests.

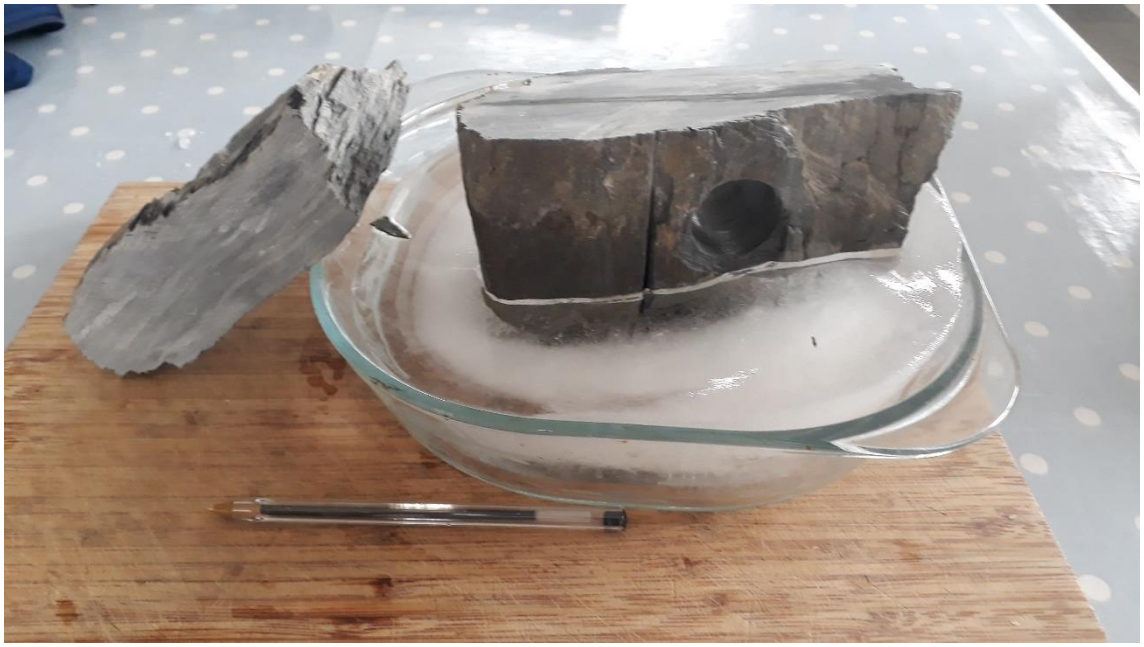

Figure 8-1 Ice mounted block sample for tilt testing.

8.1.2 Joint compressive strength

JCS was determined from the mean of the upper half of Schmidt hammer measurements from various locations covering the various geological units of the study area. Appendix C describes the method adopted to calibrate the Schmidt hammer subsequently used for fieldwork against rock cores of known strength.

Based on the number of tests required to determine a coefficient of variation ≤5% (Appendix C), a minimum of twenty two measurements of JCS were made using a Schmidt hammer at each field location. At each location the test was undertaken perpendicular to the exposed joint surface and the orientation of the test recorded to allow for subsequent correction, if later required.

8.1.3 Joint roughness coefficient

JRC was determined from joint surfaces exposed in outcrop with the aid of a 6" profile gauge compared to Barton's JRC profiles (Figure 7-2). Where possible pairs of measurements were made perpendicular to one another on a joint surface to allow an aggregate value of JRC to be taken to remove bias associated with otherwise imperceptible roughness variation or accidental orientation bias.

8.2 Calculated shear strength envelopes

8.2.1 The Padarn Tuff Formation

Using Equation 7.2 a value of R for unweathered material of 59.8 MPa and mean weathered strength (r) = 53.1 MPa as well as a ϕ_b measured from small diameter sliding tests (Table 8.1) gave a value of ϕ_r = 28.1°. Using an average JRC of 6.3 based on a range from 4 to 10 the shear strength envelope (Figure 8-4) and shear strength parameters (Table 8.3) were calculated using Equation 7.1. The strength envelope shown is curtailed at the

materials compressive strength, consistent with the onset of failure through intact material (Barton, 2014). Figure 8-2 shows the fresh and weathered Padarn Tuff Formation (SH 56167 61264) and Figure 8-3 shows fiamme textures observed.

Figure 8-2 Fresh and weathered Padarn Tuff Formation.

Figure 8-3 Fiamme structures in the Padarn Tuff Formation.

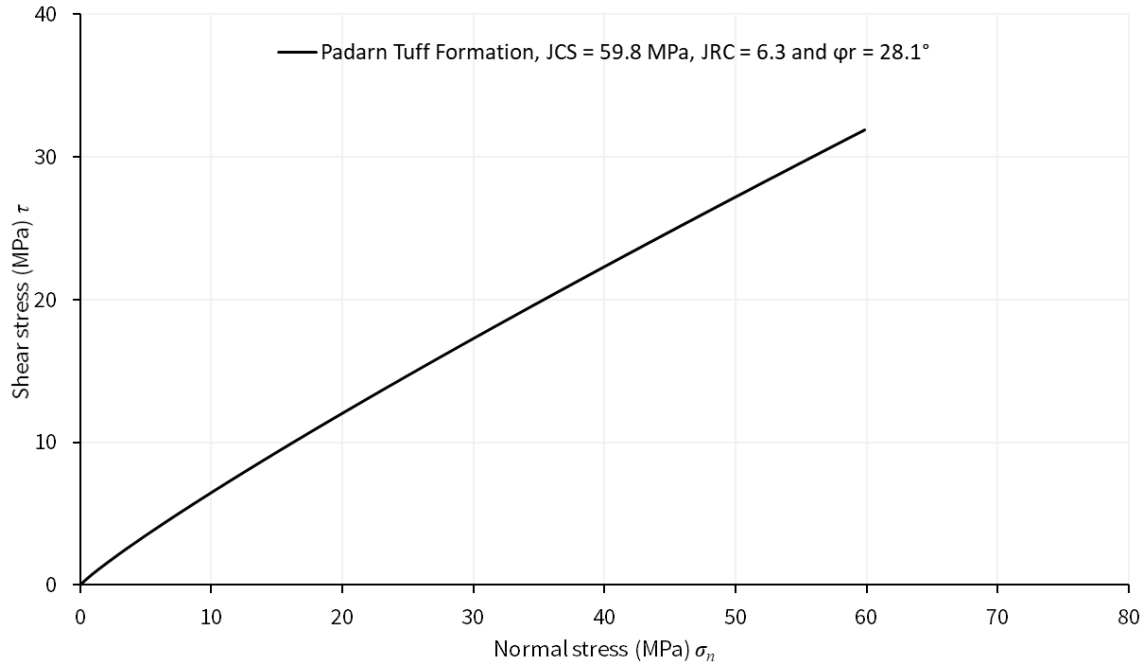

Figure 8-4 Padarn Tuff Formation: Shear strength envelope.

σ_n	τ	ϕ_i	c_i
1 MPa	0.8 MPa	36.4°	0.08 MPa
5 MPa	3.5 MPa	32.0°	0.35 MPa
10 MPa	6.5 MPa	30.1°	0.68 MPa
15 MPa	9.3 MPa	29.0°	0.99 MPa
20 MPa	12.0 MPa	28.3°	1.30 MPa
25 MPa	14.7 MPa	27.6°	1.60 MPa
30 MPa	17.3 MPa	27.1°	1.91 MPa
35 MPa	19.8 MPa	26.7°	2.20 MPa
40 MPa	22.3 MPa	26.4°	2.50 MPa
45 MPa	24.8 MPa	26.0°	2.80 MPa
50 MPa	27.2 MPa	25.8°	3.09 MPa
55 MPa	29.6 MPa	25.5°	3.38 MPa

Table 8.3 Padarn Tuff Formation: Instantaneous shear strength parameters.

8.2.2 The Fachwen Formation

For R = 53.4 MPa, r = 49.7 MPa and ϕ_b = 29.4° a ϕ_r = 28.0° was calculated, adopting a typical JRC = 10 gave the strength envelope shown as Figure 8-5, and parameters in Table 8.4. Figure 8-6 shows weathered and fresh surfaces, from which strength was measured.

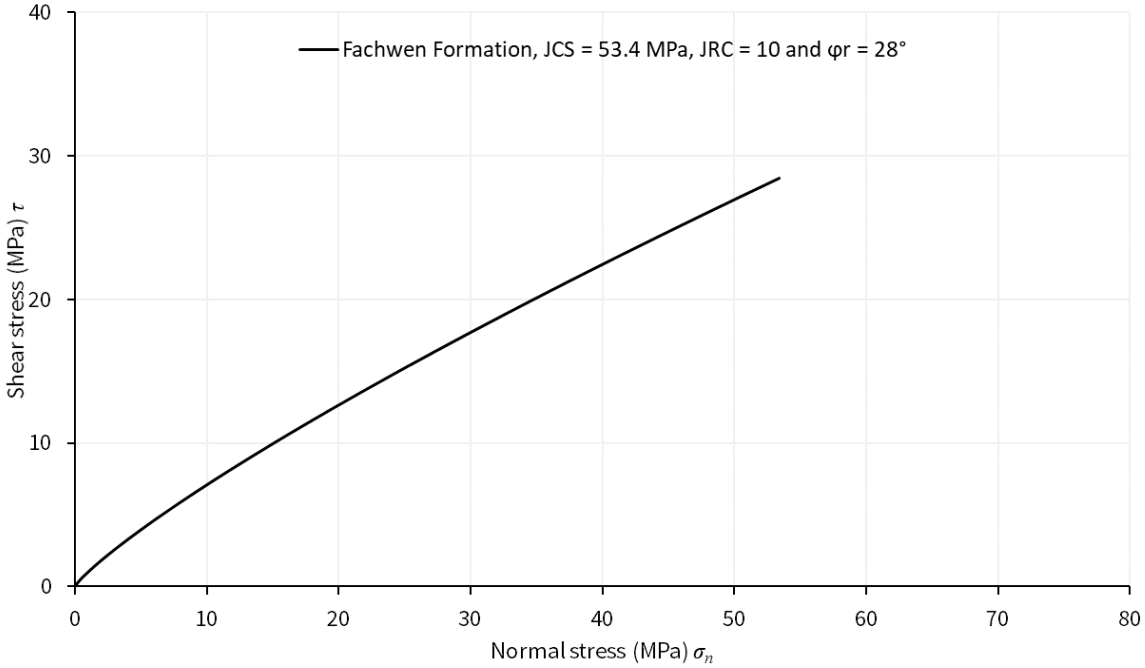

Figure 8-5 Fachwen Formation: Shear strength envelope.

σ_n	τ	ϕ_i	c_i
1 MPa	1.0 MPa	40.6°	0.15 MPa
5 MPa	4.0 MPa	33.7°	0.61 MPa
10 MPa	7.1 MPa	30.7°	1.14 MPa
15 MPa	9.9 MPa	29.0°	1.63 MPa
20 MPa	12.6 MPa	27.7°	2.12 MPa
25 MPa	15.2 MPa	26.8°	2.59 MPa
30 MPa	17.7 MPa	26.0°	3.06 MPa
35 MPa	20.1 MPa	25.3°	3.52 MPa
40 MPa	22.4 MPa	24.8°	3.98 MPa
45 MPa	24.7 MPa	24.3°	4.43 MPa
50 MPa	26.9 MPa	23.8°	4.88 MPa
55 MPa	29.1 MPa	23.4°	5.33 MPa
60 MPa	31.3 MPa	23.0°	5.77 MPa

Table 8.4 Fachwen Formation: Instantaneous shear strength parameters.

Figure 8-6 Fresh and weathered Fachwen Formation (SH 56399 61017).

8.2.3 The Llanberis Slates Formation

The calculated shear strength of the Llanberis Slates Formation is shown as Figure 8-7, which shows a near-linear envelope as a consequence of a low average JRC of 2.3. Figure 8-7 is based on a mean JCS = 58.4 MPa, which is also the value of R for unweathered material used to determine ϕ_r = 26.2° (Equation 7.2) based on a mean weathered strength (r) of 47.5 MPa and a measured value of ϕ_b = 29.9° (Table 8.1). Instantaneous shear strength parameters ϕ_i and c_i are provided (Table 8.5) based on the method described in Appendix C.4.

Unweathered strength measurements were taken from Tŷ Mawr Quarry (SH 49489 52164) and weathered measurements from a tramway cutting near Dorothea Quarry (SH 50073 53390). A photograph of the unweathered material tested is provided as Figure

8-8, along with the range of colours of slates observed (Figure 8-9) as well as copper mineralisation observed along joint surfaces (Figure 8-10).

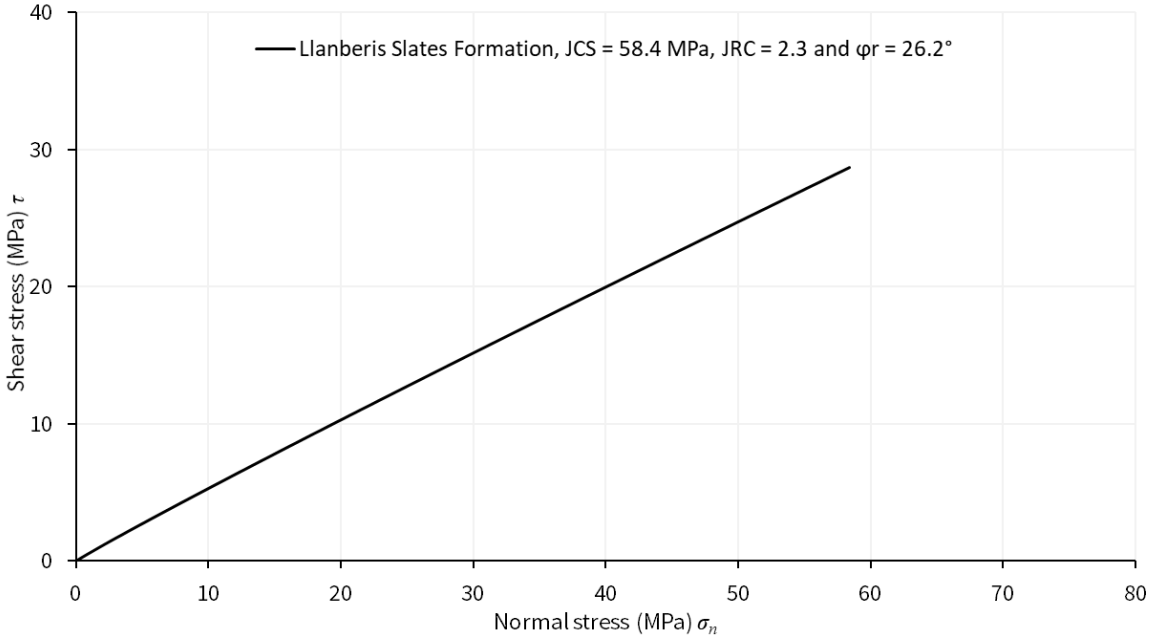

Figure 8-7 Shear strength envelope for the Llanberis Slates Formation.

σ_n	τ	ϕ_i	c_i
1 MPa	0.6 MPa	29.2°	0.02 MPa
5 MPa	2.7 MPa	27.6°	0.11 MPa
10 MPa	5.3 MPa	26.9°	0.22 MPa
15 MPa	7.8 MPa	26.5°	0.33 MPa
20 MPa	10.3 MPa	26.2°	0.44 MPa
25 MPa	12.7 MPa	26.0°	0.55 MPa
30 MPa	15.2 MPa	25.8°	0.66 MPa
35 MPa	17.6 MPa	25.7°	0.76 MPa
40 MPa	20.0 MPa	25.5°	0.87 MPa
45 MPa	22.3 MPa	25.4°	0.98 MPa
50 MPa	24.7 MPa	25.3°	1.08 MPa
55 MPa	27.1 MPa	25.2°	1.19 MPa

Table 8.5 Llanberis Slates Formation: Instantaneous shear strength parameters.

Figure 8-8 Unweathered Llanberis Slates Formation (SH 49489 52164).

Figure 8-9 Coloured slates of Tŷ Mawr Quarry, each approximately 350 mm long.

Figure 8-10 Copper mineralisation at SH49556 52219 in Tŷ Mawr Quarry.

8.2.4 Grit horizon within the Llanberis Slates Formation

The shear strength envelope for a grit horizon within the Llanberis Slates Formation was determined from material with fresh (SH 59520 58995) and weathered (SH 59558 58998) mean strengths of 54.8 and 50.4 MPa respectively. A mean JRC of 8.7 was used, based on a range from 8 to 10, with a ϕ_r = 33.0° (Equation 7.2) determined from ϕ_b = 34.6° (Table 8.1). The surface used to determine unweathered strength was interpreted to be fresh from the observed presence of pyrite. An individual boulder also allowed both a fresh and weathered, or part weathered surface, to be observed (Figure 8-12).

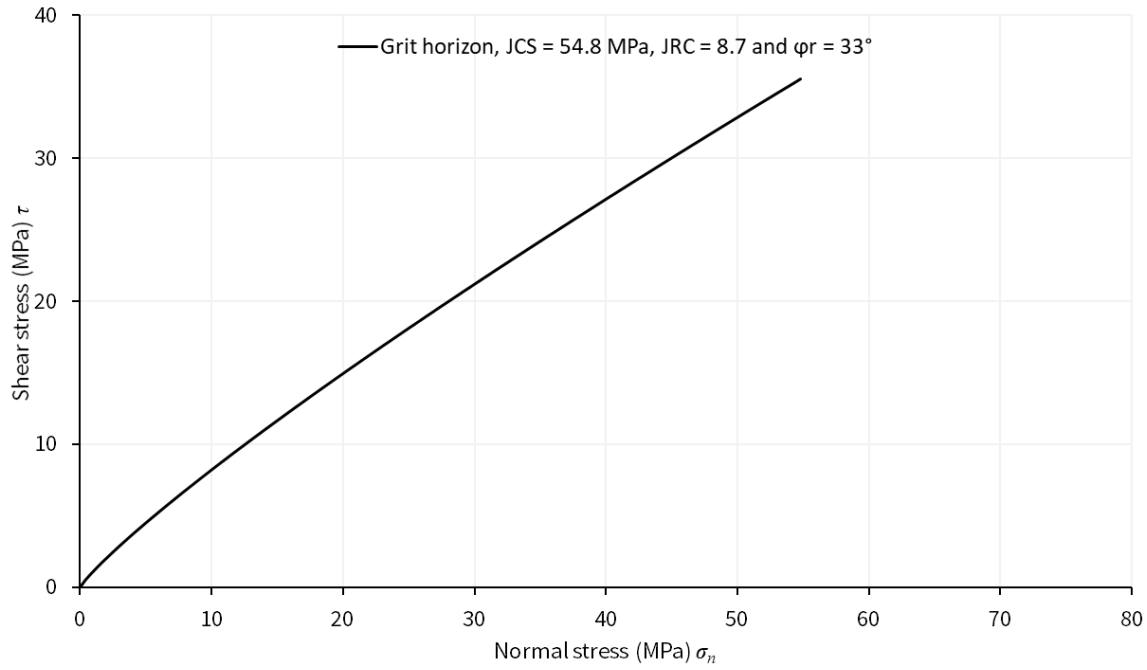

Figure 8-11 Grit horizon: Shear strength envelope.

σ_n	τ	ϕ_i	c_i
1 MPa	1.1 MPa	44.1°	0.15 MPa
5 MPa	4.5 MPa	38.0°	0.60 MPa
10 MPa	8.2 MPa	35.4°	1.10 MPa
15 MPa	11.7 MPa	33.9°	1.59 MPa
20 MPa	15.0 MPa	32.8°	2.05 MPa
25 MPa	18.1 MPa	32.0°	2.51 MPa
30 MPa	21.2 MPa	31.3°	2.96 MPa
35 MPa	24.2 MPa	30.7°	3.41 MPa
40 MPa	27.2 MPa	30.2°	3.85 MPa
45 MPa	30.1 MPa	29.8°	4.28 MPa
50 MPa	32.9 MPa	29.4°	4.72 MPa

Table 8.6 Grit horizon: Instantaneous shear strength parameters.

Figure 8-12 Weathered and fresh interior of the same boulder (SH49730 52394).

8.2.5 The Bronllwyd Grit Formation

The shear strength envelope for the Bronllwyd Grit Formation (Figure 8-13) is based on a JCS = 64.2 MPa, a mean JRC = 12 (range 10 to 14) and ϕ_r = 27.7°. In calculating these values, a weathered strength of 52.4 MPa and ϕ_b =30.3° were used. Weathered and unweathered measurement of strength were based on outcrops at SH 59520 58995 (Figure 8-14) and SH 59558 58998 respectively, on the side of the A4086 southeast of Llanberis. Shear strength parameters are provided as Table 8.7.

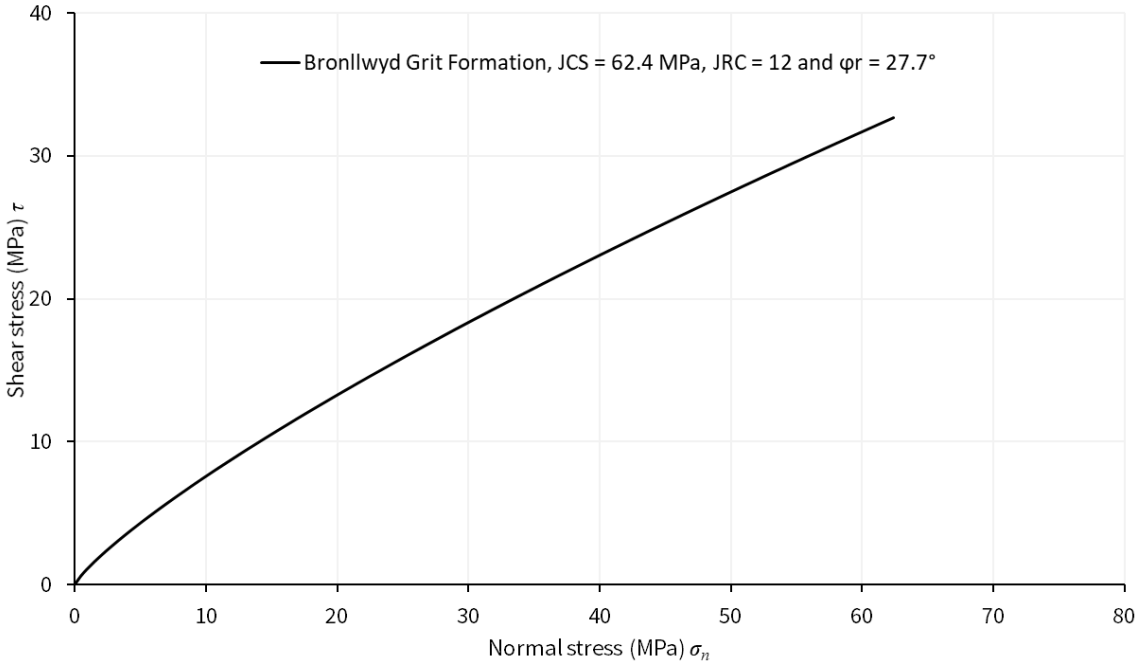

Figure 8-13 Bronllwyd Grit Formation: Shear strength envelope.

σ_n	τ	ϕ_i	c_i
1 MPa	1.2 MPa	43.4°	0.21 MPa
5 MPa	4.3 MPa	35.2°	0.79 MPa
10 MPa	7.6 MPa	31.6°	1.43 MPa
15 MPa	10.5 MPa	29.5°	2.03 MPa
20 MPa	13.3 MPa	28.1°	2.62 MPa
25 MPa	15.9 MPa	26.9°	3.19 MPa
30 MPa	18.4 MPa	26.0°	3.75 MPa
35 MPa	20.8 MPa	25.2°	4.30 MPa
40 MPa	23.1 MPa	24.5°	4.84 MPa
45 MPa	25.3 MPa	23.9°	5.38 MPa
50 MPa	27.5 MPa	23.4°	5.91 MPa
55 MPa	29.6 MPa	22.9°	6.44 MPa

Table 8.7 Bronllwyd Grit Formation: Instantaneous shear strength parameters.

Figure 8-14 Bronllwyd Grit Formation exposed in road cutting (SH 59520 58995).

8.2.6 The Carnedd Y Filiast Grit Member

Figure 8-15 shows the shear strength envelope for the Carnedd Y Filiast Grit Member and Table 8.8 provides instantaneous shear strength parameters. These are based on an unweathered strength of 58 MPa (SH 53748 53319), a weathered strength of 44.8 MPa

(SH 53740 53292), a mean JRC = 10 (range 8 to 12) and ϕ_b and ϕ_r of 30.8° and 26.2° respectively.

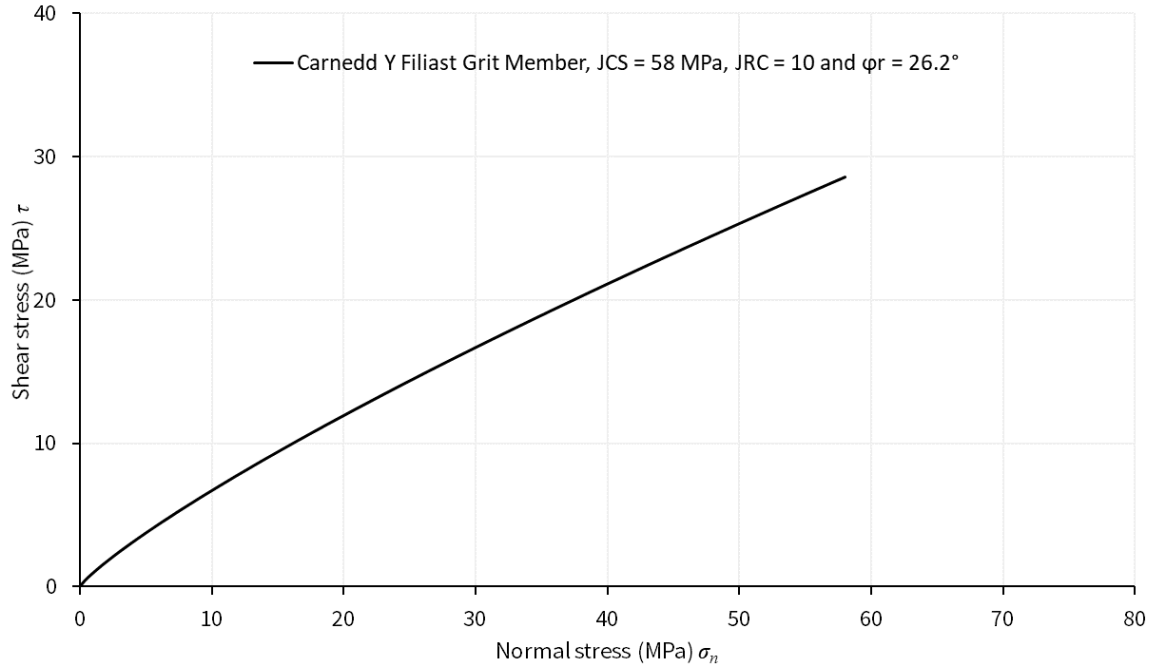

Figure 8-15 Carnedd Y Filiast Grit Member: Shear strength envelope.

σ_n	τ	ϕ_i	c_i
1 MPa	1.0 MPa	39.2°	0.15 MPa
5 MPa	3.8 MPa	32.3°	0.59 MPa
10 MPa	6.7 MPa	29.3°	1.10 MPa
15 MPa	9.4 MPa	27.6°	1.58 MPa
20 MPa	12.0 MPa	26.3°	2.05 MPa
25 MPa	14.4 MPa	25.4°	2.52 MPa
30 MPa	16.7 MPa	24.6°	2.97 MPa
35 MPa	18.9 MPa	23.9°	3.42 MPa
40 MPa	21.1 MPa	23.3°	3.87 MPa
45 MPa	23.3 MPa	22.8°	4.32 MPa
50 MPa	25.3 MPa	22.4°	4.76 MPa
55 MPa	27.4 MPa	22.0°	5.19 MPa

Table 8.8 Carnedd Y Filiast Grit Member: Instantaneous shear strength parameters.

8.2.7 The Marchlyn Formation

Figure 8-16 shows the Marchlyn Formation's shear strength envelope and shear strength parameters (Table 8.9). These are based on an unweathered strength of 57.8 MPa (SH 55329 53761), a weathered strength of 27.4 MPa (SH 55707 53066), a mean JRC = 6 (range 5 to 9) and ϕ_b and ϕ_r of 29.0° and 18.5° respectively.

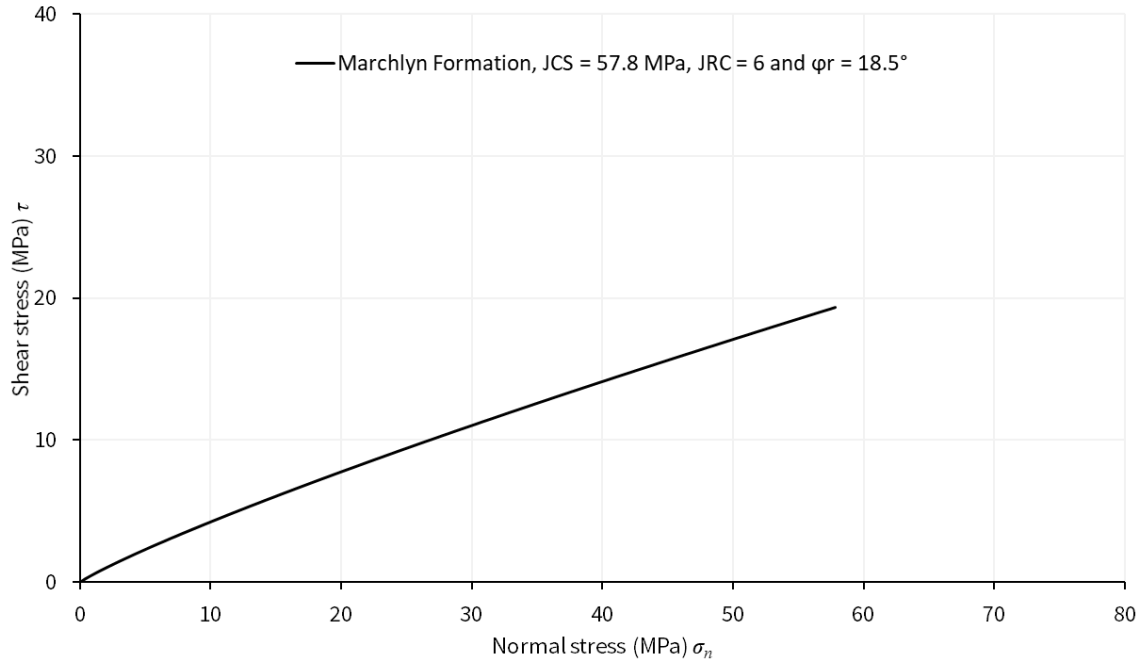

Figure 8-16 Marchlyn Formation: Shear strength envelope.

σ_n	τ	ϕ_i	c_i
1 MPa	0.6 MPa	26.4°	0.06 MPa
5 MPa	2.3 MPa	22.2°	0.28 MPa
10 MPa	4.3 MPa	20.4°	0.54 MPa
15 MPa	6.1 MPa	19.4°	0.79 MPa
20 MPa	7.8 MPa	18.6°	1.05 MPa
25 MPa	9.4 MPa	18.0°	1.30 MPa
30 MPa	11.0 MPa	17.6°	1.55 MPa
35 MPa	12.6 MPa	17.2°	1.80 MPa
40 MPa	14.1 MPa	16.8°	2.04 MPa
45 MPa	15.6 MPa	16.5°	2.29 MPa
50 MPa	17.1 MPa	16.2°	2.54 MPa
55 MPa	18.5 MPa	16.0°	2.78 MPa

Table 8.9 Marchlyn Formation: Instantaneous shear strength parameters.

8.2.8 The Nant Ffrancon Subgroup

Coring of samples of the Nant Ffrancon Subgroup either disintegrated or did not yield cores with sufficient length:width ratios to allow a value of ϕ_b to be determined by core sliding tests. An average ϕ_b = 28° was established from five sliding samples on block samples hand sawn from a large fresh sample recovered from a newly cut forestry track (Figure 8-18). Samples were filed flat and all yielded values of 27°, 28° or 29°. Barton's failure envelope is shown below as Figure 8-17 and shear strength parameters as Table 8.10. The Nant Ffrancon Subgroup is the weakest of all the rock masses considered in this study, but forms the bulk of the proposed tunnel's length for the proposed hydropower development.

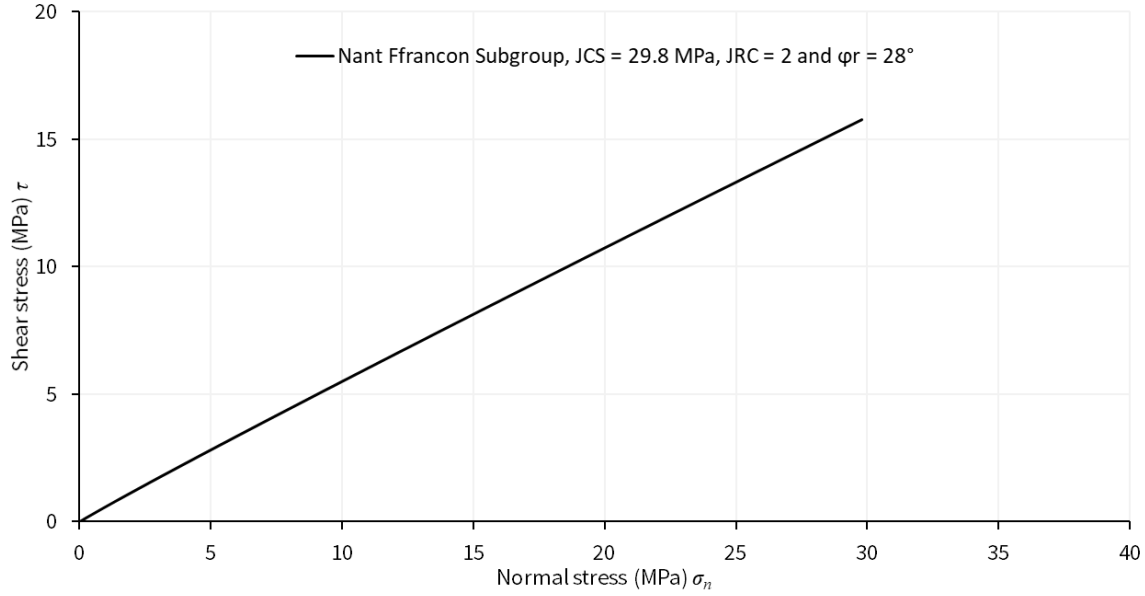

Figure 8-17 Nant Ffrancon Subgroup: Shear strength envelope.

σ_n	τ	ϕ_i	c_i
1 MPa	2.8 MPa	28.6°	0.10 MPa
5 MPa	5.5 MPa	28.0°	0.20 MPa
10 MPa	8.1 MPa	27.6°	0.29 MPa
15 MPa	10.7 MPa	27.4°	0.39 MPa
20 MPa	13.3 MPa	27.2°	0.49 MPa
25 MPa	15.9 MPa	27.0°	0.58 MPa

Table 8.10 Nant Ffrancon Subgroup: Instantaneous shear strength parameters.

Figure 8-18 Forest track exposing Nant Ffrancon Subgroup (SH 56331 54080).

Figure 8-19 Prepared block samples and sliding test (left).

8.2.9 The Pitts Head Tuff Formation

Measurements on the Padarn Tuff Formation from SH 51353 50664 (Figure 8-21) and subsequent tilt tests from samples from the same location allowed calculation of the strength envelope (Figure 8-20) as well as corresponding instantaneous parameters to be

calculated (Table 8.11). This utilised R = 64.3 MPa, r = 59.0 MPa, ϕ_b = 31.2°, ϕ_r = 29.6° and a mean JRC = 6 based on a range of 4 to 8 (Figure 8-22).

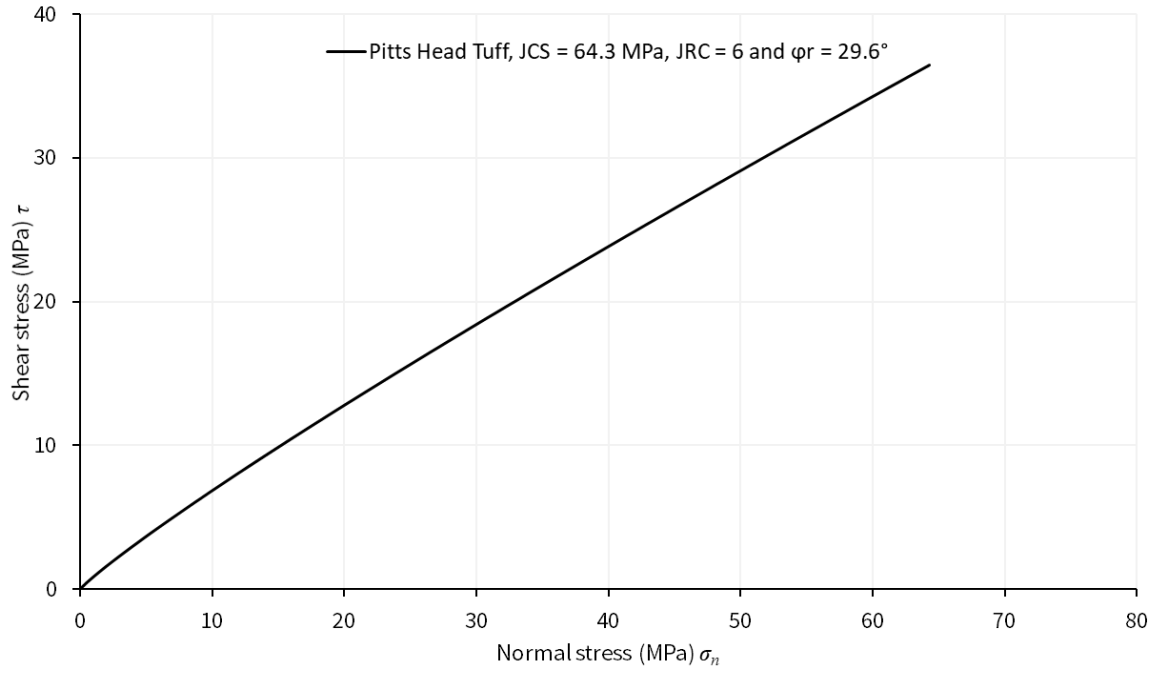

Figure 8-20 Pitts Head Tuff Formation: Shear strength envelope.

σ_n	τ	ϕ_i	c_i
1 MPa	0.9 MPa	37.7°	0.08 MPa
5 MPa	3.7 MPa	33.5°	0.35 MPa
10 MPa	6.8 MPa	31.7°	0.67 MPa
15 MPa	9.9 MPa	30.7°	0.98 MPa
20 MPa	12.8 MPa	29.9°	1.28 MPa
25 MPa	15.6 MPa	29.3°	1.58 MPa
30 MPa	18.4 MPa	28.9°	1.88 MPa
35 MPa	21.2 MPa	28.5°	2.17 MPa
40 MPa	23.8 MPa	28.1°	2.46 MPa
45 MPa	26.5 MPa	27.8°	2.75 MPa
50 MPa	29.1 MPa	27.5°	3.04 MPa
55 MPa	31.7 MPa	27.3°	3.33 MPa
60 MPa	34.3 MPa	27.1°	3.61 MPa

Table 8.11 Pitts Head Tuff Formation: Instantaneous shear strength parameters.

Figure 8-21 Pitts Head Tuff Formation outcrop (SH 51353 50664).

Figure 8-22 Typical joint surface in the Pitts Head Tuff Formation.

8.2.10 Mynydd Mawr Microgranite

Figure 8-23 shows the calculated shear strength envelopes for the unnamed flow banded intrusion forming the mountain of Mynydd Mawr (SH 53978 54680). This had one of

the highest compressive strength of the materials encountered with R = 63.9 MPa, r = 62.9 (Figure 8-24) and ϕ_r = 34.7° based on a measured ϕ_b = 35.0°. Values of JRC were either in the range of 2 to 4 or 6 to 8. Strength envelopes for both JRC = 2 and a JRC of 8 are provided showing the difference attributable to the variations in JRC observed. Estimated shear strength parameters are provided in Table 8.12.

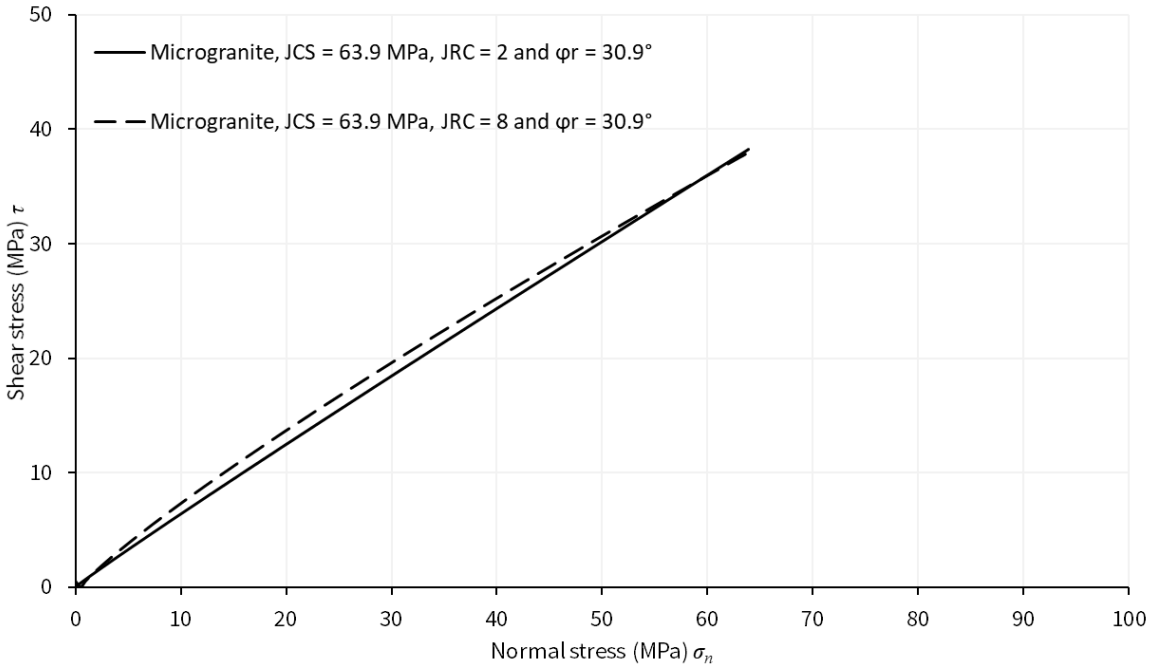

Figure 8-23 Microgranite: Shear strength envelope.

	Lower bound JRC = 2			Upper bound JRC = 8		
σ_n	τ	ϕ_i	c_i	τ	ϕ_i	c_i
1 MPa	0.7 MPa	33.6°	0.02 MPa	1.0 MPa	41.6°	0.12 MPa
5 MPa	3.3 MPa	32.2°	0.11 MPa	4.2 MPa	36.1°	0.51 MPa
10 MPa	6.4 MPa	31.6°	0.21 MPa	7.6 MPa	33.7°	0.96 MPa
15 MPa	9.4 MPa	31.3°	0.32 MPa	10.9 MPa	32.3°	1.38 MPa
20 MPa	12.4 MPa	31.0°	0.42 MPa	14.0 MPa	31.3°	1.80 MPa
25 MPa	15.4 MPa	30.8°	0.52 MPa	17.0 MPa	30.5°	2.21 MPa
30 MPa	18.4 MPa	30.7°	0.63 MPa	19.9 MPa	29.9°	2.61 MPa
35 MPa	21.4 MPa	30.5°	0.73 MPa	22.7 MPa	29.4°	3.01 MPa
40 MPa	24.3 MPa	30.4°	0.83 MPa	25.5 MPa	28.9°	3.41 MPa
45 MPa	27.2 MPa	30.3°	0.93 MPa	28.2 MPa	28.5°	3.80 MPa
50 MPa	30.2 MPa	30.2°	1.03 MPa	30.9 MPa	28.1°	4.19 MPa
55 MPa	33.1 MPa	30.1°	1.13 MPa	33.6 MPa	27.8°	4.57 MPa
60 MPa	36.0 MPa	30.1°	1.23 MPa	36.2 MPa	27.5°	4.95 MPa

Table 8.12 Microgranite: Instantaneous shear strength parameters.

Figure 8-24 Microgranite boulders at the top of Mynydd Mawr (SH 53978 54680).

Figure 8-25 Flow textures within the microgranite of Mynydd Mawr.

8.2.11 Nantlle dolerite

Figure 8-26 shows the shear strength envelope for the dolerite encountered and Table 8.13 provides the accompanying shear strength parameters. These are based on unweathered strength of 68.9 MPa (SH 50073 53390), a weathered strength of 56.7 MPa (SH 50073 53390) a mean JRC = 2.7 (range 2 to 3) and ϕ_b and ϕ_r of 31.2° and 27.6° respectively. The low JRC gives a near linear profile to the calculated failure envelope.

Figure 8-27 shows the weathered intrusion near the top of Mynydd Mawr where samples were collected for subsequent coring.

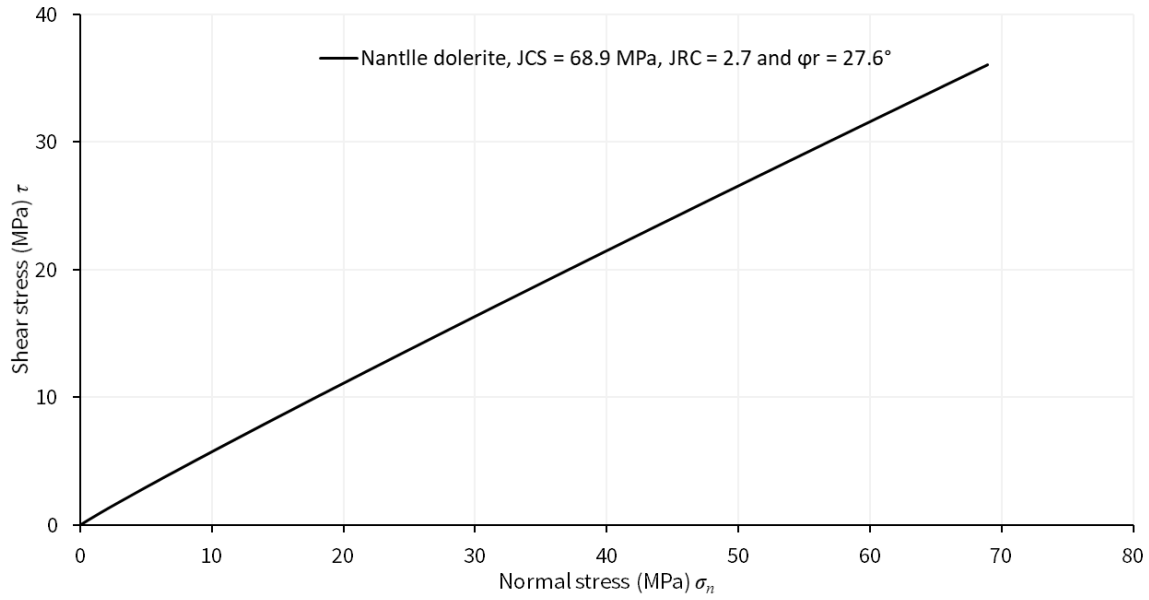

Figure 8-26 Dolerite: Shear strength envelope.

σ_n	τ	ϕ_i	c_i
1 MPa	0.6 MPa	31.4°	0.03 MPa
5 MPa	3.0 MPa	29.5°	0.14 MPa
10 MPa	5.8 MPa	28.7°	0.27 MPa
15 MPa	8.5 MPa	28.2°	0.40 MPa
20 MPa	11.1 MPa	27.9°	0.54 MPa
25 MPa	13.8 MPa	27.7°	0.67 MPa
30 MPa	16.4 MPa	27.4°	0.80 MPa
35 MPa	19.0 MPa	27.3°	0.92 MPa
40 MPa	21.5 MPa	27.1°	1.05 MPa
45 MPa	24.1 MPa	27.0°	1.18 MPa
50 MPa	26.6 MPa	26.8°	1.31 MPa
55 MPa	29.1 MPa	26.7°	1.44 MPa
60 MPa	31.6 MPa	26.6°	1.57 MPa
65 MPa	34.1 MPa	26.5°	1.69 MPa

Table 8.13 Dolerite: Instantaneous shear strength parameters.

Figure 8-27 Dolerite instruction exposed on Mynydd Mawr (SH 54741 54332).

8.3 Comparison of strength envelopes

8.3.1 Comparison of metapelites

The strength envelopes of the metamorphosed mudstones of the Llanberis Slates Formation and Nant Ffrancon Subgroup are shown together as Figure 8-28, both materials do not show pronounced nonlinearity due to low JRC values. There is a contrast in maximum strength due to the relative difference in intact strength of the materials, however this is only relevant for stress levels >30 MPa.

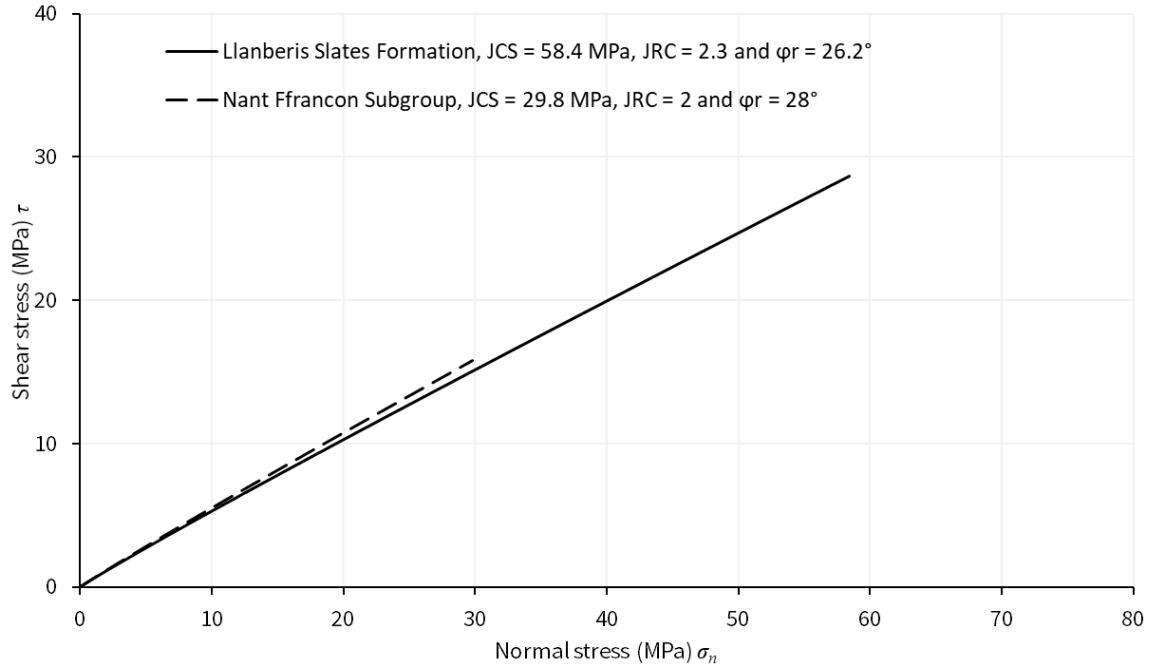

Figure 8-28 Shear strength envelopes for the metapelites tested.

8.3.2 Comparison of metapsammites

A comparison of the strength envelopes of the Fachwen and Bronllwyd Formations as well as the Carnedd Y Filiast Grit Member and a grit horizon from within the Llanberis Slates Formation is provided as Figure 8-29. This shows the steeper failure envelope of the highest friction material of the grit within the Llanberis Slates Formation and broad similarity of the envelopes of the other three units of comparable frictional properties and ascribed values of JRC.

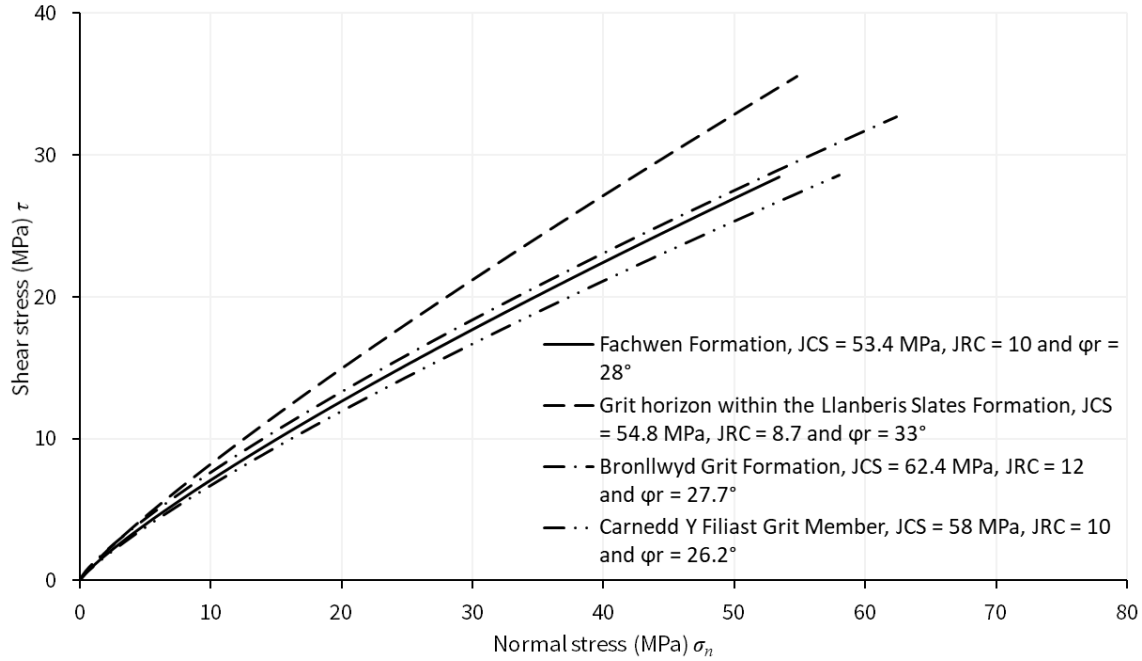

Figure 8-29 Comparison of metapsammites tested.

8.3.3 Comparison of tuff materials

The Pits Head Tuff and Padarn Tuff Formations yielded similar JRC values, 6 and 6.3, and ϕ_r values, 29.6° and 28.1° respectively, and had compressive strengths within 5 MPa of one another. The mass behaviour of these materials is therefore very similar (Figure 8-30).

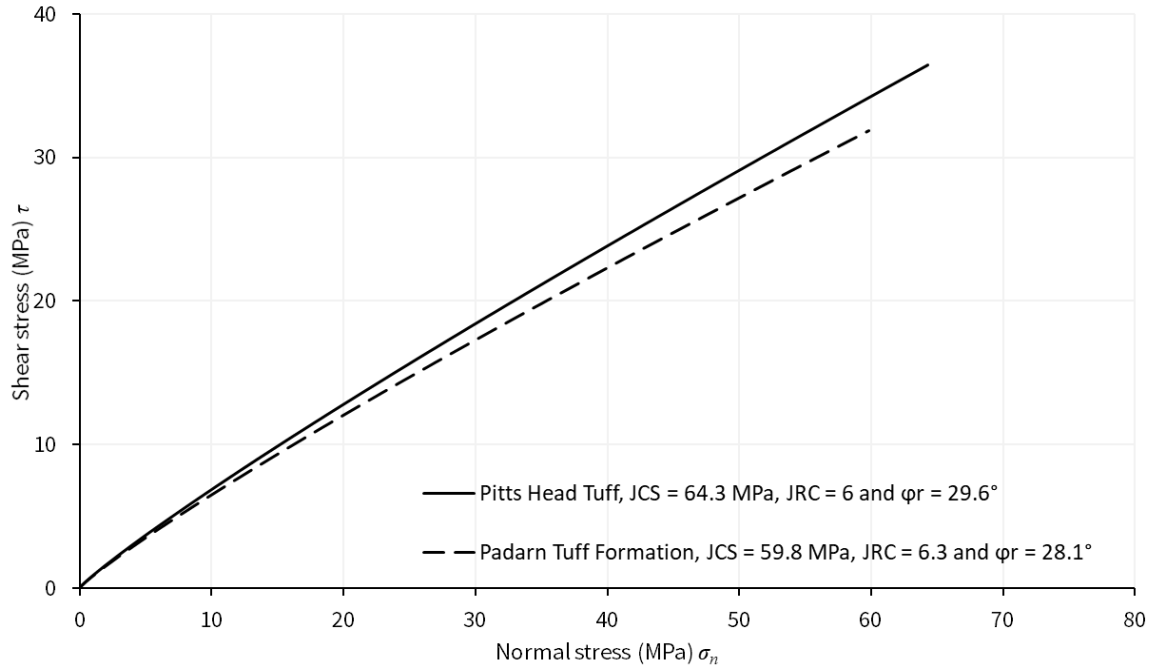

Figure 8-30 Strength envelopes for Padarn and Pitts Head Tuff Formations.

8.3.4 Other geological units tested

During an initial period of fieldwork identifying unweathered dolerite suitable for testing proved difficult. To avoid the potential absence of any suitable material for coring, samples of dolerite from Titterstone Clee Hill, Shropshire (SO 59581 77923) were taken with the intention of using such material as a contingent proxy for the material of the Nantlle Valley. In addition to obtaining samples, measurements needed for strength envelope determination were also made. This allows comparison of two different dolerites (Figure 8-31), albeit from different geological settings, but of otherwise comparable bulk chemistry and crystal size. This shows that despite similarity in rock type, the strength envelopes differ greatly. Although the Nantlle dolerite had the greater compressive strength, its mass strength was less than that of the Titterstone Clee Hill material as a consequence of a lower ϕ_r, i.e. a greater ratio of *R*:*r*. Values of ϕ_b obtained

from sliding testes for the Clee Hill and Nantlle dolerites were comparable at 32.8° and 31.2° respectively.

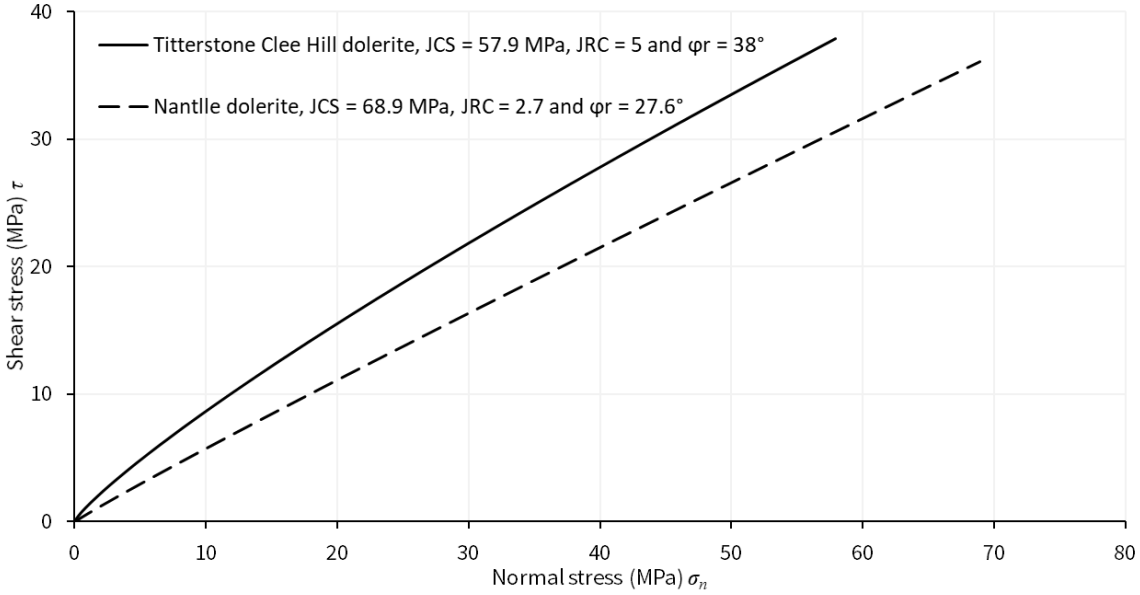

Figure 8-31 Shear strength envelopes for Nantlle and Clee Hill dolerites.

Knowing that there were no strength envelopes to compare the microgranite of Mynydd Mawr to, a strength envelope for the coarsely crystalline granite of the Land's End Granite exposed at Sennen Cove, Cornwall (SW 35332 26337) was determined for comparative purposes. A comparison of the two (Figure 8-32), shows they have similar compressive strengths and values of ϕ_r. Both had the same value of ϕ_b (31.2°), established from small diameter sliding tests, suggesting that ϕ_b is not exclusively related to crystal size.

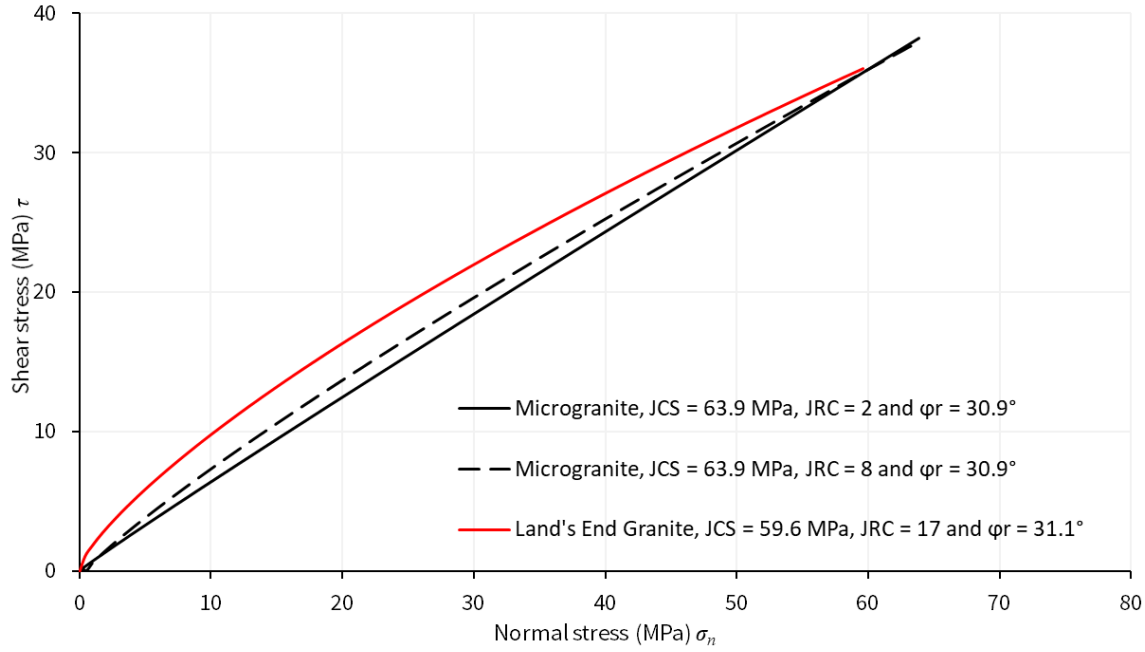

Figure 8-32 Comparison of Nantlle and Land's End Granites.

8.4 Revisiting slope stability

The sidewall of Dorothea Quarry previously analysed and discussed in section 6.3 was reassessed using Rocscience's Slide software with Barton's criterion presented in section 8.2.3 used in place of Hoek-Brown parameters. The calculated factor of safety, <0.5, indicates the impossible situation of an unsustainably steep / high slope (Figure 8-33). With reference to Figure 8-33 it appears that the general geometry of the failure is closer to that observed for the Talysarn type failure since the failure surface is steep and closer to the original slope face. This appears a better replication of the failure observed than that predicted from the extensive iterative process discussed in section 6 using the Generalised Hoek-Brown criterion.

A subsequent analyse with the value of JCS doubled from 58.4 MPa to 116.8 MPa resulted in the calculated factor of safety increasing from 0.457 to 0.469 (+2.6%). The measurements undertaken as part of this study as well as those of Davies (2020) do not

support such an increase in strength, but the additional analyses highlight the relative insensitivity of predicted stability to intact strength at low stresses, and potential errors in strength determination. By comparison keeping the original, measured JCS of 58.4 MPa and doubling JRC from 2.3 to 4.6 increased the factor of safety from 0.457 to 0.578 (+26%). Again, this is inconsistent with field observations and the very smooth planar nature of joints in slaty materials. Although the general geometry of the predicted failure fits better with the Talysarn failure strengths or JRC cannot rationally be increased to establish a factor of safety close to unity. As alluded to in section 3.3 this may be due to reliance on tensile rather than compressive strength parameters, especially given the steep overall angle of the slope and uncertainty about the role of stress relief (section 3.6).

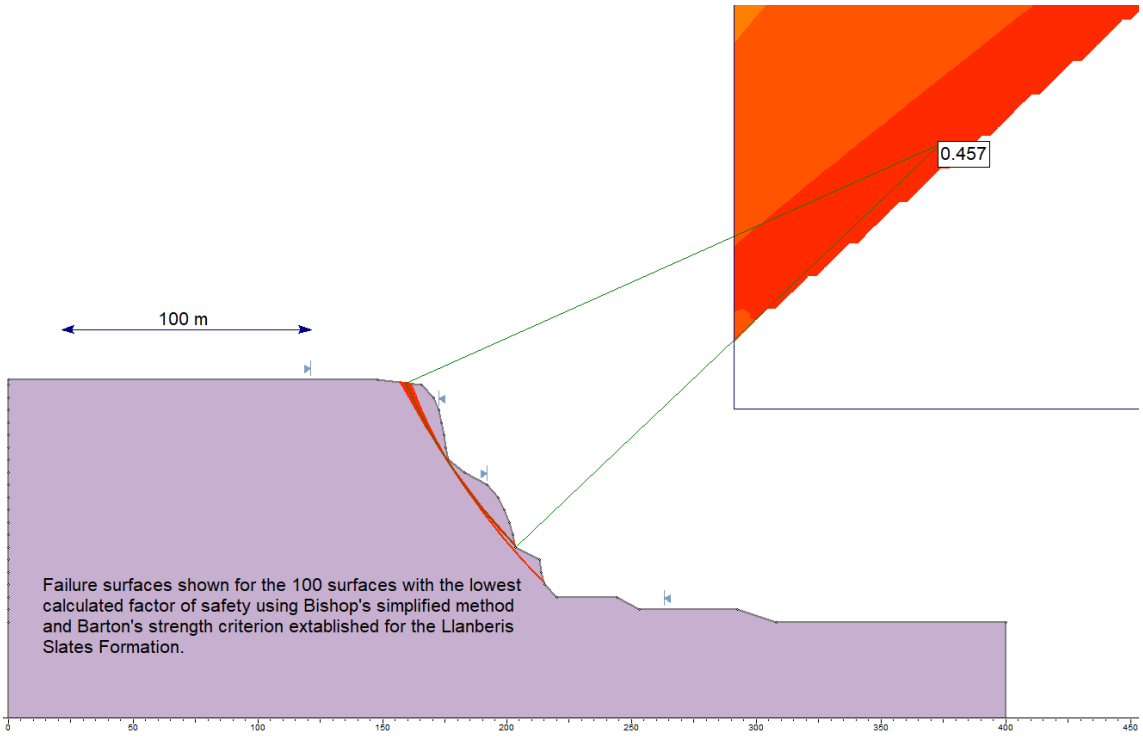

Figure 8-33 Slope stability analysis using Barton's criterion.

8.5 Comparison of Hoek-Brown and Barton shear strength envelopes

Rocscience's Slide software uses the method of Hoek et al. (2002) to determine a Generalised Hoek-Brown strength envelope in terms of normal and shear stress. Generalised Hoek-Brown strength envelopes have been exported from Slide and plotted alongside Barton's envelope for the Llanberis Slates Formation (section 8.2.3). Note that only part of the curve relevant to the Slide analysis undertaken is available for export giving the envelope an artificially truncated appearance.

Figure 8-34 shows the considerable difference in strengths at low stresses between the Barton and Generalised Hoek-Brown criteria as well as, in this instance, significantly greater curvature of the Hoek-Brown envelope compared to the near linear behaviour of Barton's criterion. For σ_n <10 MPa the Hoek-Brown envelope indicates strength considerably greater that that estimated by Barton's criterion on the same material.

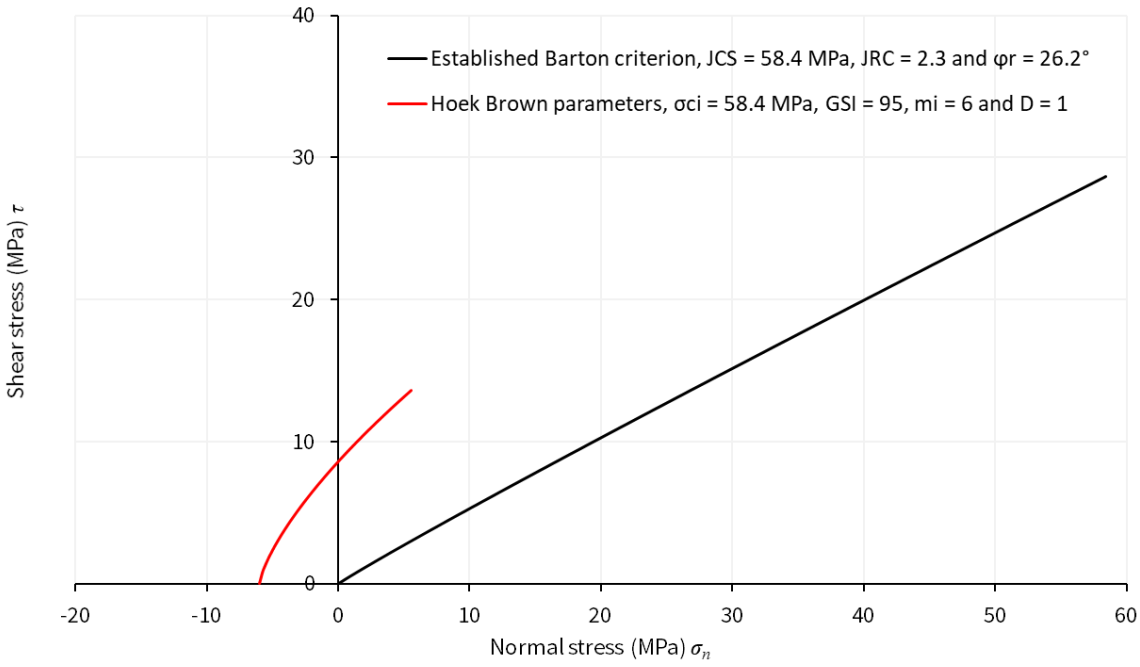

Figure 8-34 Hoek-Brown and Barton envelopes for the Llanberis Slates Formation.

9 Conclusions

9.1 Applicability of strength criteria

No conclusions can be drawn from the work undertaken as to the suitability of either the Generalised Hoek-Brown or Barton criteria for characterising the rock masses considered. All the rock masses investigated are hard brittle masses and based on the available information remain potentially equally well characterised by either criterion for continuum modelling.

Slope stability analyses showed that a significant rock slope failure could not be explained by either criterion. This point must be appreciated by anybody involved in assessing the stability of the steep high rock slopes of the Dorothea quarries. The potential causes of the failure are discussed in section 9.6. The analyses undertaken do not capture the observed mode of failure despite protracted efforts to simulate in-situ stress redistribution from quarry excavation in the FLAC analyses.

The ease and simplicity of determining Barton's criterion is extremely appealing, in part because of the ease of determining the input parameters and clear importance of each parameter. Increased testing would also allow input parameters to be rigorously scrutinised and the associated variability to be quantified by further data collection. Establishing input parameters is not subjective and it's not clear how any bias or inexperience of the user can easily influence the envelope determined.

By comparison, the Generalised Hoek-Brown's criterion requires, ideally, advanced testing and has an element of subjectivity in the use of GSI. There remains uncertainty as to what value of the disturbance factor, *D*, to adopt for anything other than a slope. While these points do not invalidate the use of the criterion it does require caution,

combined with experience and direct observation, in using the criterion. On this basis alone Barton's criterion is considered preferable.

The more fundamental issue of Hoek-Brown's criterion having a cohesion intercept at zero normal stress cannot be easily explained. This may be inconsequential if the criterion is applied to situations where normal stress is positive, however this would appear to be extremely limiting.

The very high RQD, and therefore GSI, of the materials investigated indicate that mass behaviour is likely to reflect intact behaviour with relatively little influence from discontinuities. The exception to this being where the near vertical slaty cleavage of the Llanberis Slates Formation has been allowed to open in response to horizontal unloading and potentially preventing the use of continuum mechanics.

9.2 Barton's strength criterion

9.2.1 Calculated strength envelopes

Barton's failure envelope was calculated for the following geological units of the Nantlle Valley:

- The Padarn Tuff Formation,
- The Fachwen Formation,
- The Llanberis Slates Formation,
- A grit horizon within the Llanberis Slates Formation,
- The Bronllwyd Grit Formation,
- The Carnedd Y Filiast Grit Member,
- The Marchlyn Formation,
- The Nant Ffrancon Subgroup,

- The Pitts Head Tuff Formation,
- A microgranite of Mynydd Mawr,
- A dolerite intrusion on top of Mynydd Mawr.

For comparative purposes and by obtaining contingent samples, strength envelopes were also determined for:

- The Land's End Granite, Cornwall,
- A dolerite intrusion of Titterstone Clee Hill, Shropshire.

In trialling the methods subsequently used to determine strength envelopes a strength envelope for the Kelly Burn Sandstone of Ayrshire was also established.

Barton's criterion proved quick and straightforward to determine from basic tests that allowed instantaneous shear strength parameters to be calculated. The strength envelopes established may be considered a single snapshot of the non-linear behaviour of the rock masses tested and cannot be considered definitive, not least because there will be spatial lithological and discontinuity variation that cannot be captured within this study. One point of caution to highlight from the Titterstone Clee Hill testing was the wide spectrum of weathering that exists in nature. In the case of Titterstone Clee Hill, material was observed that was completely weathered, i.e. degraded to a soil, and as such judgement has to be exercised when determining mass strength from outcrop that weathered surfaces are not unduly pessimistic. This would be avoided where borehole samples are used as any weathering or alteration of joint surfaces clearly reflects conditions inside the rock mass, rather than at its degraded periphery.

9.2.2 Basic friction angle

ϕ_b was obtained from a combination of block sliding tests, cores cut into discs, cores cut axially as well as sliding cores over one another. A comparison of the results (Table 7.1) indicated that all except the sliding tests on axial cut cores were within 1.6° of one another, sufficiently close for test related differences to be captured by subsequent sensitivity checks if used for design or analysis purposes. The similarity of results between the tests is reassuring as different sliding tests were not repeated on all materials tested. The sliding tests on an axial cut cores yielded a result 1.7° higher than the next highest sliding test, this may be a product of having the greatest contact area but cannot be attributed to the method of surface preparation, which was the same as the disc sliding tests. This may be bully addressed by the Barton-Bandis behavioural model which was developed to take account of sample size.

Similarly, the difference in values of ϕ_b obtained from the same preparation process on contrasting lithologies confirms that the preparation process alone is not the only control on the value of ϕ_b determined. A single published value of the friction angle of 30° adopted for the design of Dinorwic (Douglas et al., 1983) aligned well with the result of 29.9° obtained from small diameter core sliding tests using the modification of Stimpson's (1981) relationship between sliding angle (α) and ϕ_b prvided by Alejano et al. (2012).

The use of small diameter cores (25 mm) to determine ϕ_b proved practical and effective. The use of small diameter cores allowed samples from hand specimens to be subsampled. This is hugely advantageous as it means that samples can be orientated and not restricted by the orientation of an exploratory core as cores can, and were, subsampled. The ability to orientate small diameter cores would allow orientation dependant frictional properties

to be explored experimentally. This may be of relevance with sheared materials or where there is pronounced anisotropy and would be interesting to compare to non-strength related anisotropic fabrics.

9.3 Strength envelopes for powerhouse and tunnel construction

Of most relevance to the potential Dorothea Lakes development are the strength envelopes shown in Figure *9-1*. This figure shows the calculated envelopes for the Llanberis Slates Formation, within which the powerhouse, outfall structure as well as the lowermost part of the tunnel would be constructed. Also shown are the failure envelopes for the Bronllwyd Grit Formation, which would constitute a relatively short length of the tunnel, and the Nant Ffrancon Subgroup, which would comprise the bulk of the tunnel's length and provide the foundation for the dam and intake structure. The strength envelope of a grit horizon within the Llanberis Slates Formation is also shown. The associated instantaneous shear strength parameters are tabulated in section 8.2.

With reference to Figure *9-1* the most pronounced curvature is associated with the Bronllwyd Grit Formation while the two pelite derived units are considerably more linear in their behaviour. Despite having the highest compressive strength, the rock mass of the Llanberis Slates Formation is the weakest of the materials associated with the tunnel's alignment.

With respect to likely stress levels, it is understood that the powerhouse will be approximately 60 m below existing ground level, corresponding to a vertical stress of approximately 1.62 MPa. The ratio of horizontal:vertical stress is not known, however for credible ratios of 2:1 or 3:1 horizontal stresses of 3.24 to 4.86 MPa are possible. As discussed in section 3.3, far field stress may be concentrated three-fold around an

unsupported circular opening, such as a tunnel in the temporary condition. Depending on the initial stress ratios it is therefore possible that stress concentrations in the rock mass may be of the order of 10 to 15 MPa for construction at 60 m depth.

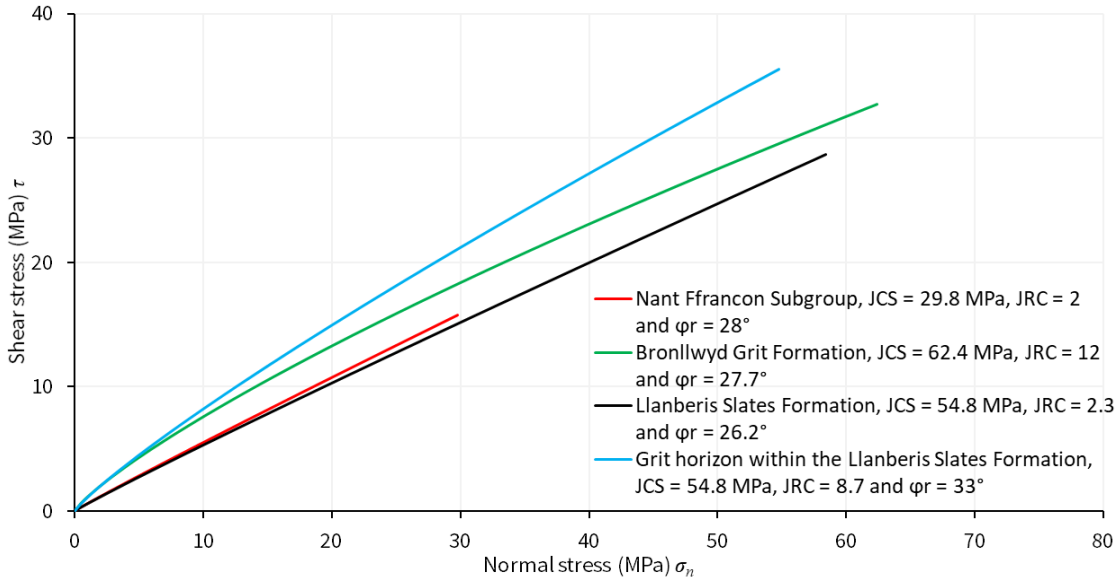

Figure 9-1 *Shear strength envelopes for tunnel and powerhouse construction.*

9.4 Observations from strength envelope derivation

The strength envelopes determined allowed direct comparison of lithologically similar materials. The tuffs of the Padarn and Pitts Head Tuff Formations (Figure 8-30 repeated as Figure 9-2) showed remarkably similar strength envelopes and the two Formations appear to have more in common than just rock type.

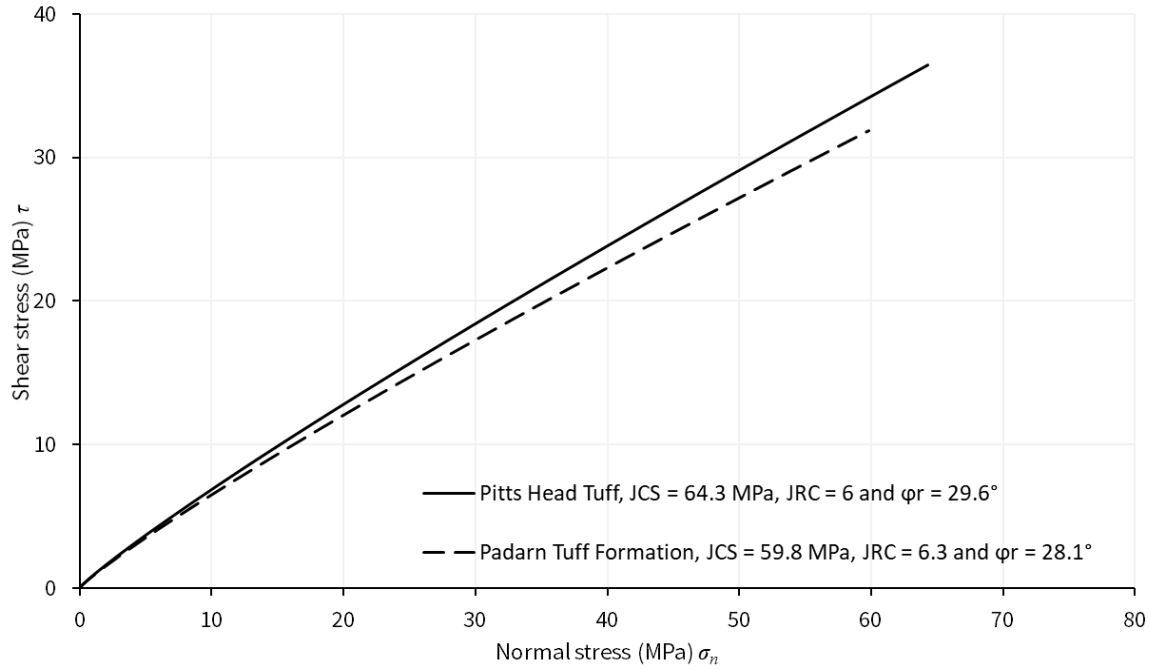

Figure 9-2 Strength envelopes for Padarn and Pitts Head Tuff Formations.

A comparison of two granitic materials (Figure 8-32 repeated as Figure 9-3), shows they have similar compressive strengths and values of ϕ_r. Both had the same value of ϕ_b (31.2°), established from small diameter sliding tests, suggesting that ϕ_b is not exclusively related to crystal size. The pronounced non-linearity of the Land's End material is attributable to a much higher JRC, which might reasonably be assumed to relate to greater mean crystal size. If mean crystal size is a control on JRC then the relatively low values of JRC for the Titterstone Clee Hill and Nantlle dolerites, 5 and 2.7 respectively, as well as the range of values for the microgranite (2 to 8) support this.

Variability in input parameters can be expected, as can be seen from Figure 9-3 the potential bimodal variability in the range of JRC has implications for the strength envelope calculated. This is highlighted as an area that requires consideration, especially where JRC is determined from drill core which is highly susceptible to orientation bias.

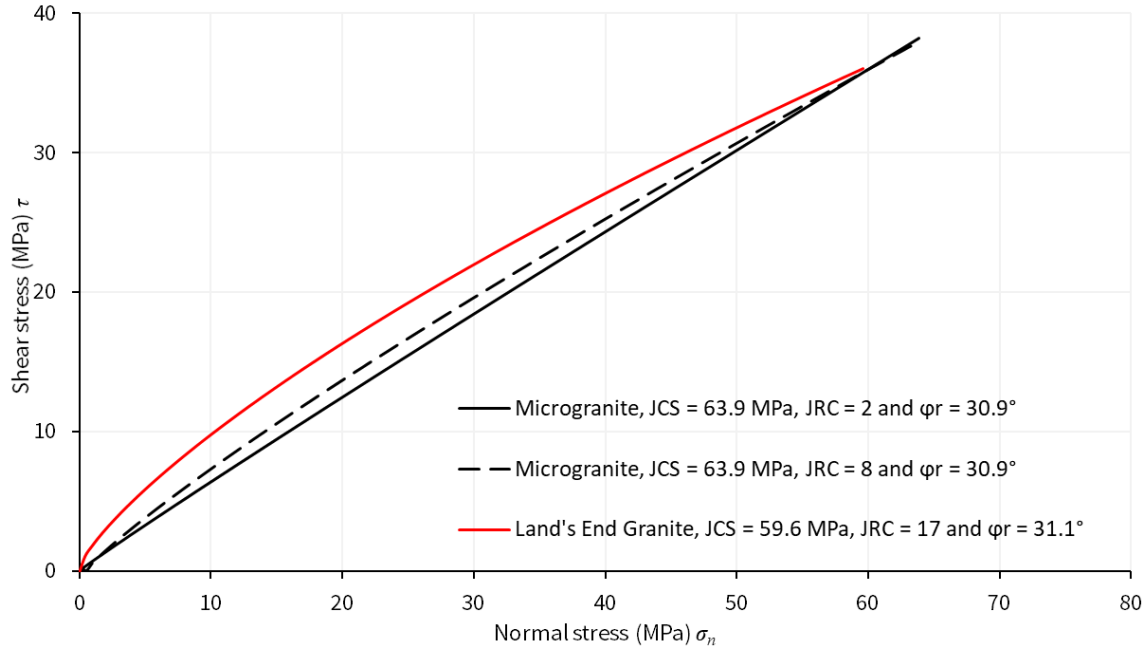

Figure 9-3 Comparison of Nantlle and Land's End Granites.

9.5 Numerical simulations of rock mass behaviour

A parametric study was undertaken sequentially downgrading Hoek-Brown parameters to determine the combinations of parameters that led to predicted failure of a worst-case cross section through Dorothea Lake. A section through Dorothea Lake was used as no bathymetry data was available for Talysarn Quarry. Numerical simulations were undertaken using Itasca's FLAC software using a staged excavation and recalculation of in-situ stress to try to replicate stress relief of the rock mass from excavation of the quarry itself. The FLAC analyses undertaken are complex and did not yield results that are sensitive to σ_t or replicate the very steep geometry of the Talysarn failure. Progressively downgrading Hoek-Brown parameters until failure was predicted allowed failure-critical combinations to be determined

The results of FLAC analyses with a factor of safety of <1.5 were corroborated by results obtained from a verification exercise using Rocscience's Slide software to analyse the

same slope geometry and combinations of parameters (except tension) using Bishop's simplified method of slices for a circular failure surface. Slide results were within 5% of those calculated from FLAC, except for material with σ_{ci} >10 MPa, GSI = 60 and m_i = 10 which were within 8% of one another. Slide seeks a circular failure, normally appropriate to isotropic homogeneous materials, whereas SLIDE allows the identification of non-circular modes of failure. The results of the numerical simulation using different software and methods of calculating stability are considered to provide mutual corroboration of one another.

Combinations of parameters required for failure to occur (Table 6.1) were not observed during the fieldwork undertaken, which is consistent with strength and rock quality data recorded by Davies (2020). On this basis neither the Generalised Hoek-Brown or Barton criterion could be used to simulate the slope failure observed and an alternative explanation for the failure is required. This does not mean that the criteria are invalid, simply that they could not explain the failure observed, probably because of the role of tension developed in response to unloading.

9.6 Talysarn slope failure: mode and timing of failure

The failure appears to have propagated through intact rock, exposing fresh rock and appears independent of readily identifiable discontinuities. The failure was therefore not simply movement of a discontinuity bound block whose kinematic freedom could be predicted from knowledge of discontinuity orientation relative to the quarry wall. Having discounted both the Hoek-Brown and Barton behaviour as explanations of the failure other explanations were sought.

It is considered most likely that the failure is attributable to the development of tensile stresses, or absence of compression, due to horizontal unloading of the rock mass from quarrying. A state of tensile stress, or zero compressive stress, can be explained using Hooke's law (section 3.6) and can be expected in the volume of rock "feeling" horizontal stress relief from excavation of the adjacent quarry. Horizonal unloading is suggested to allow existing joints to open up or new joints to develop where stress relaxation cannot be accommodated elastically. Where tensile stresses develop, they are concentrated at rock bridges, for which Griffith theory provides a useful explanation. Assuming tensile stresses remain below the tensile strength of intact rock at rock bridges the slope remains stable. Using the method explained by Barton and Shen (2018) the minimum tensile strength required to sustain 115m high slope was estimated to be 0.64 MPa (section 3.3), less than the minimum value of 2.61 MPa recorded elsewhere in the slate belt (Table 3.3). However, even for low tensile stresses a discontinuity of limited extent rapidly concentrates stress at rock bridges to a point where stresses equal then exceed the available tensile strength.

With respect to a potential trigger for the failure, many decades after cessation of quarrying, quarry water levels being in a state of equilibrium and in the absence of surcharging or seismic activity it is suggested that there may be a combination of contributory factors. Contributory factors could include the initial "opening up" the rock mass to weathering from the relaxation of joints, followed by the penetration of water and air into the unweathered rock mass allowing weathering to start or accelerate. Any associated hydration or volume changes of clay minerals is likely to contribute to prying forces further opening of joints and fractures. Over time the rupture or extension of joints further concentrates stress at the on remaining rock bridges and penetration of water into

the otherwise dry fabric of the rock. Eventually failure of rock bridges and joint extension results in stress concentrations that cannot be sustained, at which point failure propagates through the intact rock.

Reiterating Hudson and Harrison (1997) and Cai (2010), the stress required to initiate a tension cracks is close to the tensile strength of rock and the stress release from crack initiation can allow tensile failure to develop. It is therefore not inconceivable to envisage "cliff-edge" effects where small, localised yielding of a limited number of rock bridge changes stress distribution to a point that rapidly becomes unsustainable and will result in failure. It may be that this is what was observed at Talysarn with spalling of the rock face from April 2020 before ultimate collapse in July 2020. Had acoustic monitoring been available it may have been of use tracing the development of the failure. Similarly monitoring P-wave arrivals from the ruptures would have allowed not only the failure propagation to have been observed but also established the orientation of stress axes and confirmed the role of tension in the failure, or otherwise.

Although the mineralogy of the Llanberis Slates Formation has not been considered in this study, freshly broken samples reveal visible pyrite crystals, which undergo volume changes and are easily oxidised when exposed. The observed presence of pyrite provides one possible explanation for volumetric changes as a result of mineral weathering aiding joint prying, propagation and the penetration of water into the rock mass.

Close to the rockface itself it is considered likely that the introduction of more pronounced diurnal thermal stresses will also have contributed to the degradation of the rock face.

Although analyses using both the Barton and Hoek-Brown criteria did not allow the Talysarn failure to be satisfactorily back analysed to give a calculated factor of safety for

credible parameters this may reflect uncertainty about the use of either criterion at relatively low stresses associated with the slopes analysed. It may be the case that one criteria replicates the mass behaviour, albeit at higher stresses.

9.7 Adoption of continuum modelling and the role of anisotropy

Another reason why neither criterion was successful in predicting slope failure satisfactorily may be due to the relatively massive nature of the Llanberis Slates Formation. With reference to the Generalised Hoek-Brown criterion, and as suggested by Bertuzzi et al. (2016), the very high GSI values (>90) reported by Davies (2020) may well cause the rock mass to behave as an intact mass.

Similarly, the absence of pronounced joints causing instability ensures intact behaviour dominates and makes the role of joint smoothness in Barton's criterion ineffective in predicting mass behaviour in this instance. The general absence of discontinuities causing localised kinematic type failures (e.g. wedge, sliding or toppling) from the rock slopes of the Dorothea area would appear to support the conclusion that joints appear not to influence mass behaviour. The absence of obvious joint induced instability suggests that the material can be treated as mechanical continuum at the scale of the slopes present (>100 m high). This does not exclude the possibility of future kinematic failures, particularly near faults or more heavily jointed zones or future failures resulting from the propagation of joints developed specifically in response to horizontal unloading.

It may be that in such relatively massive rock the material should be treated as an intact but transversely isotropic rock for continuum modelling purposes. This would allow an orientation strength bias to be characterised for analysis purposes without requiring the

complicating consideration of the discontinuities, which are irrelevant where the material behaves as an intact material.

The Talysarn failure does not appear to have occurred in response to the differences in strength based on an orientation bias. Furthermore, the numerical analyses undertaken confirm that unrealistically low compressive strengths are required to result in failure. The postulated mechanism of failure, due to reliance on tension and the gradual concentration of stress at fewer and fewer rock bridges, is itself not necessarily a consequence of one orientation being weaker in tension or compression than any other. However, the opening or creation of near vertical unloading joints in response to quarry excavation are undoubtedly promoted by the pervasive near vertical cleavage. This will make some slope orientations more prone to such failures than others.

9.8 Closing comments

The fundamental problem remains of trying to apply a single failure criterion to predict behaviour from to a tensile to compressive stress regime for rock masses of differing strengths, degrees of strength anisotropy and discontinuity properties. It may be that different failure criteria lend themselves more to specific applications or rock types than being truly ubiquitous. This challenge is highlighted by Figure 9-4, showing a particularly blocky outcrop of dolerite contrasting with a well cleaved slate.

Figure 9-4 Titterstone Clee Hill dolerite and the Llanberis Slates Formation.

10 References

Alejano L R, González J, Muralha J (2012) *Comparison of Different Techniques of Tilt Testing and Basic Friction Angle Variability Assessment*. Rock Mechanics and Rock Engineering 45:1023-1035.

APEM (2019) *Dorothea Quarry Bathymetric Survey*, Report number P00003764, July 2019 APEM Ltd Stockport.

Barton N, Quandros E (2015) *Anisotropy is Everywhere, to See, to Measure, and to Model*. Rock Mechanics and Rock Engineering 48:1323-1339.

Barton N R (2014) *Shear strength of rock, rock joints and rock masses - problems and some solutions*. Keynote lecture, Eurorock, Vigo.

Barton N R (2015) *Forty Years with the Q-system - Lessons and Developments*. Hong Kong, IoM3.

Barton N, Shen B (2018) *Extension Strain and Rock Strength Limits for Deep Tunnels, Cliffs, Mountain Walls and the Highest Mountains*. Rock Mechanics and Rock Engineering 51:3945-3962.

Bertuzzi R (2019) *Revisiting rock mass classification to estimate rock mass properties*. Journal of Rock Mechanics and Geotechnical Engineering 11:494-510.

Bertuzzi R, Douglas K, Mostyn G (2016) *Improving the GSI Hoek-Brown criterion relationship*. International Journal of Rock Mechanics and Mining Sciences 89:185-199.

BGS (1961) *British Regional Geology North Wales (Third edition)*. Her Majesty's Stationary Office, London.

BGS (1985) *England and Wales Sheet SH 55 SW Nantlle*. 1:10 000. BGS, Nottingham.

BGS (2015) *Nefyn and part of Caernarfon, England and Wales Sheet 118 and part of Sheet 105. Bedrock and Superficial Deposits*. 1:50 000. BGS Nottingham.

BGS (2019) *Geology of Britain Viewer*. http://mapapps.bgs.ac.uk/geologyofbritain/home.html [Accessed 7 December 2019].

BGS (2020) *Earthquakes around the British Isles in the last 50 days*. http://earthquakes.bgs.ac.uk/earthquakes/recent_uk_events.html [Accessed 20 July 2020].

BSI (2004) BS EN 1997-1:2004 +A1:2013 (Incorporating corrigendum February 2009) *Eurocode 7: Geotechnical design - Part 1: General rules*. BSI Standards Limited.

BSI (2015) BS 5930:2015 *Code of practice for ground investigations*. BSI Standards Limited.

BSI (2018) BS EN ISO 14689 *Geotechnical investigation and testing - Identification, description and classification of rock*. BSI Standards Limited.

Button E, Riedmüller G, Schubert W, Klima K, Medley E (2004) *Tunnelling in tectonic melanges - accommodating the impacts of geotechnical complexities and anisotropic rock mass fabrics*. Bulletin of Engineering Geology and the Environment 63:109-117.

Cai M (2010) *Practical Estimates of Tensile Strength and Hoek-Brown Strength Parameter m_i of Brittle Rocks*. Rock Mechanics and Rock Engineering 43:167-184.

CET (2019) *Report on Ground Investigation at Hunterston Power Station B for Workplace Solutions / Engie* (version 1).

Cohen K M, Finney S C, Gibbard P L, Fan J -X (2020) *ICS International Chronostratigraphic Chart*. Episodes 36:199-204. [Online] Available at: http://www.stratigraphy.org/ICSchart/ChronostratChart2020-01.pdf [Accessed 20 May 2020].

Colak K, Unlu T (2004) *Effect of transverse anisotropy on the Hoek-Brown strength parameter 'm_i' for intact rocks*. international Journal of Rock Mechanics and Mining Sciences 41:1045-1052.

Compston W, Wright A E, Toghill P (2002) *Dating the Late Precambrian volcanicity in England and Wales*. Journal of the Geological Society of London 159:323-339.

Connor-Langford J, Diederichs M S (2015) *Quantifying uncertainty in Hoek-Brown intact strength envelopes*. International Journal of Rock Mechanics and Mining Sciences 74:91-102.

Davies M (2020) *An investigation into the geology between Dorothea Lake and Cym Silyn, North Wales: implications for ground engineering*. Unpublished MSci Thesis for The University of Birmingham.

Douglas T H (1984) *Discussion on 'Comparison between real and predicted geology in tunnels : examples from recent cases' by G. West*. Quarterly Journal of Engineering Geology 17:165-166.

Douglas T H, Richards L R, Arthur L J (1983) *Trial excavation for underground caverns at Dinorwig power station*. Géotechniquie, 33(4):407-431.

DRC (2012) *Instruction Manual Geohammer*. https://www.drcitalia.it/wp-content/uploads/areadownload_ENG/Geohammer/Manual/DOC_GEOHAMMER_manual032015_ENG.pdf [Accessed 20 December 2020].

Eberhardt E (2012) *The Hoek-Brown Criterion*. Rock Mechanics and Rock Engineering 45:981-988.

Essex R J (2007). *Geotechnical Baseline Reports for Construction (second edition)*. American Society of Civil Engineers. Virginia.

Forshaw M J (2019) *A Sedimentology and Provenance Study of Lower to Mid-Cambrian Turbidites within the Llanberis State Formation, NW Wales*. Unpublished MSci Thesis for The University of Birmingham.

Fortey R A, Harper R A, Ingham J K, Owen A W, Parkes M A, Rushton A W A, Woodcock N H (2000) *A revised correlation of Ordovician Rocks in the British Isles Special Report 24*. The Geological Society of London.

Fortsakis P, Nikas K, Marinos V, Marinos P (2012) *Anisotropic behaviour of stratified rock masses in tunnelling*. Engineering Geology 141:74-83.

Griffith A A (1921) *The Phenomena of Rupture and Flow in Solids*. Philosophical Transactions of the Royal Society of London 221:163-198.

Ground Engineering (2018) *Ground Engineering*. [Online]

Available at: https://www.geplus.co.uk/news/sse-wins-108m-in-appeal-over-glendoe-tunnel-collapse-12-04-2018/ [Accessed 13 December 2020].

Hencher S R (2019) *The Glendoe Tunnel Collapse, Scotland*. Rock Mechanics and Rock Engineering 52:4033-4055.

Hoek E (1990) *Estimating Mohr-Coulomb Friction and Cohesion Values from the Hoek-Brown Failure Criterion*. International Journal of Rock Mechanics, Mining Science and Geomechanics 27(3):227-229.

Hoek E (1998) *Reliability of Hoek-Brown Estimates of Rock Mass Properties and their Impact on Design*. International Journal of Rock Mechanics and Mining Science 35(1):63-68.

Hoek E (1999) *Putting numbers to geology - an engineer's viewpoint*. Quarterly Journal of Engineering Geology 32:1-19.

Hoek E (2001) *Big tunnels in bad rock (The Thirty-Sixth Karl Terzaghi Lecture)*. Journal of Geotechnical and Geoenvironmental Engineering 127(9):726-740.

Hoek E (2006) *Practical Rock Engineering*. [Online]

Available at: https://www.rocscience.com/learning/hoeks-corner/course-notes-books [Accessed 15 November 2019].

Hoek E, Brown E T (1980) *Underground Excavations in Rock*. London: The Institution of Mining and Metallurgy.

Hoek E, Brown E T (1997) *Practical estimates of rock mass strength*. International Journal of Rock Mechanics and Mining Sciences 34(8):1165-1186.

Hoek E, Brown E T (2018) *The Hoek-Brown failure criterion and GSI - 2018 edition*. Journal of Rock Mechanics and Geotechnical Engineering 11(3):445-463.

Hoek E, Carranza-Torres C, Corkum B (2002) *Hoek-Brown 2002 edition*. In: R. Hammah, W. Bawden, J. Curran and M. Telesnicki, eds. Mining and tunnelling innovation and opportunity, proceedings of the 5th North American rock mechanics

symposium and 17th tunnelling association of Canada conference. Toronto, Canada: University of Toronto 267-273.

Hoek E, Carter T G, Diederichs M S (2013) *Quantification of the Geological Strength Index Chart*. 47th US Rock Mechanics / Geomechanics Symposium, San Francisco.

Hoek E, Diederichs M S (2006) *Empirical estimation of rock mass modulus*. International Journal of Rock Mechanics and Mining Sciences 43(2):203-215.

Hoek E, Marinos P (2000) *Predicting tunnel squeezing problems in weak heterogeneous rock masses, Part 1: Estimating rock mass strength*. Tunnels and Tunnelling International 1-21.

Hoek E, Palmeiri A (1998) *Geotechnical risks on large civil engineering projects, Keynote address for Theme 1*. International Association of Engineering Geologists Congress, Vancouver, Canada. Vancouver.

Howells M F, Smith M (1997) *Geology of the country around Snowdon*. The Stationary Office, London.

Hudson J A (1989) *Rock Mechanics Principles in Engineering Practice*, Butterworths.

Hudson J A, Harrison J P (1997) *Engineering rock mechanics and introduction to the principles*. Elsevier, Oxford.

IHA (2021) *International Hydropower Association*. [Online]

Available at: https://www.hydropower.org/country-profiles/united-kingdom [Accessed 10 July 2021.

Jorda-Bordehore L, Herrera R, (2018) *Rapid field test for shear strength characterization pf dacite at Cerro Rico de Potosi (Bolivia): tilt test with Schmidt hammer and compass-clinometer*, Bulletin of Engineering Geology and the Environment 77:867-875.

King C (2016), *A revised correlation of Tertiary rocks in the British Isles and adjacent areas of NW Europe Special Report Number 27*. The Geological Society of London, Bath.

Kirton S R, Donato J A (1985) *Some buried Tertiary dykes of Britain and surrounding waters deduced by magnetic modelling and seismic reflection methods*. Journal of the Geological Society of London 142:1047-1057.

Lapworth C (1879) *On the Tripartite Classification of the Lower Palaeozoic Rocks*. The Geological Magazine 6(1):1-15.

Lee Y-K, Pietruszczak S (2017) *Analytical representation of Mohr failure envelope approximating the generalised Hoek-Brown failure criterion*. International Journal of Rock Mechanics and Mining Sciences 100:90-99.

Marinos P G, Marinos V, Hoek E (2007) *The Geological Strength Index (GSI): A characterisation tool for assessing engineering properties of rock masses*. In: Romana, Perucho and Olalla, eds. Underground works under special conditions. Taylor and Francis 13-21.

Marinos P, Hoek E (2000) *GSI - a geologically friendly tool for rock mass strength*. In: Proceedings GeoEng 2000, International conference on geotechnical and geological engineering. Melbourne, Australia: Technomic Publishing Co, 1422-1440.

Marinos V, Carter T G (2018) *Maintaining geological reality in application of GSI for design of engineering structures in rock*. Engineering Geology 239:282-297.

Marinos V, Marinos P, Hoek E (2005) *The geological strength index: applications and limitations*. Bulletin of Engineering Geology and the Environment 55-65.

Melkoumian N, Priest S D, Hunt S P (2009) Further Development of the Three-Dimensional Hoek-Brown Yield Criterion. Rock Mechanics and Rock Engineering 42:835-847.

Mohammadi H, Tavakoli H (2015) *A study of the behaviour of brittle rocks subjected to confining stress based on the Mohr-Coulomb failure criterion*. Geomechanics and Geoengineering: An International Journal 10(1):57-67.

Morris T O, Fearnside W G (1926) *The Stratigraphy and Structure of the Cambrian Slate-Belt of Nantlle (Carnarvonshire)*. Journal of the Geological Society of London 82:250-303.

Muehlberger W R (1961) *Conjugate Joint Sets of Small Dihedral Angle*. The Journal of Geology, 69(2):211-219.

Neuffer D P, Schultz R A (2019) *Mechanisms of slope failure in Valles Marineris, Mars*. Quarterly Journal of Engineering Geology and Hydrogeology 39:227-240.

Nield T (2007) *Supercontinent*. Granta Publications, London.

Oldroyd D R (1990) *The Highlands Controversy Constructing Geological Knowledge through Fieldwork in Nineteenth-Century Britain*. The University of Chicago Press, Chicago.

Owens W H (1984) *The calculation of a best-fit ellipsoid from elliptical sections on arbitrarily orientated planes*. Journal of Structural Geology 6(5):571-578.

Palmstrom A (2005) *Measurement of and correlation between block size and rock quality designation (RQD)*. Tunnelling and Underground Space Technology 20:362-377.

Pérez-Rey I, Alejano L R, Muralha J (2019) *Experimental Study of Factors Controlling Tilt Test Results Performed on Saw-Cut Rock Joints*, ASTM Geotechnical Testing Journal 42(2):307-330.

Pine R J, Harrison J P (2003) *Rock mass properties for engineering design*. Quarterly Journal of Engineering Geology and Hydrogeology 36:5-16.

Pothier H D, Waldron J W F, Schofield D I, DuFrane S A (2015) *Peri-Gondwanan terrane interactions recorded in the Cambrian-Ordovician detrital zircon geochronology of North Wales*. Gondwana Research 28:987-1001.

Prasssetyo S H, Gutierrez M, Barton N (2017) *Nonlinear shear behaviour of rock joints using a linearized implementation of the Barton-Bandis model*. Journal of Rock Mechanics and Geotechnical Engineering 9:671-682.

Priest S D (2005) *Determination of Shear Strength and Three-dimensional Yield Strength for the Hoek-Brown Criterion*. Rock Mechanics and Rock Engineering 38(4):299-327.

Priest S D (2010) *Comparisons Between Selected Three-Dimensional Yield Criteria Applied to Rock*. Rock Mechanics and Rock Engineering 43(4):379-389.

Quantum Geotechnical (2015) *Glyn Rhonwy Pumped Storage Ground Investigation* Report Number G621/FR.

Ramamurthy T, Rao G V, Singh J (1993) *Engineering behaviour of phyllites*. Engineering Geology 33:209-225.

Reedman A J, Leveridge B E, Evans R B (1984) *The Arfon Group ('Arvonian') of North Wales*. Proceedings of the Geologists' Association 95(4):313-321.

Rees A J, Thomas A T, Lewis M, Hughes H E, Turner P (2014) *The Cambrian of SW Wales: Towards a United Avalonian Stratigraphy*. Geological Society of London, Memoirs 42:1-30.

Rocscience (2016) *Hoek's Corner: Intact rock sampling and testing*. [Online] Available at: https://www.rocscience.com/learning/hoeks-corner/lecture-series [Accessed 28 October 2019].

Rushton A W A, Brück P M, Molyneux S G, Williams M, Woodcock N H (2011) A *Revised Correlation of the Cambrian Rocks in the British Isles, Special Report Number 25*, The Geological Society of London, London.

Rushton A W A, Howells M F (1998) *Stratigraphic framework for the Ordovician of Snowdonia and the Lleyn Peninsula*, BGS Research Report RR/99/08, Keyworth, Nottingham: BGS.

Rushton A W A, Owen A W, Owens R M, Pringmore J K (2000) *British Cambrian to Ordovician Stratigraphy, Geological Conservation Review Series, No 18*. Joint Nature Conservation Committee, Peterborough.

Saeidi O, Rasouli V, Vaneghi R G, Gholami R (2014) *A modified failure criterion for transversely isotropic rocks*. Geoscience Frontiers 5:215-225.

Saeidi O, Vaneghi R G, Rasouli R, Gholami R (2013) *A modified empirical criterion for strength of transversely anisotropic rocks with metamorphic origin*. Bulletin of Engineering Geology and the Environment 72:257-296.

Saroglou H, Tsiambaos G (2008) *A modified Hoek-Brown failure criterion for anisotropic intact rock*. International Journal of Rock Mechanics and Mining Sciences 45:223-234.

Schofield D I, Evans J A, Millar I L, Wilby P R, Aspden J A (2008) *New U-Pb and Rb-Sr constraints on pre-Acadian tectonism in North Wales*. Journal of the Geological Society of London 165:891-894.

Schofield D I, Leslie A G, Wilby P R, Dartnall R, Waldron J W F, Kendall R S (2021) *Tectonic evolution of Anglesey and adjacent mainland North Wales*. Geological Society of London, London, Special Publications 503:371-390.

Schofield D I, Potter J, Barr A M, Horák J M, Millar I L, Longstaffe F J (2016) *Reappraising the Neoproterozoic 'East Avalonia' of southern Great Britain*. Gondwana Research 35:257-271.

Shen B, Shi J, Barton N (2020) *Graphic Examples of a Logical Nonlinear Strength Criterion for Intact Rock*. Rock Mechanics and Rock Engineering 53:71-75.

Singh M, Barton N (2019) *Highest Mountains Suggest Strong Curvature of Shear Strength Envelopes for Rock*. Proceedings of ISRM Conference Foz do Iguacu, Brazil.

Stimpson B (1981) *A Suggested Technique for Determining the Basic Friction Angle of Rock Surfaces Using Core*. International Journal of Rock Mechanics and Mining Sciences and Geomechanics Abstracts 19(1):63-65.

Thomas M E, Petford N, Bromhead E N (2019) *Volcanic rock-mass properties from Snowdonia and Tenerife: implications for volcano edifice strength*. Journal of the Geological Society of London 161:939-946.

Tien Y M, Kuo M C, Juang C H (2006) *An experimental investigation of the failure mechanism of simulated transversely isotropic rocks*. International Journal of Rock Mechanics and Mining Sciences 43:1163-1181.

Trewin N H, Thirlwall M F (2002) *Old Red Sandstone*. In: N. H. Trewin, ed. The Geology of Scotland. The Geological Society of London, London 213-249.

van der Pluijm B A, Marshak S (1997) *Earth Structure: An Introduction to Structural Geology and Tectonics*. McGraw-Hill.

UNESCO (2021) *The Slate Landscape of Northwest Wales*. [Online] Available at: https://whc.unesco.org/en/list/1633/ [Accessed 30 July 2021].

West G (1983) *Comparisons between real and predicted geology in tunnels: examples from recent cases*. Quarterly Journal of Engineering Geology and Hydrogeology 16:113-126.

West G, Ewan V J (1981) *Site investigation and construction of the Dinorwic diversion tunnel*. TRRL Report LR 984, Transport and Road Research Laboratory, Crowthorn.

Woodcock R, Strachan R (2002) *Geological History of Britain and Ireland*. Blackwell Publishing.

Wood D S (1974) *Current views of the development of slaty cleavage*. Annual Review of Earth and Planetary Sciences 2:369-401.

Zhang Q, Zhu H, Zhang L (2013) *Modification of a generalised three-dimensional Hoek-Brown strength criterion*. International Journal of Rock Mechanics and Mining Sciences 59:80-96.

Appendix A. Rock strengths from ISO 14689:2017

Strength term	Identification by hand test	UCS (MPa)
Extremely weak	Scratched by thumbnail, gravel sized lumps can be crushed between finger and thumb.	0.6 to 1.0
Very weak	Scratched by thumbnail, lumps can be broken by heavy hand pressure, can be peeled easily by a pocket knife, crumbles under firm blows with point of a geological hammer.	1 to 5
Weak	Thin slabs, corners or edges can be broken off with hand pressure, can be peeled by a pocket knife with difficulty, easily scratched by pocket knife, shallow indentations made by firm blow with point of geological hammer.	5 to 12.5
Moderately weak	Thin slabs, corners or edges can be broken off with heavy hand pressure, can be scratched with difficulty by pocket knife, hand-held specimen can be broken with single firm blow of geological hammer.	12.5 to 25
Medium strong	Cannot be scraped or peeled with a pocket knife, specimen on a solid surface can be fractured with a single firm blow of geological hammer	25 to 50
Strong	Specimen requires more than one blow of geological hammer to fracture it.	50 to 100
Very strong	Specimen requires many blows of geological hammer to fracture it.	100 to 250
Extremely strong	Specimen can only be chipped with geological hammer.	> 250

Table A.1 Rock strength descriptions from ISO 14689:2017.

Appendix B. Published values of petrographic parameter m_i

	Hoek and Brown (1997)	Hoek (2006)	Bertuzzi et al. (2016)	Marinos and Carter (2018)
Sedimentary rocks				
Conglomerate	(22)	(21±3)	-	25-27 (not clayey)
Breccia	-	(19±5)	-	-
Sandstone	19	17±4	12	17-20 (medium quartz cemented)
	-	-	-	13-16 (medium)
Claystone	4	4±2	-	4-6
Shales	-	(6±2)	-	-
Marls	-	(7±2)	-	-
Siltstone	9	7±2	-	10-12
Greywackes	-	(18±3)	-	-
Chalk	7	7±2	-	7-9
Coal	(8-21)	-	8.06-18	-
Carbonate breccia	(20)	-	-	-
Sparitic limestone	(10)	(10±2)	-	-
Micritic limestone	8	(9±2)	-	-
Crystalline limestone	-	(12±3)	-	-
Unspecified limestone	-	-	14.9	-

	Hoek and Brown (1997)	Hoek (2006)	Bertuzzi et al. (2016)	Marinos and Carter (2018)
Dolomites	-	(9±3)	-	-
Unspecified carbonates	-	-	-	13-16
Gypsum	-	8±2	-	-
Metamorphic rocks				
Marble	9	9±3	-	-
Hornfels	(19)	(19±4)	39.1	17-20
Quartzite	24	20±3	9	17-20
	-	-	17-23	-
Metasandstone	-	(19±3)	-	-
Migmatite	(30)	(29±3)	-	-
Amphibolite	25-31	(26±6)	-	-
Mylonites	(6)	-	-	4-6
Gneiss	33	28±5	-	28-30 (quartz gneiss)
	-	-	-	25-27 (amphibolitic)
	-	-	-	13-16 (biotitic)
Schists	4-8	12±3	-	-
	-	-	-	10-12 (foliated)
	-	-	-	7-9 (strongly schistose)
Phyllites	(10)	(7±3)	8	10-12
	-	-	-	7-9 (schistose)

	Hoek and Brown (1997)	Hoek (2006)	Bertuzzi et al. (2016)	Marinos and Carter (2018)
Igneous rocks				
Granite	33	32±3	41.4	31-33
	-	-	25	-
Rhyolite	(16)	(25±5)	-	25-27
Obsidian	(19)	(19±3)	-	-
Granodiorite	(30)	(29±3)	-	28-30
Dacite	(17)	(25±3)	-	-
Diorite	(28)	(25±5)	-	28-30
Andesite	19	(25±5)	-	25-27
Gabbro	27	(27±3)	-	25-27
Dolerite	(28)	(16±5)	-	17-20
Basalt	(17)	(25±5)	-	25-27
Norite	22	(20±5)	-	-
Agglomerate	(20)	(19±3)	-	-
Extrusive breccia	(18)	(19±5)	-	-
Tuff	(15)	(13±5)	-	-
Massive sulphide	-	-	14	-
Peridotite	-	(25±5)	-	25-27
Serpentinite	-	-	-	13-16
Anhydrite	-	12±2	-	-

Table B.1 Published values of m_i.

(Values in parentheses are estimates.)

Appendix C. Barton's criterion for the Kelly Burn Sandstone

C.1 Schmidt hammer calibration to determine JCS

C.1.1 Background and samples tested

The testing described in this Appendix was on core samples provided by EDF Nuclear Generation Limited from a ground investigation at Hunterston B Nuclear Power Station, Ayrshire, Scotland.

Core samples were selected in 2019 as being the most complete of the material remaining after completion of laboratory testing and were stored by the author for subsequent testing during the winter of 2020/21. The cores were from the Kelly Burn Sandstone, which comprises a red, purple, or reddish brown occasionally conglomeritic sandstone (Figure C-1). The sandstone is part of the Old Red Sandstone of the Midland Valley, an upwards fining sequence of Devonian to Carboniferous age, which in Ayrshire is interpreted to record braided streams, alluvial fans, and large channel bar deposits (Trewin and Thirlwall, 2002).

Figure C-1 Photographs of typical core samples of Kelly Burn Sandstone.

C.1.2 UCS and density measurements

For unweathered joint surface JCS = σ_c. On this basis a comparison of Schmidt hammer results with UCS measurements was undertaken to calibrate a Schmidt hammer subsequently used for fieldwork. Ignoring two anomalous results of 1.54 and 156 MPa twenty-seven UCS tests on samples of 89 or 117 mm diameter gave a range of σ_c from 22.2 to 57.6 MPa (CET, 2019). Average UCS values of 44.4 MPa (standard deviation 9.23 MPa) and 42.8 MPa (standard deviation 7.15 MPa) were determined from the small and large diameter tests respectively. The mean of all tests was 43.9 MPa. It is suggested that a lower average UCS for the larger diameter samples is probably attributable to the larger volume of rock tested capturing greater aspects of rock weakness. The mean dry density of the sandstone reported from UCS tests was 2.32 Mg/m^3.

C.1.3 Schmidt hammer values

Of 312 Schmidt rebound values all were in the range of 24 to 55 N/mm^2 (or MPa). Disregarding the lowest half of the population (i.e. 156 tests), as required for the Barton criteria, the mean value of 44.4 MPa is remarkably close to the mean USC of 43.9 MPa. All tests were undertaken in the vertical orientation with the hammer acting directly downwards with the core placed on a concrete floor and held in place to prevent movement (Figure C-3). Tests were undertaken using an L Type DRC Geohammer with 0.735 Nm impact energy and were undertaken with reference to the manufacturer's instructions (DRC, 2012) with the notable exception of that the impact surface was a curved core surface, not a flat surface.

The upper 50% of test data from different core lengths (Table C.1) were used to determine the coefficient of variability (percentage standard deviation divided by the mean) (Figure C-2), with a value ≤5% indicating sufficient tests had been undertaken. The two core lengths not achieving a coefficient of variability of ≤5% did not show a clear trend towards 5%. Where ≤5% was achieved this was achieved after 11 tests, suggesting a minimum population of at least 22 tests was required during subsequent fieldwork to ensure variability was been captured.

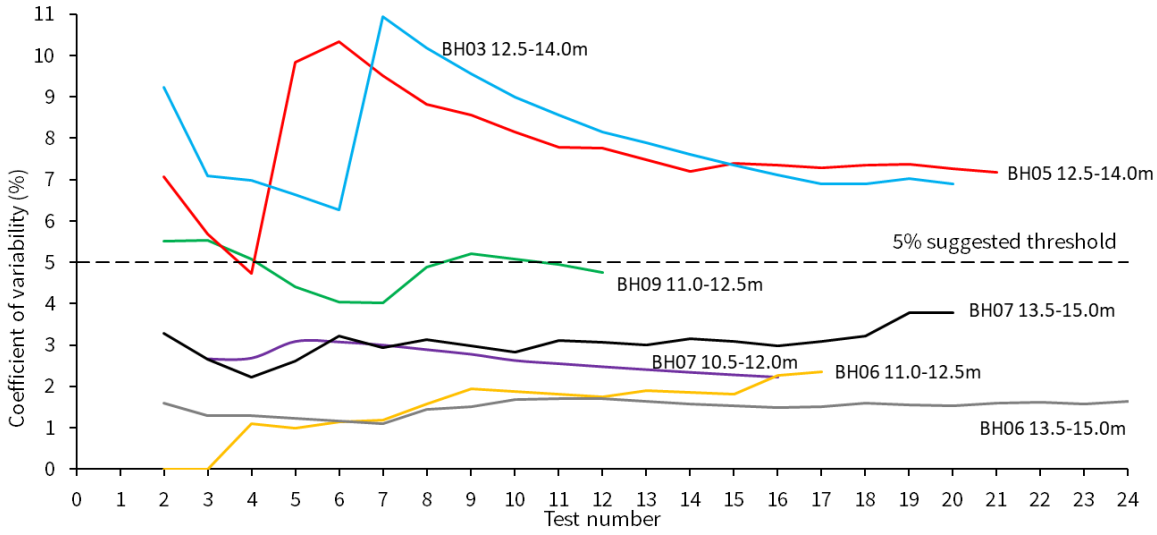

Figure C-2 Coefficient of variability for Schmidt results on core samples.

C.1.4 Test orientation bias

Consideration was given to the orientation of the test as a non-vertical test imparts less impact energy. This was tested with the core length showing the least variability in the tranche of vertical tests (BH07 from 10.5-12.0 m depth) being subjected to 50 further tests orientated vertically downwards, followed by a further 50 horizontal tests. Ignoring the lowest half of each population the mean vertical rebound value was 45.9 N/mm^2 and 46.7 N/mm^2 for the horizontal tests, a difference of <2% of the mean of the vertical tests. Mean values of horizontal and vertical tests are suggested to be sufficiently close to one another to remove the need for further consideration of the role of test orientation where horizontal or inclined below the horizontal.

C.1.5 Summary

The usual procedure for determining strength from a Schmidt rebound value requires correction for both test orientation and rock density (Figure C-4). Based on Figure C-4

and the regression curves provided with the manual (DRC, 2012) the suggested UCS values are far greater than actual measured values of UCS.

In the absence of formal calibration, the mean Schmidt rebound value for the highest 50% of values (44.4 MPa) is sufficiently close to the mean of all UCS measurements (43.9 MPa) to be considered adequate for estimating strength without further correction. For the range of rebound harnesses measured the Schmidt hammer therefore proved a reliable indicator of strength.

Based on an assessment of the coefficient of variability a minimum of 22 Schmidt hammer measurements are required to ensure that there is likely to be an acceptably small variability within the uppermost half of the population. This number may be unnecessarily high as the tests were undertaken on the curved surface of a core sample, rather than a planar joint surface, but served as a practical minimum for fieldwork purposes.

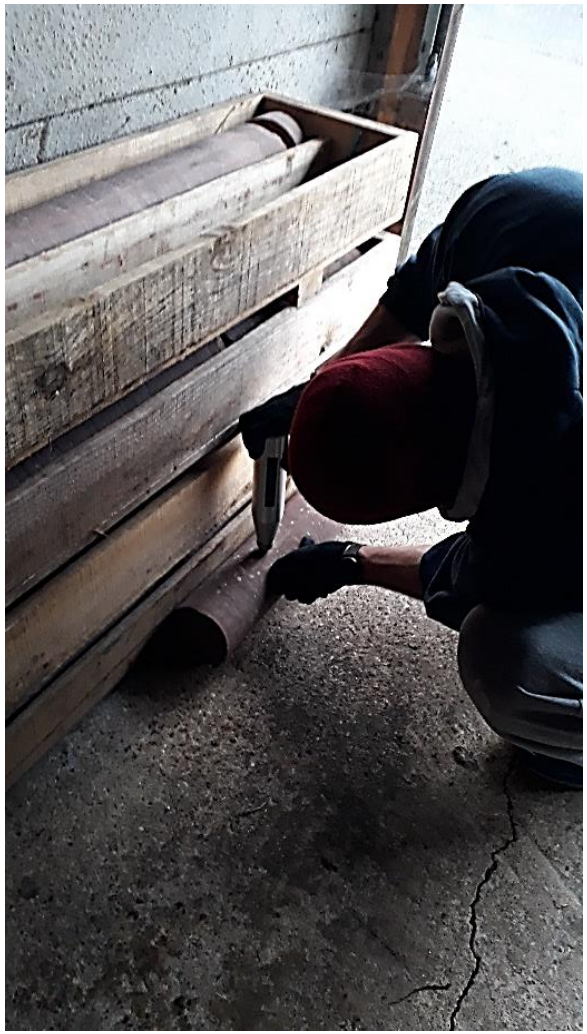

Figure C-3 Schmidt hammer testing of core material.

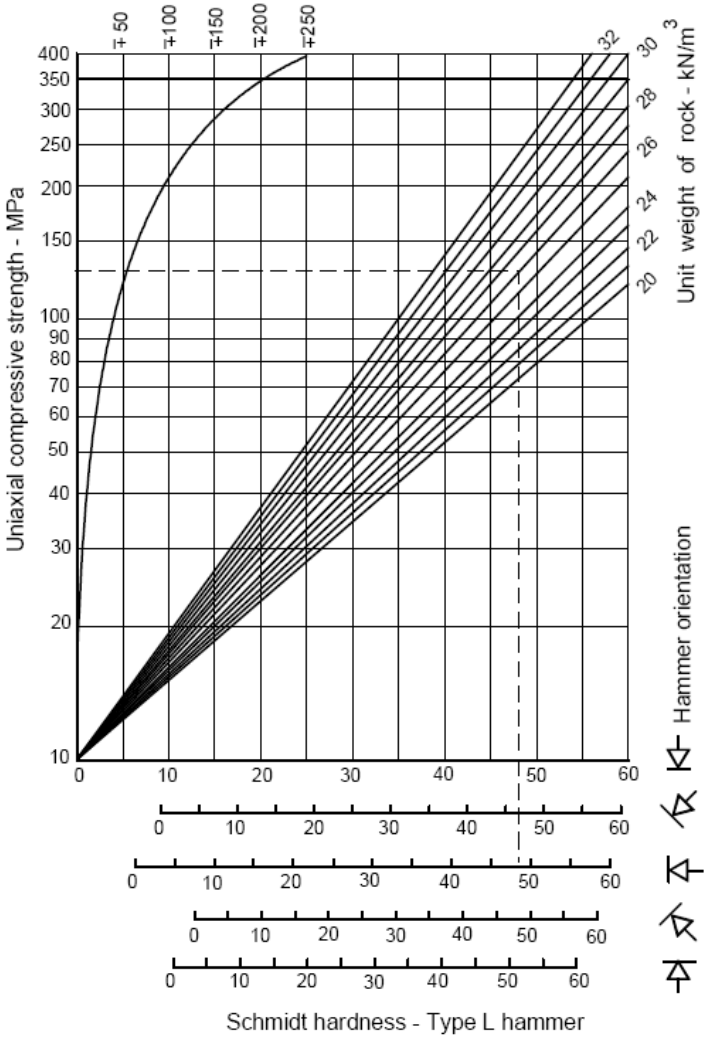

Figure C-4 UCS from Schmidt rebound hardness, orientation, and density.

BH02 12.5-14.0m	BH07 10.5-12.0m	BH07 10.5-12.0m	BH06 11.0-12.5m	BH09 11.0-12.5m	BH05 12.5-14.0m	BH06 13.5-15.0m	BH07 13.5-15.0m	BH03 12.5-14.0m
38, 37, 41, 42, 38, 37, 41, 37, 36, 40, 39, 40, 40, 45, 43, 44, 40, 41, 42, 40, 42, 42, 43, 43	36, 38, 36, 40, 41, 41, 40, 44, 44, 42, 42, 41, 45, 42, 38, 32, 42, 27, 44, 44, 43, 44, 44, 40, 44, 44, 40, 40, 44, 44, 41, 26, 28	45, 42, 43, 45, 46, 43, 44, 47, 47, 46, 44, 45, 45, 45, 44, 44, 44, 46, 46, 45, 46, 46, 38, 46, 45, 43, 46, 47, 44, 41, 42, 46, 45, 46, 42, 42, 48, 47, 45, 44, 44, 46, 43, 46, 44, 46, 44, 45, 39, 42, 42	25, 42, 45, 45, 45, 42, 34, 30, 37, 46, 45, 46, 46, 44, 47, 46, 45, 43, 45, 44, 46, 45, 41, 48, 44, 40, 40, 42, 43, 32, 37, 31	35, 40, 37, 36, 36, 37, 35, 38, 30, 39, 41, 41, 40, 40, 38, 31, 35, 34, 30, 28, 24, 29, 35, 35, 31	37, 37, 38, 42, 42, 40, 49, 36, 37, 29, 34, 43, 41, 31, 36, 39, 36, 40, 40, 38, 42, 40, 32, 37, 38, 38, 28, 31, 37, 35, 28, 29, 37, 38, 38, 36, 36, 24	40, 44, 38, 36, 45, 44, 45, 44, 42, 38, 40, 44, 44, 43, 45, 43, 45, 45, 44, 44, 44, 44, 45, 43, 44, 44, 41, 41, 42, 37, 43, 45, 40, 41, 26, 40, 44, 41, 43, 40	30, 42, 44, 44, 41, 43, 45, 46, 44, 39, 46, 40, 36, 45, 44, 41, 42, 41, 41, 36, 41, 43, 45, 42, 38, 43, 41, 44, 42, 40, 46, 41, 48, 46	36, 41, 41, 43, 41, 49, 40, 41, 41, 41, 44, 42, 42, 40, 41, 41, 41, 40, 41, 42, 55, 47, 47, 46, 47, 46, 48, 45, 47, 47, 47, 43, 35, 42, 44, 40, 39

Table C.1 Unweathered Schmidt hammer values on Kelly Burn Sandstone (N/mm^2).

Weathered Schmidt hammer results from a low wave cut cliff at NS 20182 47006
28, 31,38, 42, 24, 36, 41, 28, 22, 37, 45, 27, 28, 36, 42, 30, 32, 32, 43, 26, 26, 34, 34, 23, 28, 36, 39, 30, 20, 36, 40, 33, 24, 38, 25, 27, 26, 39, 40, 44, 20, 37, 30, 38, 32, 34, 35, 32, 30, 41, 30, 29, 29, 28, 30, 32, 28, 37, 36, 22, 32, 38, 34, 33, 30, 28, 29, 35, 28, 39, 34, 41, 30, 41, 39, 35, 28, 38, 40, 31, 31, 37, 42, 42, 30, 37, 41, 42, 26, 38, 40, 40, 26, 39, 42, 40, 30, 38, 41, 40, 35, 36, 31, 40, 31, 38, 40, 40, 38, 37, 42, 42, 31, 38, 40, 40, 31, 39,40, 40, 32, 39, 38, 39, 26, 39, 40, 32, 34, 39, 38, 37, 40, 31, 38, 40, 30, 34, 41, 30, 31, 34, 34, 34, 39, 31, 37, 40, 29, 36, 40, 31, 33, 40, 29, 35, 35, 31, 37, 37, 32, 36, 39, 32, 38, 35, 28, 39, 36, 32, 36, 37, 30, 35, 37, 26, 32, 36, 30, 39, 30, 30, 43, 34, 30, 35, 36, 34, 41, 41, 30, 43, 35, 33, 38, 33, 31, 38, 39, 33, 43, 35, 28, 37, 37, 37, 36, 32, 35, 36, 34, 36, 37, 32, 40, 38, 42, 34, 44, 42

Table C.2 Weathered Schmidt hammer results on Kelly Burn Sandstone (N/mm^2).

C.2 Barton's criterion: input parameters

C.2.1 JCS for the Kelly Burn Sandstone

A JCS of 44.4 MPa was adopted, the mean of the upper half of the Schmidt hammer tests.

C.2.2 JRC for the Kelly Burn Sandstone

A JRC was determined using a profile gauge on joint surfaces (Figure C-5) and comparison to Barton's JRC chart printed at the correct scale (Figure C-6). Drilling induced fractures were ignored. The range of values observed (Table C.3) gave a mean JRC of 10.2.

Figure C-5 Use of a profile gauge on a joint surface of Kelly Burn Sandstone.

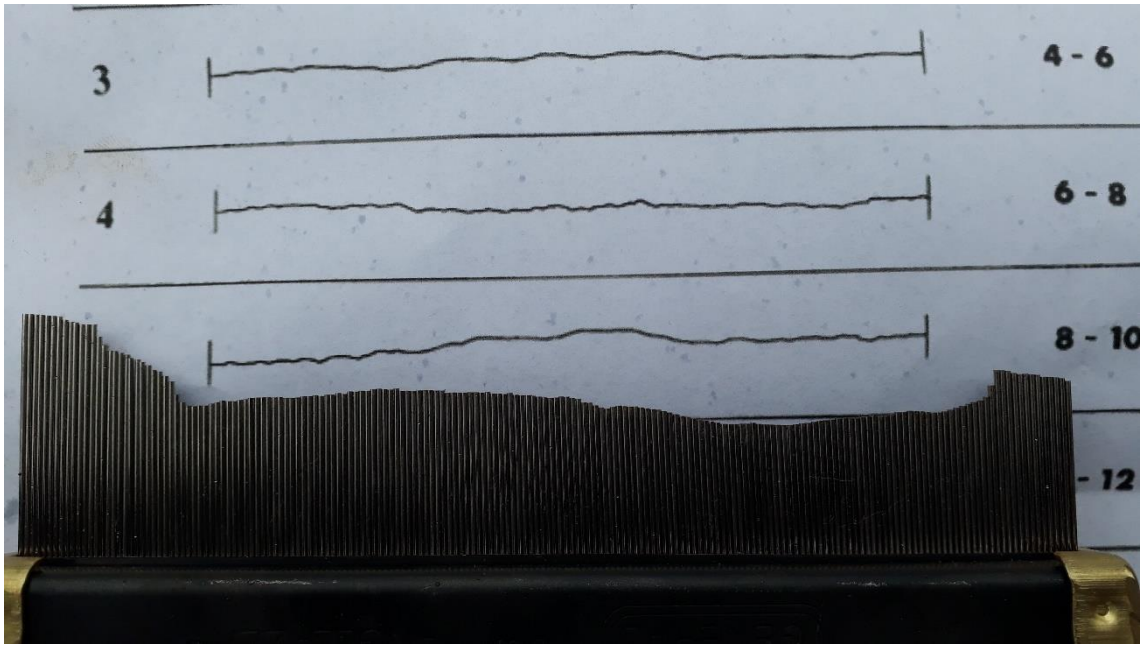

Figure C-6 Comparison of profile gauge to Barton's JRC chart.

Test number	Range of JRC values
1	8-10
2	12-14
3	14-16
4	10-12
5	6-8
6	10-12
7	8-10
8	12-14
9	8-10
10	8-10
11	8-10
12	12-14
13	8-10
14	12-14
15	10-12
16	6-8
17	10-12
18	4-6
Average	10.2

Table C.3 Values of JRC determined from cores of Kelly Burn Sandstone.

C.2.3 Bulk friction angle for the Kelly Burn Sandstone

Although Barton (2014) limits the self-weight tilt test to a maximum JRC = 9, several tilt tests gave a mean angle for the onset of sliding (α) of 35.5° (Table C.4). Tests were undertaken using an improvised arrangement of cores within a core box with the onset of sliding observed by a clinometer mounted on one of the lower cores (Figure C-7). The sliding core, labelled A. in Figure C-7, was placed on the lower cores after the end of the core box had been elevated to the desired test angle. The core box was sufficiently long to allow accurate changes in tilt one degree at a time. Clinometer measurements along the core box while elevated proved inaccurate as there was a perceptible sag in the part filled wooden core box, hence measurements on the core itself. The test set up was generally as described by Stimpson (1981) and Alejano et al. (2012). For an average α = 35.5° (Table C.4) a value of φ_b = 31.7° was determined using the relationship given by Alejano et al. (2012) (Equation 7.4).

Reference of sliding (top) core	Angle of tilt at which sliding occurred (α)
BH07 10.5-12.0m depth sample A	36°
BH07 10.5-12.0m depth sample B	35°
BH09 11.0-12.5m depth sample A	35°
BH09 11.0-12.5m depth sample B	35°
BH09 11.0-12.5m depth sample C	35°
BH09 11.0-12.5m depth sample D	35°
BH09 11.0-12.5m depth sample E	35°
BH05 12.5-14.0m depth sample A	35°
BH05 12.5-14.0m depth sample B	36°
BH05 12.5-14.0m depth sample C	36°
BH05 12.5-14.0m depth sample D	36°
BH05 12.5-14.0m depth sample E	38°
BH06 13.5-15.0m depth sample A	36°
BH06 13.5-15.0m depth sample B	35°
BH06 13.5-15.0m depth sample C	35°
BH06 13.5-15.0m depth sample D	35°
BH06 13.5-15.0m depth sample E	35°
Average	35.5°

Table C.4 Tilt test results on Kelly Burn Sandstone cores.

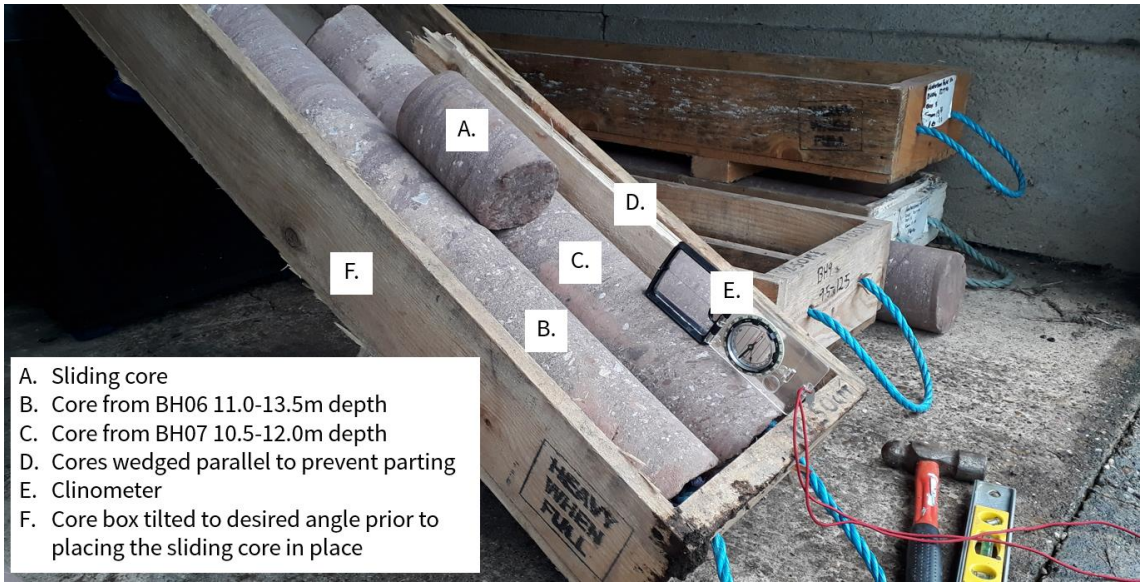

Figure C-7 Tilt test set up for determining φ_b on core material.

C.3 Barton's strength envelope for the Kelly Burn Sandstone

Using the values of JCS, JRC and φ_r described above strength envelopes for the Kelly Burn Sandstone are presented as Figure C-8 up to a value of $\sigma_n = \sigma_c$; a value associated with the ability of failure to propagate through intact rock. The two envelopes shown capture the upper and lower bound values of ϕ_r, based on the range of values of ϕ_b measured from different types of sliding test (Table 7.1).

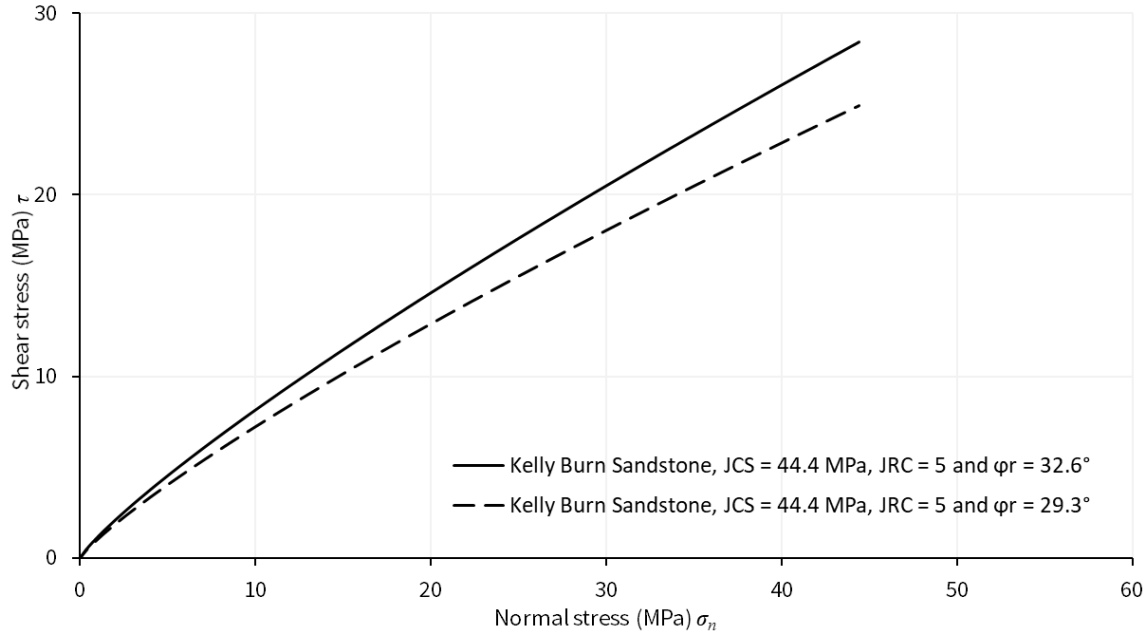

Figure C-8 Kelly Burn Sandstone: shear strength envelopes.

C.4 Shear strength parameters for the Kelly Burn Sandstone

Instantaneous friction angles (φ_i) and cohesion (c_i) were determined from the strength envelopes provided in Figure C-8 and are presented as Table C.5 using the approach shown in Figure C-9 and Figure C-10 respectively.

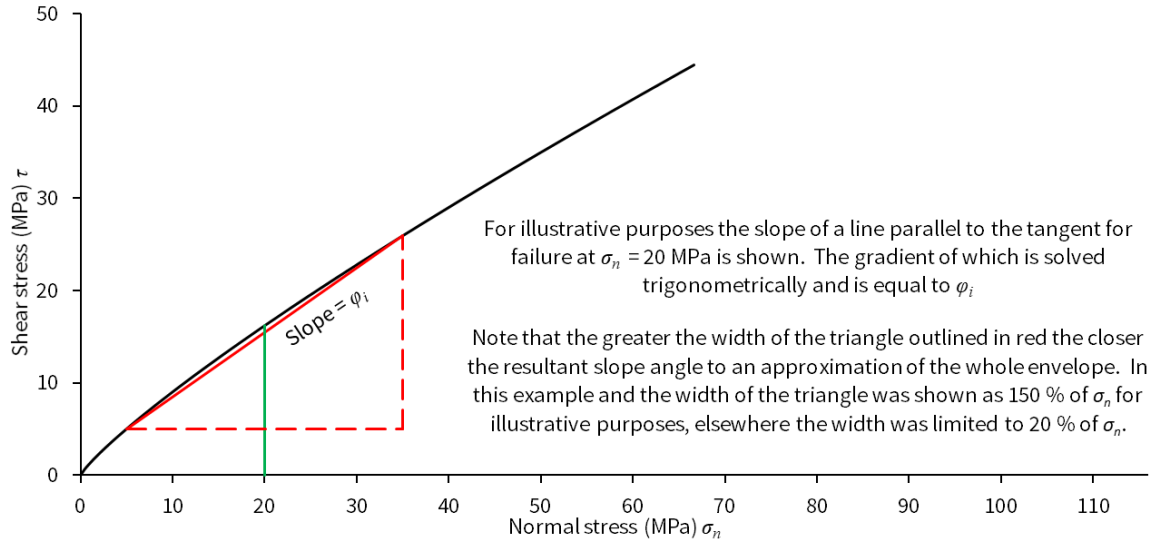

Figure C-9 Graphical representation of the method used to determine φ_i.

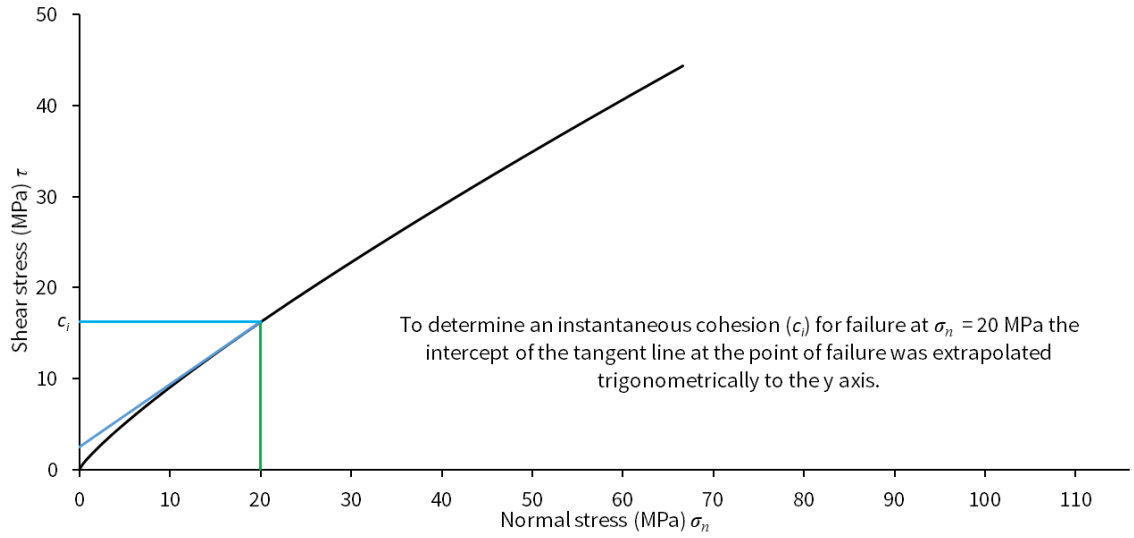

Figure C-10 Graphical representation of the method used to determine c_i.

	Lower bound ϕ_r = 29.3°			Upper bound ϕ_r = 32.6°		
σ_n	τ	ϕ_i	c_i	τ	ϕ_i	c_i
1 MPa	1.0 MPa	41.3°	0.16 MPa	1.2 MPa	44.6°	0.18 MPa
5 MPa	4.0 MPa	34.3°	0.64 MPa	4.5 MPa	37.5°	0.70 MPa
10 MPa	7.2 MPa	31.2°	1.18 MPa	8.2 MPa	34.5°	1.29 MPa
15 MPa	10.2 MPa	29.4°	1.69 MPa	11.5 MPa	32.7°	1.83 MPa
20 MPa	12.9 MPa	28.2°	2.19 MPa	14.6 MPa	31.5°	2.37 MPa
25 MPa	15.5 MPa	27.2°	2.67 MPa	17.6 MPa	30.5°	2.89 MPa
30 MPa	18.0 MPa	26.4°	3.15 MPa	20.5 MPa	29.7°	3.40 MPa
35 MPa	20.5 MPa	25.7°	3.63 MPa	23.3 MPa	29.0°	3.90 MPa
40 MPa	22.9 MPa	25.1°	4.10 MPa	26.0 MPa	28.4°	4.40 MPa

Table C.5 Kelly Burn Sandstone: Instantaneous shear strength parameters.

Appendix D. Parametric study of slope failure

D.1 Purpose

Numerical simulations were undertaken to assess the extent to which Generalised Hoek-Brown parameters can be used to explain the failure of a quarry wall by an iterative process of numerical simulations. Failure of the rock mass occurs when restoring forces equal disturbing forces along a rupture surface, i.e. a factor of safety equal to 1.0. Simulating a calculated factor of safety of unity gives a possible combination of parameters and geometry with the potential to cause failure. This was achieved by numerical simulation of a two-dimensional slice through one of the deepest parts of Dorothea Lake. The cross section used for analysis (Figure D-1) was prepared based on joining bathymetric (APEM, 2019) and LiDAR (pers. comm M. Billingham, 2020) survey data along the line of section (Figure D-2) with the offset <150 m and >310 m taken to be level ground, i.e ignoring the smaller quarry (Dorothea South) to the southwest and the opposite northeast wall of the quarry.

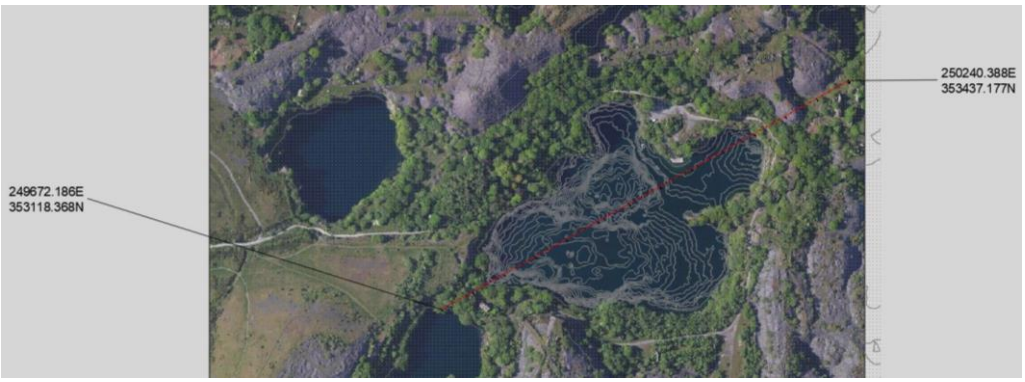

Figure D-1 Line of section used in the back analyses, courtesy of Mark Whatman.

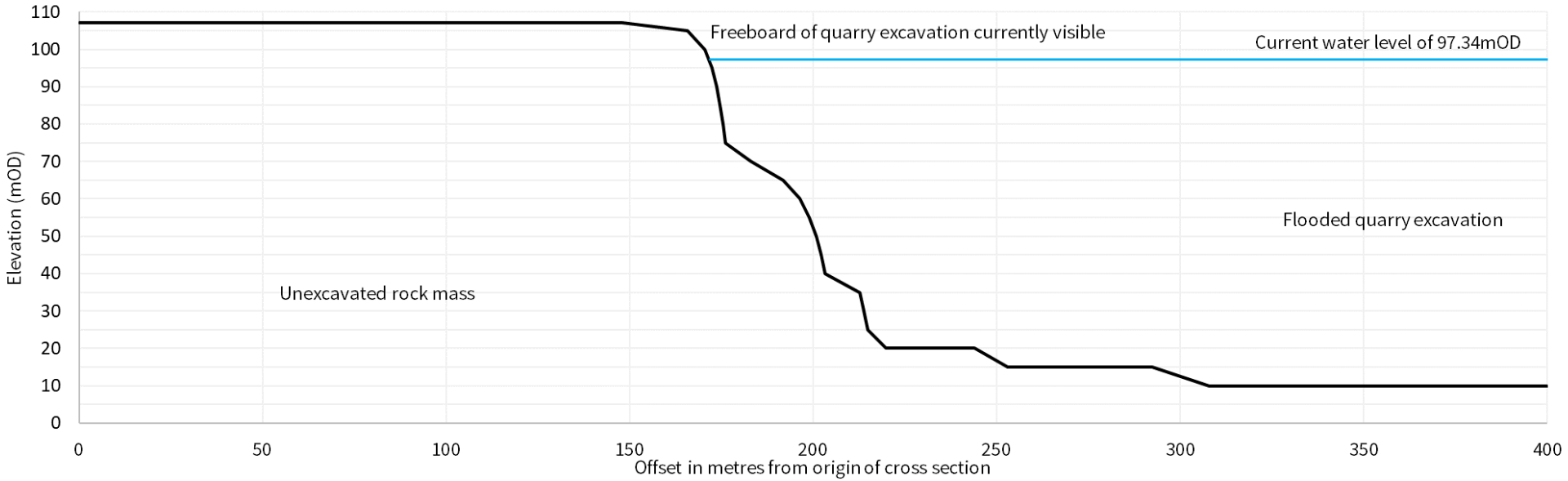

Figure D-2 Cross section used in the analyses process.

D.2 Analysis details: Settings and stages of analysis

Numerical analyses were undertaken using Itasca's FLAC 7.00.411 software with a static vertical gravity of g = 9.81 m/s^2 and model boundaries set an appropriate distance from the rock slope to negate proximity effects. The grid used in the analyses (Figure D-3) obeyed requirements for aspect ratios required by the software and the density of the grid reduced away from the rockface exposed by excavation to reduce run time to between 20 and 90 minutes for each simulation. The analyses undertaken comprised the following stages:

i. Establish the initial vertical and horizontal stress condition due to self-weight alone for horizontal ground at +107.1 mOD (Figure D-3).

ii. Reset calculated displacements to zero (Figure D-4).

iii. Excavate to +100 mOD and recalculate stress distribution (Figure D-5).

iv. Excavate to +95 mOD and recalculate stress distribution (Figure D-6).

v. Excavate to +90 mOD and recalculate stress distribution (Figure D-7).

vi. Excavate to +85 mOD and recalculate stress distribution (Figure D-8).

vii. Excavate to +80 mOD and recalculate stress distribution (Figure D-9).

viii. Excavate to +75 mOD and recalculate stress distribution (Figure D-10).

ix. Excavate to +70 mOD and recalculate stress distribution (Figure D-11).

x. Excavate to +65 mOD and recalculate stress distribution (Figure D-12).

xi. Excavate to +60 mOD and recalculate stress distribution (Figure D-13).

xii. Excavate to +55 mOD and recalculate stress distribution (Figure D-14).

xiii. Excavate to +50 mOD and recalculate stress distribution (Figure D-15).

xiv. Excavate to +45 mOD and recalculate stress distribution (Figure D-16).

xv. Excavate to +40 mOD and recalculate stress distribution (Figure D-17).

xvi. Excavate to +35 mOD and recalculate stress distribution (Figure D-18).

xvii. Excavate to +30 mOD and recalculate stress distribution (Figure D-19).

xviii. Excavate to +25 mOD and recalculate stress distribution (Figure D-20).

xix. Excavate to +20 mOD and recalculate stress distribution (Figure D-21).

xx. Excavate to +15 mOD and recalculate stress distribution (Figure D-22).

xxi. Excavate to +10 mOD and recalculate stress distribution (Figure D-23).

xxii. Calculate the factor of safety against failure.

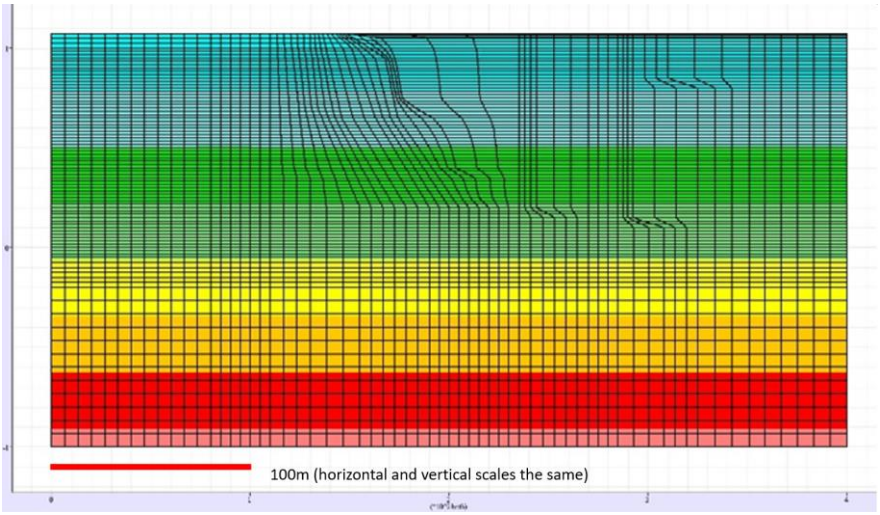

Figure D-3 Calculation of vertical stress from self-weight of the rock mass alone.

Figure D-4
Calculated settlement from elastic settlement of model alone.

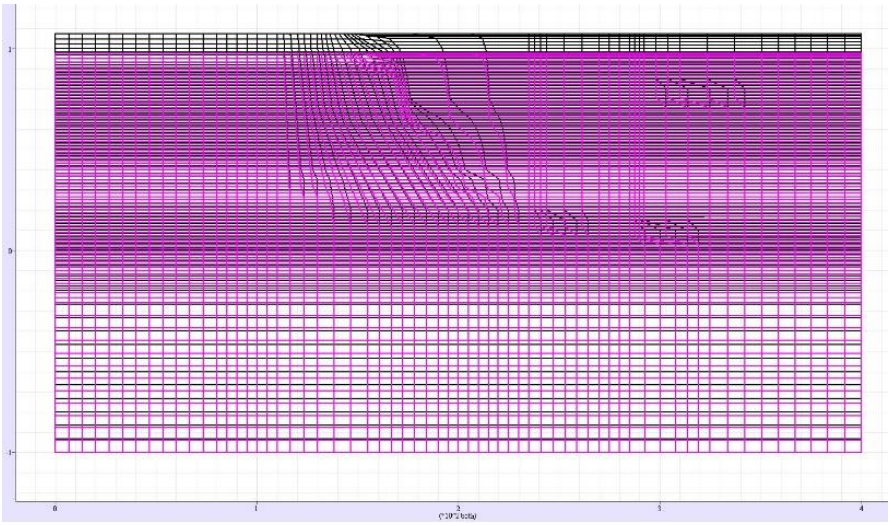

Figure D-5
Excavation to 100 mOD following the quarry profile.

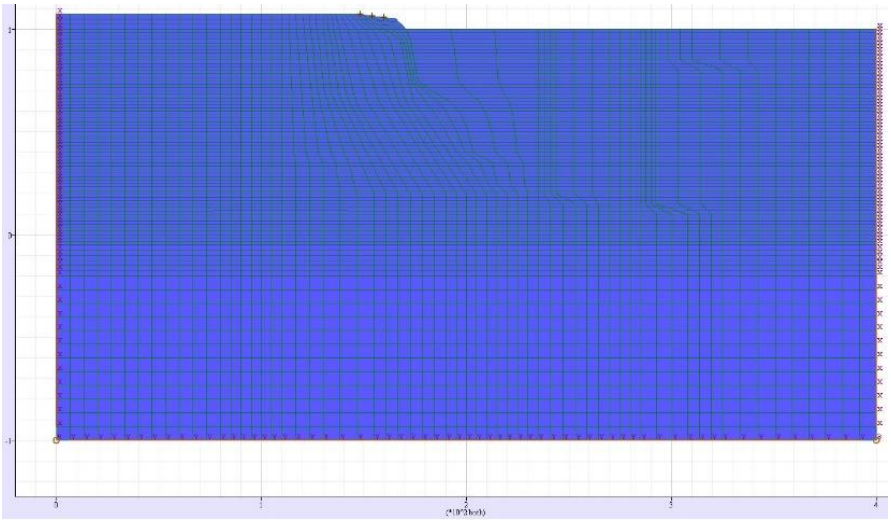

Figure D-6
Excavation to 95 mOD following the quarry profile.

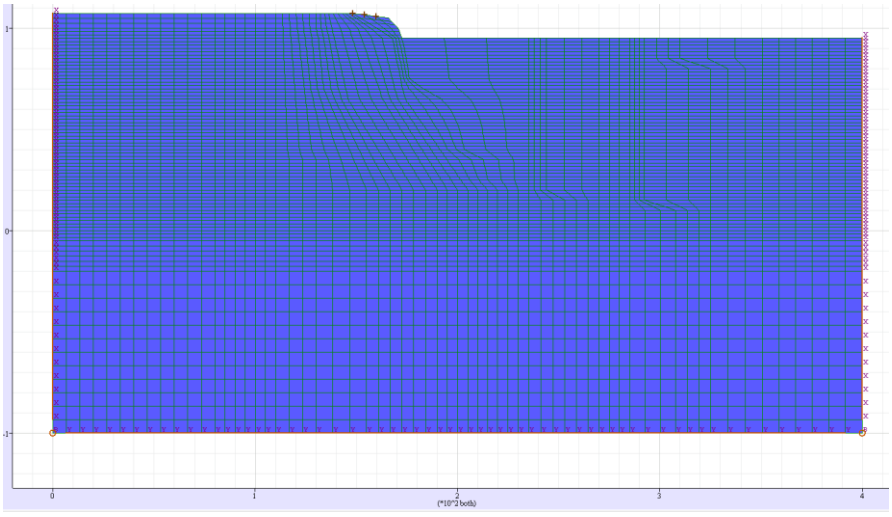

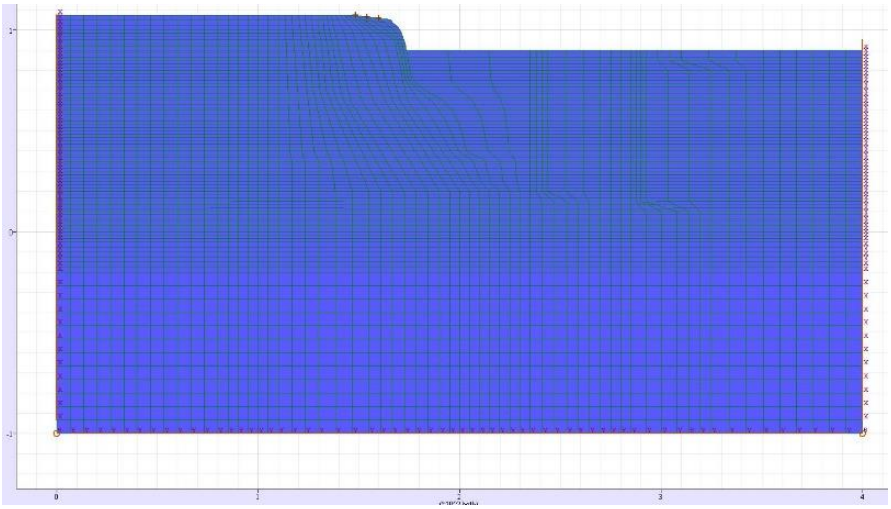

Figure D-7 Excavation to 90 mOD following the quarry profile.

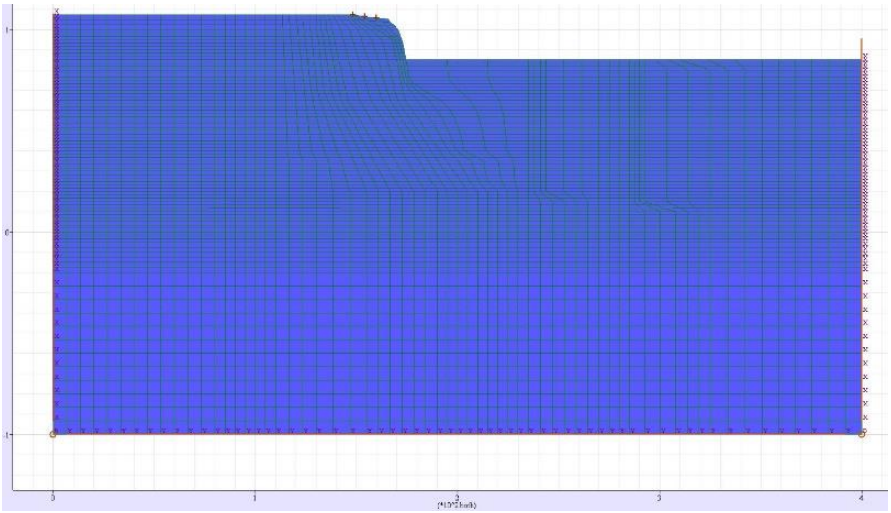

Figure D-8 Excavation to 85 mOD following the quarry profile.

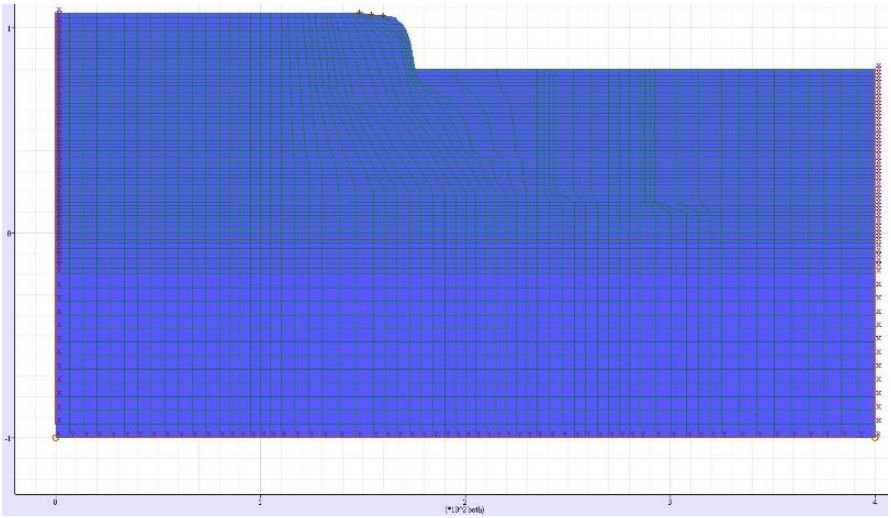

Figure D-9 Excavation to 80 mOD following the quarry profile.

Figure D-10 Excavation to 75 mOD following the quarry profile.

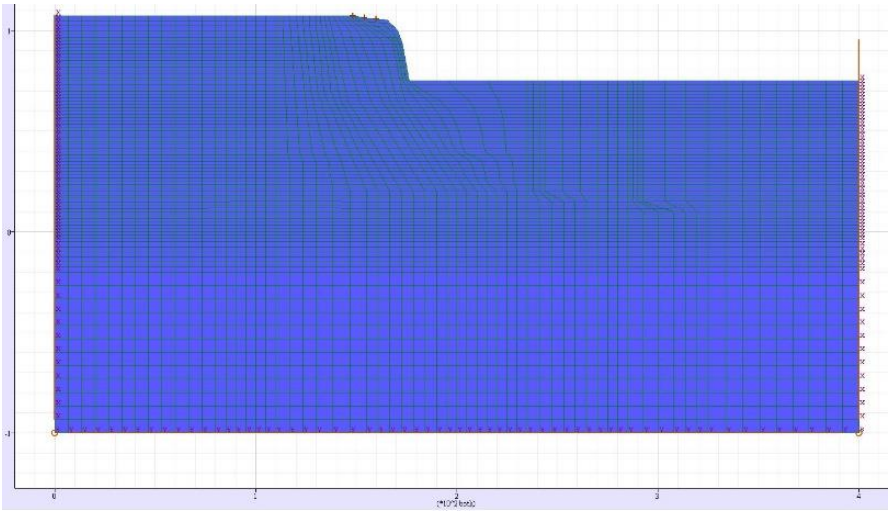

Figure D-11 Excavation to 70 mOD following the quarry profile.

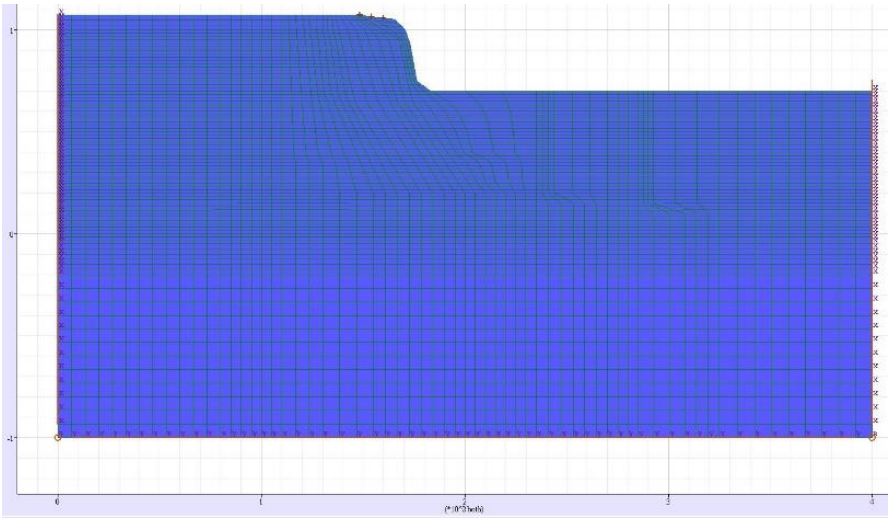

Figure D-12 Excavation to 65 mOD following the quarry profile.

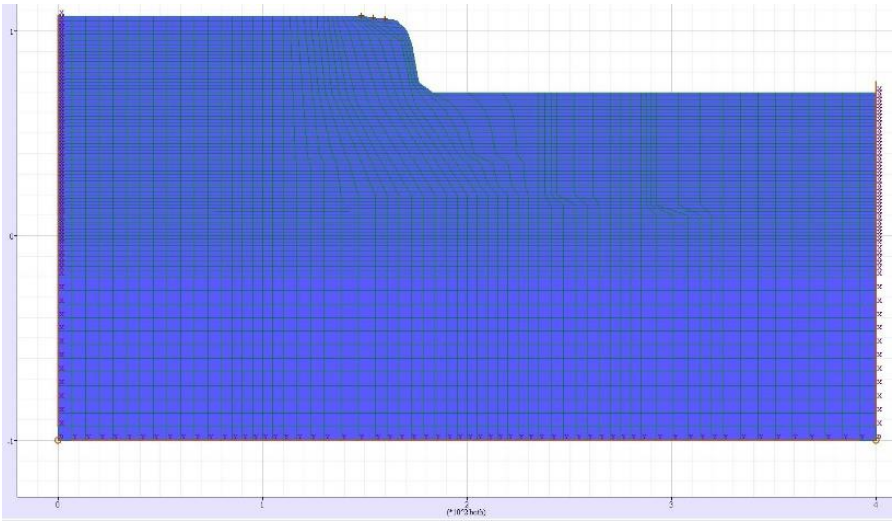

Figure D-13 Excavation to 60 mOD following the quarry profile.

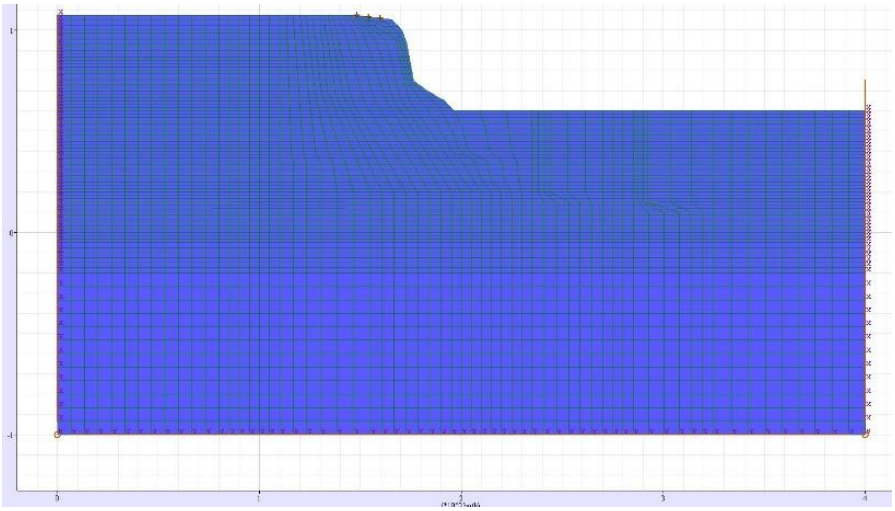

Figure D-14 Excavation to 55 mOD following the quarry profile.

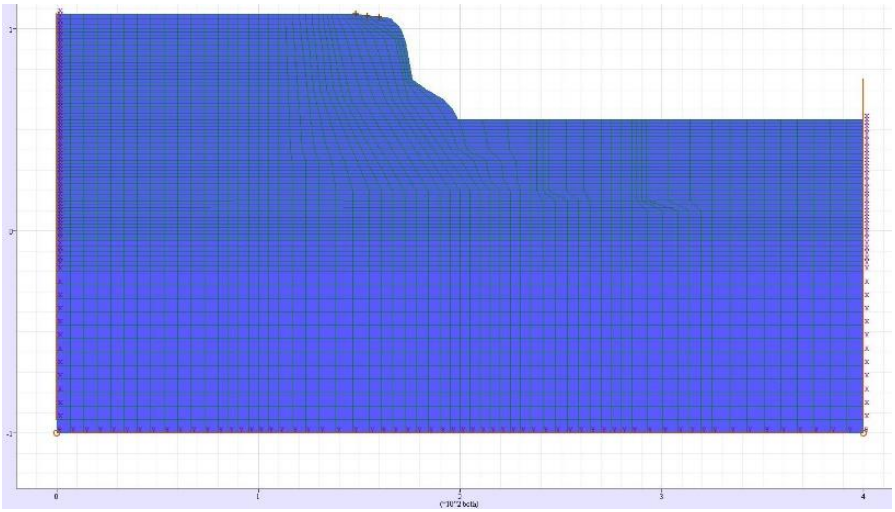

Figure D-15 Excavation to 50 mOD following the quarry profile.

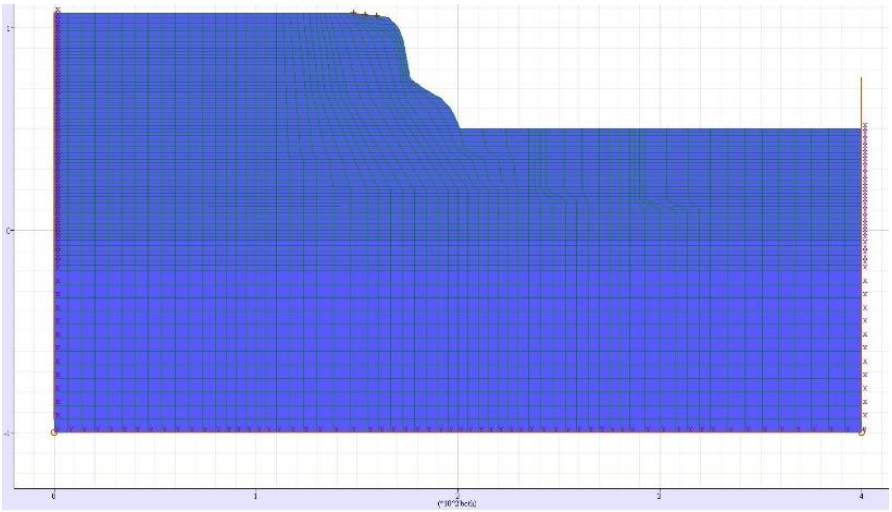

Figure D-16 Excavation to 45 mOD following the quarry profile.

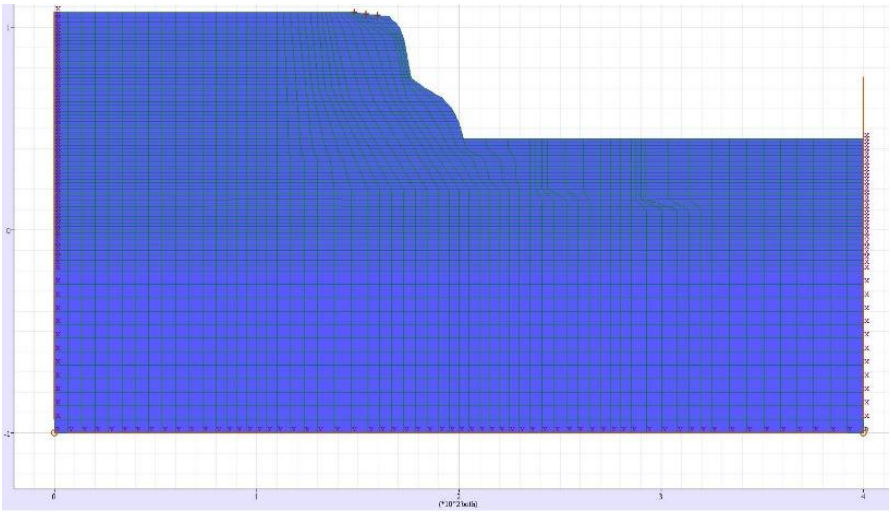

Figure D-17 Excavation to 40 mOD following the quarry profile.

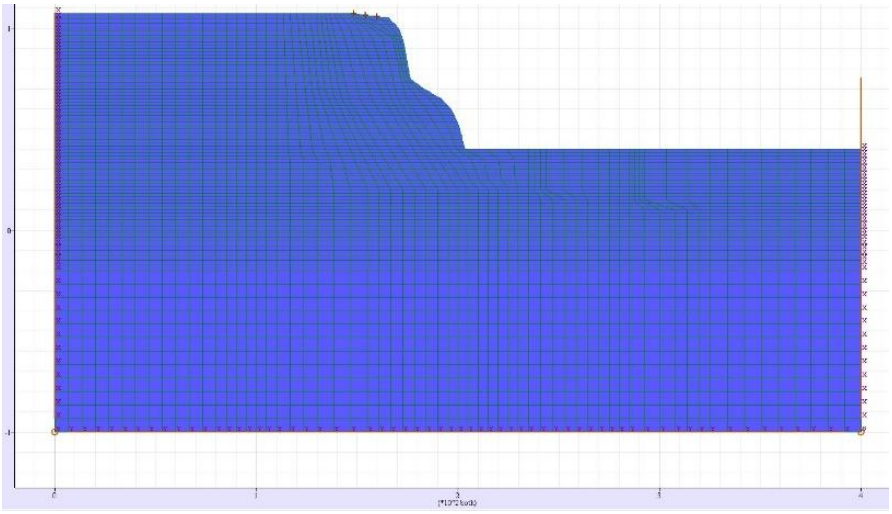

Figure D-18 Excavation to 35 mOD following the quarry profile.

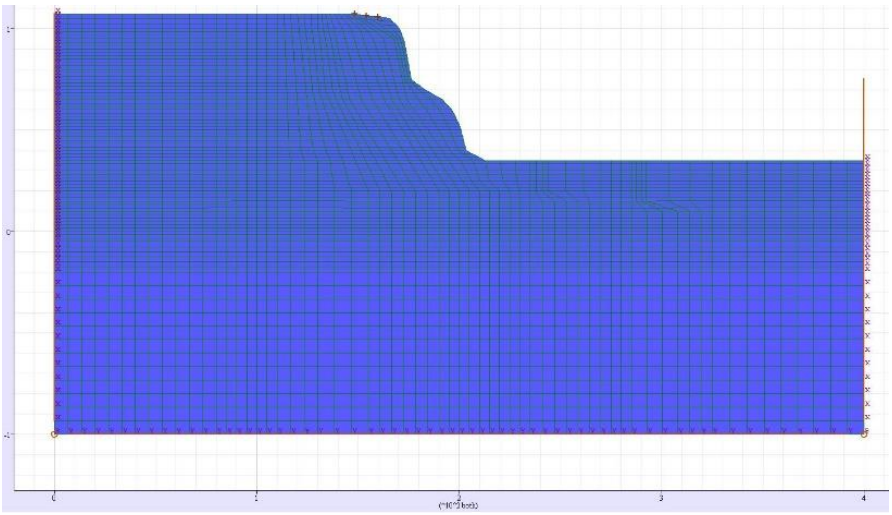

Figure D-19 Excavation to 30 mOD following the quarry profile.

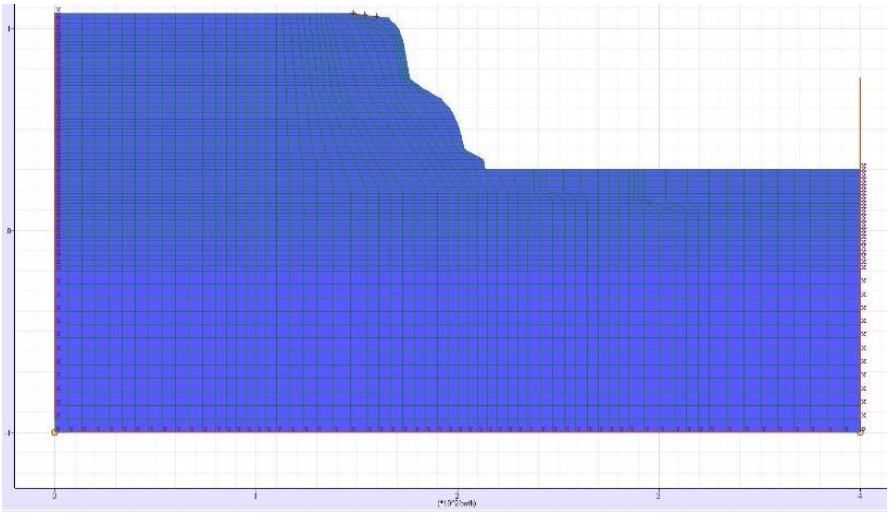

Figure D-20 Excavation to 25 mOD following the quarry profile.

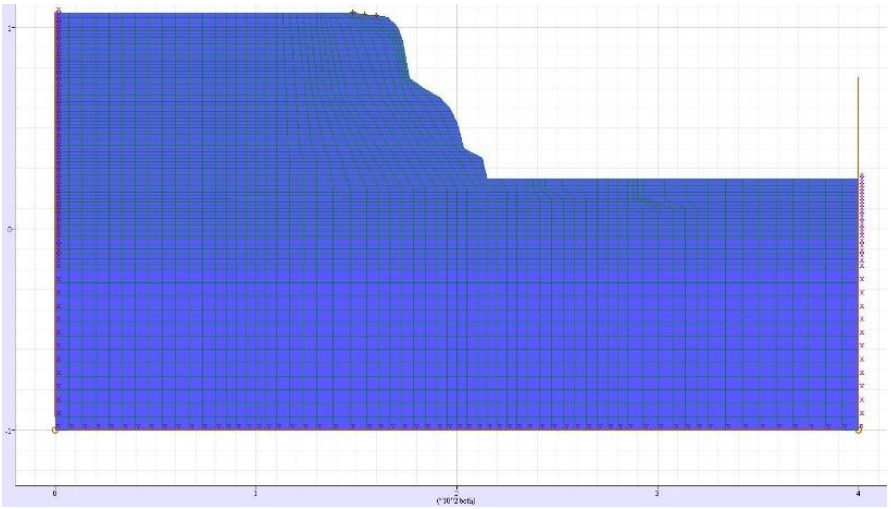

Figure D-21 Excavation to 20 mOD following the quarry profile.

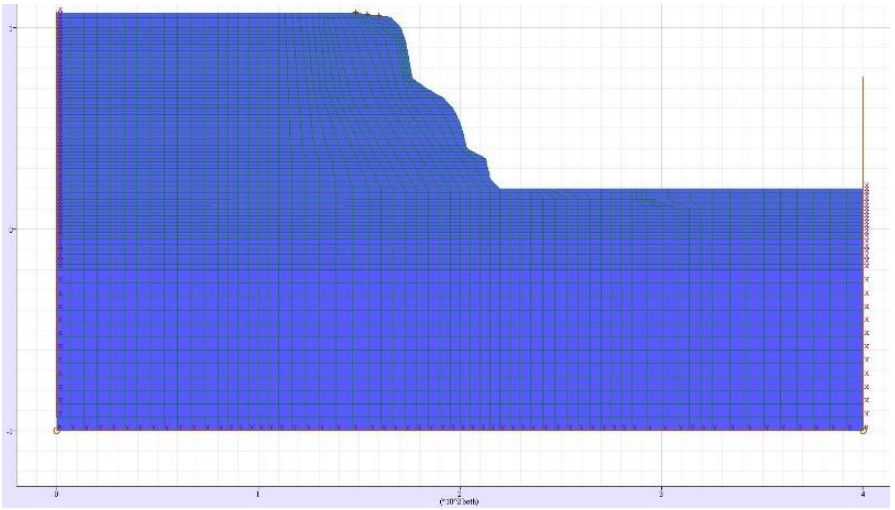

Figure D-22 Excavation to 15 mOD following the quarry profile.

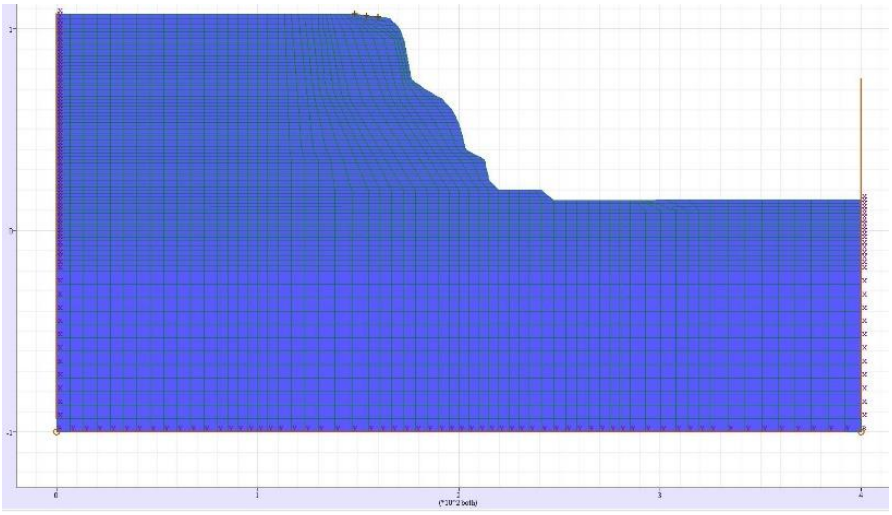

Figure D-23 Excavation to 10 mOD following the quarry profile.

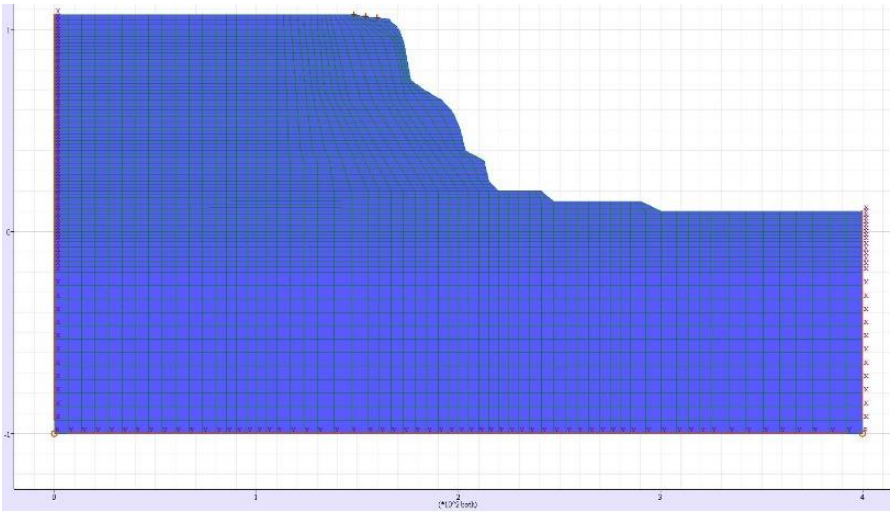

Figure D-24 Vertical stress calculated prior to factor of safety calculation.

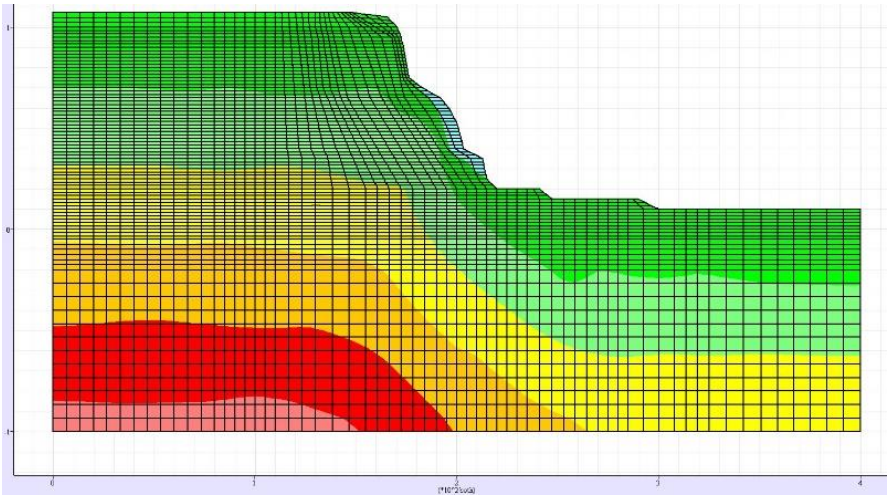

D.3 Parameter selection

D.3.1 Tensile and compressive strength

Davies (2020) suggests a normal distribution for Schmidt hammer results for various lithologies outcropping around Dorothea Quarry. Figure D-25 shows the probability distribution of over 14,000 Schmidt hammer results based on the geological subdivisions adopted by Davies (2020). Although the data contains no information on the orientation of the test, orientation relative to bedding or cleavage, a density correction or the relative weathering / freshness of the surface tested it is clear that four of the units tested have a higher average Schmidt rebound value and lower standard deviation, it is suggested that this inadvertently identifies materials without pronounced strength anisotropy, i.e. Davies' hornfels, a grit, an intrusion and the green slate. Figure D-25 indicates a range of strength values as well as a variety of geological subdivisions present.

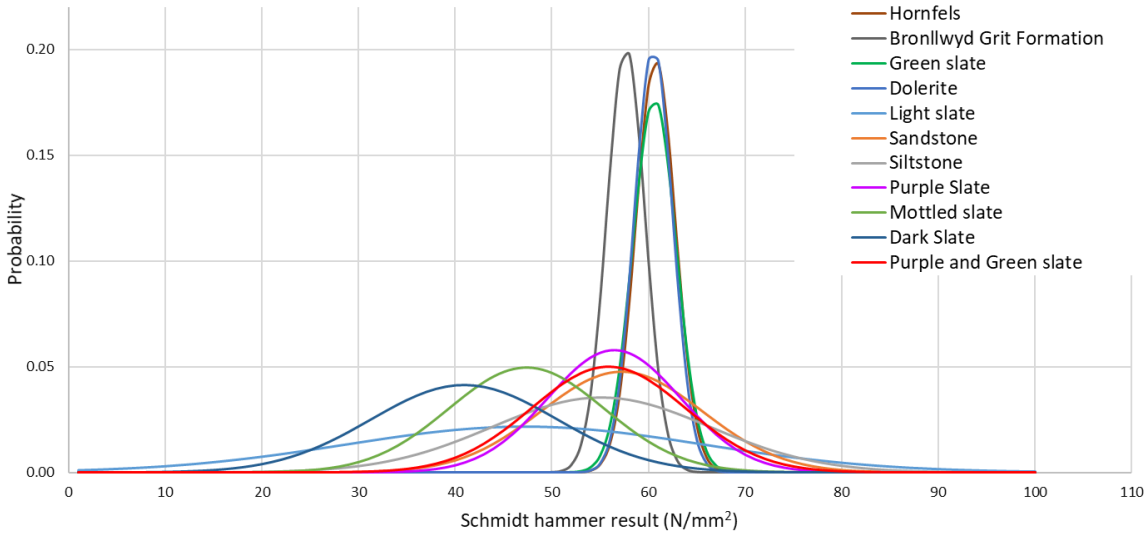

Figure D-25 Probability distribution function for Schmidt hammer Davies (2020).

The analyses undertaken were repeated for values of σ_{ci} of 1, 5, 12.5, 25, 50 and 100 MPa, consistent with the threshold values of strength descriptions in BS 5930 (BSI, 2015) and

BS EN ISO 14689 (BSI, 2018), given as Appendix A. Where the factor of safety <<1.0, a value cannot be calculated, and the computation automatically terminates. In such cases a higher value of σ_{ci} was adopted for a subsequent analysis to try and calculate a factor of safety ≈1.0. It is recognised that adopting a ubiquitous value of strength is a necessary simplification of the complexity and variability within a lithological variable rock mass.

With respect to tensile strength, the approach adopted was to utilise a value of $\sigma_t = \sigma_{ci}/6.4$ based on the mean ratio observed from elsewhere in the slate belt, as shown in Table 3.4 and Figure 3-13.

D.3.2 Geological Strength Index

The GSI of the rock mass concerned has not been determined, however Davies (2020) reported values of RQD (Figure D-26) from scanline measurements. Based on Equation 5.1 the value of GSI is likely to be close to 100, notwithstanding this it was considered prudent to undertake analyses for GSI = 100 (i.e. intact behaviour) and sensitivity checks for reduced GSI values of 80 and 60. This allows the effect of reduced rock quality to be assessed, such as in volumes of rock associated with increased fracturing, fault zones and limitations on accessibility.

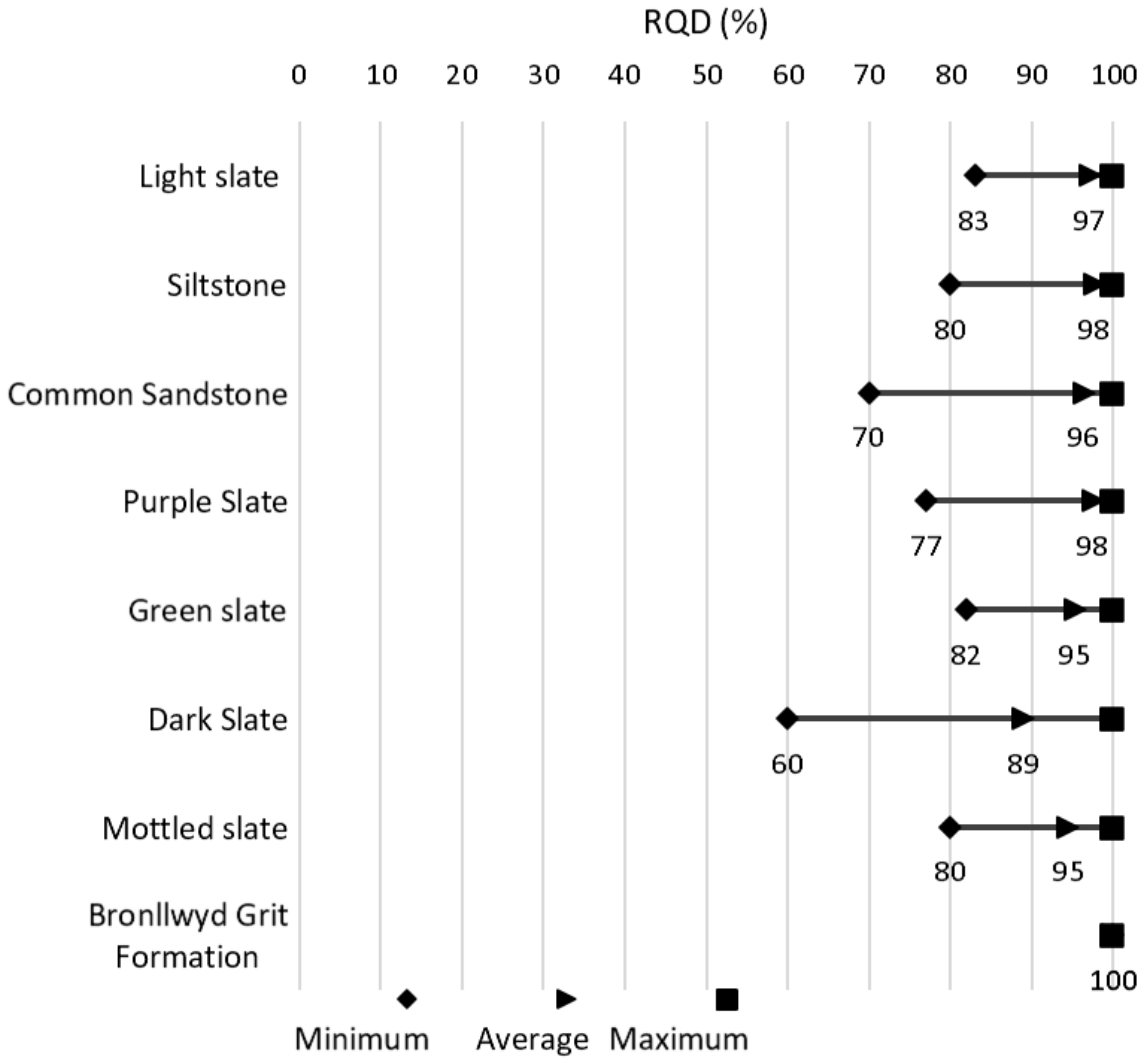

Figure D-26 Range of RQD values, plotted from values reported by Davies (2020).

D.3.3 Disturbance factor and in-situ stresses

A ubiquitous value of D = 1.0 was adopted for the analysis of a slope to reflect stress relief from excavation. This value may not be applicable to a tunnel but is entirely appropriate for the analysis of a slope (Hoek, et al., 2002). What is not known is the extent away from the quarry face for which a value of D = 1.0 is applicable. For the analyses it was considered a reasonable assumption that a zone of rock closest to the excavation and associated with potential failure will be associated with the maximum

disturbance factor from stress relief and or blasting damage, therefore a value of D = 1.0 was used throughout the analyses.

Not directly considered in the analyses is the likely situation of initial horizontal in-situ stressing being higher than vertical stresses. In the case of the slope considered this is not detrimental to the analyses undertaken as any initial in-situ stress regime will have been corrupted by the significant excavation of a steep rock slope of over 100 m high.

D.3.4 Petrographic constant m_i

Two values of m_i were considered, 6 and 10, based on upper and lower bound published values for slates and metapelites (Appendix B, Table B.1).

D.3.5 Parameters a, s and m_b

For each numerical simulation the value of a, s and m_b was calculated based on Equation 4.2 to Equation 4.4, and values adopted for analysis summarised in Table D.2.

D.3.6 Bulk unit weight

A value of 2790 kg/m^3 was used based on measurements summarised in Table 3.3.

D.3.7 Elastic moduli

A shear modulus (G) of 20.83 GPa and bulk modulus (K) of 27.78 GPa were used throughout the analyses based on E = 50 GPa and v = 0.2 (Equation D.1). An E = 50 GPa was adopted based on measurements of back analyse from Dinorwic (Douglas et al., 1983).

$$E = 2G\,(1+v) = 3K\,(1-2v)$$

Equation D.1 Relationship of bulk, shear and Young's modulus.

Hoek and Diederichs (2006) propose methods for estimating rock mass modulus, E_{rm}, in isotropic rock where there are measurements of intact rock deformation modulus (E_i), (Equation D.2). Therefore, the adoption of an E, or E_{rm} = 50 GPa has been compared to values of E_{rm} derived from Equation D.2 (Figure D-27) for differing values of D and GSI. For Figure D-27 an intact stiffness value of E_i = 75.6 GPa was used, the mean of results available from Glyn Rhonwy (Table 3.3). This suggests that a mass stiffness of 50 GPa may well reflect either a higher intact stiffness or, more likely, a stiffer response of the rock mass from less disturbance of the rock mass from excavation of Dinorwic's Machine Hall compared to Dorothea Quarry.

A value of An E = 50 GPa remains appropriate as the value is adopted through the analyses irrespective of proximity to the rockface and the inherent disturbance. Notwithstanding the value of E adopted, the purposes of the analyses is to predict failure rather than accurately predict deformation.

$$E_{rm} = E_i \left(0.02 + \frac{1 - {}^{D}/_{2}}{1 + \exp\left(\frac{(60 + 15D - GSI)}{11}\right)} \right)$$

Equation D.2 Rock mass deformation modulus (Hoek and Diederichs, 2006).

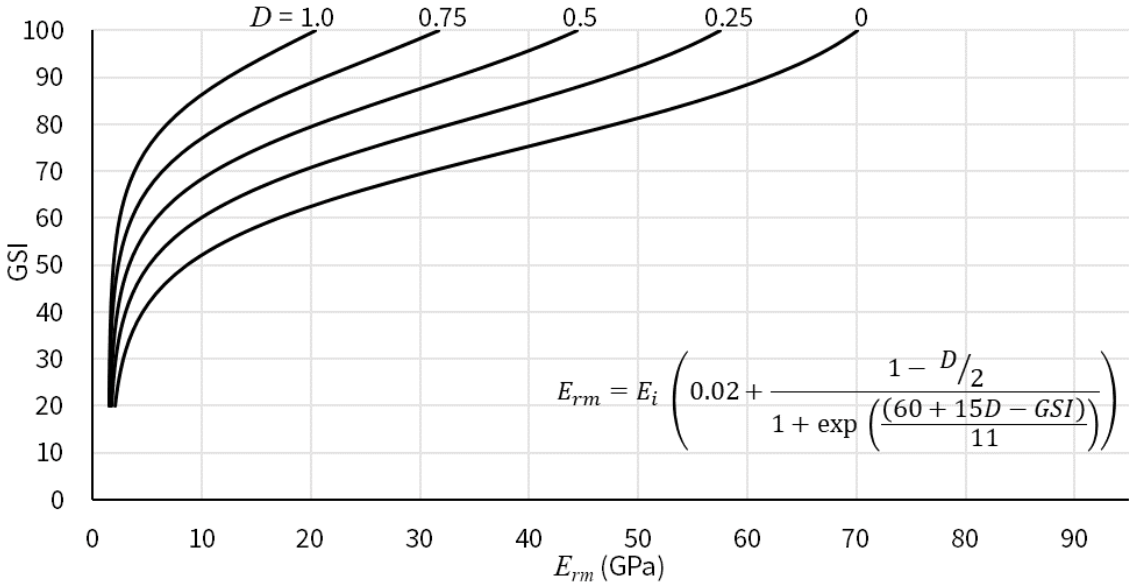

Figure D-27 Graph of rock mass deformation modulus based on Equation D.2.

D.3.8 Summary of parameters

A summary of the parameters used in the analyses is provided below.

Parameter	Values adopted for analysis
σ_{ci}	Repeated analyses adopting 1, 5, 12.5, 25, 50 or 100 MPa with further analyses where these values did not determine a factor of safety ≈ 1.0
σ_t	$\sigma_t = \sigma_{ci}/6.4$
GSI	Repeated analyses with values of 100, 80 and 60
D	1.0, to reflect stress relief and disturbance of the rock mass from excavation
m_i	A value of 6 or 10.
m_b	Equation 4.2
a	Equation 4.4
s	Equation 4.3
γ	2790 kg/m^3 Table 3.3
G and K	20.83 GPa and 27.78 GPa respectively

Table D.1 Summary of Hoek-Brown parameters adopted for analysis.

D.3.9 Groundwater

Groundwater was pumped from the Dorothea Quarry complex to allow slate extraction. This resulted in depression of groundwater to at least 5 mOD beneath the deepest part of the quarry. Cessation of pumping resulted in filling of the quarries to the current level

over a 5-year period. Quarry water level has remained static at 97.3 mOD during the period for which data is available, approximately five years.

For analysis purposes the case of no water being present has been considered, comparable to the final years of quarrying when groundwater levels were artificially depressed below the floor of the quarry. Groundwater is therefore not specifically considered in the analyses as the slopes were dry at the time of maximum drawdown. It is worth noting that any future drawdown for construction and the cyclic change in water level would need to consider the resulting rapid and cyclic change in stress in the rock mass. The absence of water from the analyses is considered appropriate to help understand the behaviour of the rock mass alone.

D.4 FLAC results

File name	σ_{ci} MPa	σ_t MPa	D	GSI	m_i	m_b	s	a	Factor of safety	Date
001.txt	20	3.125	0	100	6	6	1	0.5	10.2706	14/07/20
002.txt	10	1.5625	0	100	6	6	1	0.5	6.3577	14/07/20
003.txt	5	0.78125	0	100	6	6	1	0.5	4.1839	14/07/20
004.txt	2.5	0.390625	0	100	6	6	1	0.5	2.5864	14/07/20
005.txt	1.25	0.195313	0	100	6	6	1	0.5	1.6895	14/07/20
006.txt	1	0.15625	0	100	6	6	1	0.5	1.4902	14/07/20
007.txt	0.65	0.101563	0	100	6	6	1	0.5	1.17	14/07/20
008.txt	0.4	0.0625	0	100	6	6	1	0.5	0.9082	14/07/20
009.txt	0.25	0.039063	0	100	6	6	1	0.5	0.6855	14/07/20
010.txt	20	3.125	0	100	7	7	1	0.5	10.1205	15/07/20
011.txt	10	1.5625	0	100	7	7	1	0.5	6.3782	15/07/20
012.txt	5	0.78125	0	100	7	7	1	0.5	4.136	15/07/20
013.txt	2.5	0.390625	0	100	7	7	1	0.5	2.5864	15/07/20
014.txt	1.25	0.195313	0	100	7	7	1	0.5	1.7168	15/07/20
015.txt	1	0.15625	0	100	7	7	1	0.5	1.5098	15/07/20
016.txt	0.65	0.101563	0	100	7	7	1	0.5	1.1973	15/07/20
017.txt	0.4	0.0625	0	100	7	7	1	0.5	0.9316	15/07/20
018.txt	0.25	0.039063	0	100	7	7	1	0.5	-	15/07/20
100.txt	2.25	0.351563	0	100	20	20	1	0.5	9.7433	14/07/20
110.txt	1	0	0	100	6	6	1	0.5	1.4551	14/07/20
111.txt	0.65	0	0	100	6	6	1	0.5	-	14/07/20
112.txt	5	0	0	100	6	6	1	0.5	-	14/07/20
113.txt	20	3.125	0	80	6	2.93725	0.108368	0.500593	4.8982	20/07/20
114.txt	20	3.125	0.5	80	6	2.314928	0.069483	0.500593	4.1873	20/07/20
115.txt	20	3.125	1	80	6	1.437906	0.035674	0.500593	3.3481	20/07/20
200.txt	1	0.15625	0	100	6	6.000	1.000	0.500	1.49	21/07/20
201.txt	5	0.78125	0	100	6	6.000	1.000	0.500	4.18	21/07/20
202.txt	12.5	1.953125	0	100	6	6.000	1.000	0.500	7.36	22/07/20
203.txt	25	3.90625	0	100	6	6.000	1.000	0.500	12.16	22/07/20
204.txt	50	7.8125	0	100	6	6.000	1.000	0.500	21.52	22/07/20
205.txt	100	15.625	0	100	6	6.000	1.000	0.500	-	22/07/20
400.txt	1	0.15625	0	80	6	2.937	0.108	0.501	0.912	24/08/20
401.txt	5	0.78125	0	80	6	2.937	0.108	0.501	2.03857	24/08/20
402.txt	12.5	1.953125	0	80	6	2.937	0.108	0.501	3.53857	24/08/20
403.txt	25	3.90625	0	80	6	2.937	0.108	0.501	5.74243	24/08/20
404.txt	50	7.8125	0	80	6	2.937	0.108	0.501	8.72156	24/08/20
405.txt	100	15.625	0	80	6	2.937	0.108	0.501	14.1525	24/08/20

File name	σ_{ci} MPa	σ_t MPa	D	GSI	m_i	m_b	s	a	Factor of safety	Date
406.txt	1	0.15625	0	60	6	1.438	0.012	0.503	-	24/08/20
407.txt	5	0.78125	0	60	6	1.438	0.012	0.503	1.23633	24/08/20
408.txt	12.5	1.953125	0	60	6	1.438	0.012	0.503	1.89258	24/08/20
409.txt	25	3.90625	0	60	6	1.438	0.012	0.503	2.73877	24/08/20
410.txt	50	7.8125	0	60	6	1.438	0.012	0.503	4.14282	24/08/20
411.txt	100	15.625	0	60	6	1.438	0.012	0.503	6.68921	24/08/20
412.txt	1	0.15625	1	80	6	1.438	0.036	0.501	-	24/08/20
603.txt	2	0.3125	1	80	6	1.438	0.036	0.501	1.0020	19/09/20
413.txt	5	0.78125	1	80	6	1.438	0.036	0.501	1.4824	24/08/20
414.txt	12.5	1.953125	1	80	6	1.4379	0.0357	0.5006	2.50146	24/08/20
415.txt	25	3.90625	1	80	6	1.438	0.036	0.501	3.93701	24/08/20
416.txt	50	7.8125	1	80	6	1.438	0.036	0.501	6.1936	24/08/20
417.txt	100	15.625	1	80	6	1.438	0.036	0.501	9.63708	24/08/20
418.txt	1	0.15625	1	60	6	0.345	0.001	0.503	-	24/08/20
419.txt	5	0.78125	1	60	6	0.345	0.0013	0.503	-	24/08/20
601.txt	10	1.5625	1	60	6	0.345	0.0013	0.503	0.951172	19/09/20
420.txt	12.5	1.953125	1	60	6	0.345	0.0013	0.503	1.06836	24/08/20
421.txt	25	3.90625	1	60	6	0.345	0.0013	0.503	1.45508	24/08/20
422.txt	50	7.8125	1	60	6	0.345	0.0013	0.503	2.12939	24/08/20
423.txt	100	15.625	1	60	6	0.345	0.0013	0.503	3.20459	24/08/20
500.txt	1	0.15625	0	100	10	10.000	1.000	0.500	1.58008	24/08/20
501.txt	5	0.78125	0	100	10	10.000	1.000	0.500	4.00952	24/08/20
502.txt	12.5	1.953125	0	100	10	10.000	1.000	0.500	7.40356	24/08/20
503.txt	25	3.90625	0	100	10	10.000	1.000	0.500	11.4755	24/08/20
504.txt	50	7.8125	0	100	10	10.000	1.000	0.500	19.2454	24/08/20
505.txt	100	15.625	0	100	10	10.000	1.000	0.500	-	24/8/20
506.txt	1	0.15625	0	80	10	4.895	0.108	0.501	1.0377	24/08/20
507.txt	5	0.78125	0	80	10	4.895	0.108	0.501	2.11475	24/08/20
508.txt	12.5	1.953125	0	80	10	4.895	0.108	0.501	3.47998	24/08/20
509.txt	25	3.90625	0	80	10	4.895	0.108	0.501	5.40063	24/08/20
510.txt	50	7.8125	0	80	10	4.895	0.108	0.501	8.74353	24/08/20
511.txt	100	15.625	0	80	10	4.895	0.108	0.501	13.3065	24/08/20
512.txt	1	0.15625	0	60	10	2.397	0.012	0.503	-	24/8/20
513.txt	5	0.78125	0	60	10	2.397	0.012	0.503	1.38477	24/08/20
514.txt	12.5	1.953125	0	60	10	2.397	0.012	0.503	1.99805	24/08/20
515.txt	25	3.90625	0	60	10	2.397	0.012	0.503	2.78857	24/08/20
516.txt	50	7.8125	0	60	10	2.397	0.012	0.503	4.06421	24/08/20
517.txt	100	15.625	0	60	10	2.397	0.012	0.503	6.22778	24/08/20
518.txt	1	0.15625	1	80	10	2.397	0.036	0.501	-	24/8/20

File name	σ_{ci} MPa	σ_t MPa	D	GSI	m_i	m_b	s	a	Factor of safety	Date
604.txt	2	0.3125	1	80	10	2.397	0.036	0.501	1.05664	19/09/20
519.txt	5	0.78125	1	80	10	2.397	0.036	0.501	1.5918	24/08/20
520.txt	12.5	1.953125	1	80	10	2.397	0.036	0.501	2.53662	24/08/20
521.txt	25	3.90625	1	80	10	2.3965	0.0357	0.5006	3.80518	19/09/20
522.txt	50	7.8125	1	80	10	2.397	0.036	0.501	6.08423	19/09/20
523.txt	100	15.625	1	80	10	2.397	0.036	0.501	9.44299	19/09/20
524.txt	1	0.15625	1	60	10	0.574	0.0013	0.503	-	19/9/20
525.txt	5	0.78125	1	60	10	0.574	0.0013	0.503	-	19/9/20
602.txt	10	1.5625	1	60	10	0.574	0.0013	0.503	1.07227	19/09/20
526.txt	12.5	1.953125	1	60	10	0.574	0.0013	0.503	1.16992	24/08/20
527.txt	25	3.90625	1	60	10	0.574	0.0013	0.503	1.5957	24/08/20
528.txt	50	7.8125	1	60	10	0.574	0.0013	0.503	2.19678	24/08/20
529.txt	100	15.625	1	60	10	0.574	0.0013	0.503	3.1958	24/08/20
605.txt	1	0.15625	1	90	6	2.9372	0.1889	0.5002	0.978516	19/09/20
606.txt	5	0.78125	1	90	6	2.9372	0.1889	0.5002	2.36963	19/09/20
607.txt	12.5	1.953125	1	90	6	2.9372	0.1889	0.5002	4.40942	19/09/20
608.txt	25	3.90625	1	90	6	2.9372	0.1889	0.5002	6.71655	19/09/20
609.txt	50	7.8125	1	90	6	2.9372	0.1889	0.5002	10.787	19/09/20
610.txt	100	15.625	1	90	6	2.9372	0.1889	0.5002	18.6059	19/09/20
611.txt	10	0	1	60	6	0.345	0.0013	0.503	0.951172	19/09/20

Table D.2 Summary of FLAC results.

The Table above excludes values of γ = 27.9 kN/m^3, as well as G = 20.83 GPa and K = 27.78 GPa based on E = 50 GPa and ν = 0.2, which were the same for all analyses.

Where a dash appears in the Table above, no factor of safety could be calculated (i.e. factor of safety was too low to allow computation).

Where rows are greyed out these were initial analyses to test and manipulate the software.

Appendix E. Slope stability analyses using Slide

E.1 Purpose

This purpose of this Appendix is to document additional analyses using Generalised Hoek-Brown behaviour using Rocscience's Slide v6.039 software to corroborate the FLAC analyses documented in Appendix D.

E.2 Corroboration of FLAC analyses

E.2.1 Analyses undertaken

Slide analyses allow calculation of a factor of safety for Bishop's simplified method for a 2D slice. Simulations adopted the same cross section though the side of Dorothea Quarry previously adopted for the FLAC analyses (Figure D-1). Unlike FLAC, Slide does not allow for the sequencing of the idealised excavation of the quarry as a method to develop a stress history as a way of "relaxing" higher horizontal stresses. Stresses calculated in the Slide software are therefore only the product of self-weight, depth of overburden and any pore water pressure, thereby greatly reducing computation time. As with FLAC there is provision for materials to be ascribed Hoek-Brown parameters.

E.2.2 Parameters and results

To allow comparison with the FLAC analyses combinations of parameters used in the analyses were used where FLAC analyses calculated a factor of safety of <1.5. As Slide (or Hoek-Brown) make no provision for a tensile strength no allowance for tensile strength was made. Results are shown in Table D.2 alongside the comparable FLAC result from Table E.1. For ease of reference the file name denotes a unique set of parameters given in Table D.2, i.e. "601" and the file extension ".txt" or ".slim" denotes a text file for use in FLAC or a Slide file respectively.

Factor of safety		File reference	
FLAC	Slide	FLAC	Slide
0.912	0.949	400.txt	400.slim
1.236	1.238	407.txt	407.slim
1.002	0.966	603.txt	603.slim
1.482	1.461	413.txt	413.slim
0.951	1.002	601.txt	601.slim
1.068	1.101	420.txt	420.slim
1.455	1.484	421.txt	421.slim
1.038	1.087	506.txt	506.slim
1.385	1.439	513.txt	513.slim
1.057	1.099	604.txt	604.slim
1.072	1.146	602.txt	602.slim
1.170	1.245	526.txt	526.slim
0.979	0.996	605.txt	605.slim

Table E.1 Comparison of FLAC and Slide analyses.

E.2.3 Observations

The Slide analyses are sufficiently close to the results of the FLAC simulations to suggest mutual corroboration of the predicted behaviour of the rock mass and that predictions of a factor of safety close to unity are not the product of errors in developing the FLAC model or input errors. The notable difference is that the Slide analyses only utilised an

automated search function for a circular failure surface, which aligns well with the lowest factor of safety from FLAC, which is not restricted to circular failure surfaces.